Investigating Focused Electron Beam Induced Processing on Organic and Metal-Organic Substrates

Untersuchungen zur lokalen Modifikation von organischen und metallorganischen Substraten mittels eines hochfokussierten Elektronenstrahls

Der Naturwissenschaftlichen Fakultät der

Friedrich-Alexander-Universität Erlangen-Nürnberg

zur Erlangung des Doktorgrades Dr. rer. nat.

vorgelegt von

Martin Georg Drost

aus Erlangen

Als Dissertation genehmigt

von der Naturwissenschaftlichen Fakultät

der Friedrich-Alexander-Universität Erlangen-Nürnberg

Tag der mündlichen Prüfung: 11.09.2017

Vorsitzender des Promotionsorgans: Prof. Dr. Georg Kreimer

Gutachter: PD Dr. Hubertus Marbach

                  Prof. Dr. Jörg Libuda

Table of contents

List of abbreviations

2HTPP	2H-Tetraphenylporphyrin
AC	Alternating Current
AE(S)	Auger Electron (Spectroscopy)
(NC-)AFM	(Non-Contact) Atomic Force Microscopy
AG	Autocatalytic Growth
ALD	Atomic Layer Deposition
BSE	Backscattered Electron
DAC	Digital-Analog Converter
DC	Direct Current
DD	Dipolar Dissociation
DEA	Dissociative Electron Attachment
DFT	Density Functional Theory
DI	Dissociative Ionization
EBID	Electron Beam Induced Deposition
EBIE	Electron Beam Induced Etching
EBISA	Electron Beam Induced Surface Activation
EBL	Electron Beam Lithography
EDX	Energy Dispersive X-Ray Spectroscopy
ESD	Electron Stimulated Desorption
FEBIP	Focused Electron Beam Induced Processing
FSE	Forward Scattered Electron
FWHM	Full Width at Half Maximum
LDOS	Local Density of States
LEED	Low Energy Electron Diffraction
MC	Monte Carlo (Simulation)
ND	Neutral Dissociation
NEXAFS	Near Edge X-Ray Absorption Fine Structure (Spectroscopy)
PBN	Pyrolitic Boron Nitride
PE	Primary Electron
QMS	Quadrupole Mass Spectrometry
RT	Room Temperature

SAM	Scanning Auger Microscopy
SE(I,II,III)	Secondary Electron (Type I, II, III)
SEM	Scanning Electron Microscopy
STM	Scanning Tunneling Microscopy
(S)TEM	(Scanning) Transmission Electron Microscopy
STXM	Scanning Transmission X-Ray Microscopy
(SUR)MOF	(Surface-Anchored) Metal-Organic Framework
TMP	Turbomolecular Pump
(U)HV	(Ultra-) High Vacuum
VT	Variable Temperature
WDX	Wavelength Dispersive X-Ray Spectroscopy

1 Introduction

Modern human societies of the 21st century rely in many ways on the application of nanotechnology, which is a general term for the use of functional nanoscale objects. The most important fields of application are probably computers, which consist of modular microelectronic units, most importantly integrated circuits that can house more than 25 million transistors per mm² as of 2016 [1]. These devices are fabricated by photolithography, where light illuminates a photoresist layer through a patterned photomask, thereby modifying the resist layer for further processing with the irradiated areas conforming to the mask pattern. The photomasks are produced by maskless lithography, using focused photon (e.g. Direct Laser Writing) or electron beams (Electron Beam Lithography, EBL [2]). EBL is becoming increasingly important in this regard, with ~ 37.5 % of the photomask production in 2011 [3], as it offers superior resolution (< 10 nm) compared to photon-based techniques. Besides photomask production, it is also widely used for prototype fabrication due to its flexibility, e.g. in nanoelectronic and nanophotonic devices [4]. In EBL, a focused electron beam is employed to fabricate a surface pattern in a resist layer, inducing chemical changes. Subsequent developing, like in photolithography, can selectively remove the exposed part (positive resist) or the unexposed part (negative resist). Metal deposition and removal of the residual resist leads to metallic structures that conform to the irradiated pattern. Thus, EBL requires multiple processing steps and is restricted to two-dimensional structures and in the choice of materials.

In the past two decades, a number of closely related techniques that can overcome these limitations have been increasingly investigated, subsumed under the term Focused Electron Beam Induced Processing (FEBIP) [5, 6]. The most common technique in FEBIP is Electron Beam Induced Deposition (EBID). In EBID, material is deposited on a surface by using a focused electron beam, typically from a Scanning Electron Microscope (SEM), to directly dissociate precursor molecules which are supplied from the gas phase. The volatile dissociation products can desorb into the gas phase, whereas the non-volatile products form the deposit at the impact point of the electron beam. Therefore, in EBID only one processing step is required, making it inherently faster than EBL. It can be employed on practically any non-insulating surface and has 3D capabilities. Another major advantage is the variety of possible materials that can be deposited due to the large amount of available precursor compounds.

In 2010, Walz et al. introduced a novel technique termed Electron Beam Induced Surface Activation (EBISA) [7]. EBISA is a two-step process in which the electron beam irradiates a suitable surface, such as a native silicon oxide layer, in the absence of a precursor. Thereby the surface at the irradiated positions is modified such that they become catalytically active towards dissociation of subsequently supplied precursor molecules, leading to deposit formation at pre-irradiated sites. So far it has been demonstrated that EBISA is possible with the precursor $Fe(CO)_5$ on silicon oxide (native and thermal) [7, 8], rutile $TiO_2(110)$ [9] and thin layers of 2H-tetraphenylporphyrin (2HTPP) on Ag(111) [10].

The FEBIP techniques face two main challenges which are usually in the focus of current research. One is to obtain full control over the chemical composition of the deposit, which is complicated as unwanted precursor and residual gas dissociation products (mostly C and O) tend to be incorporated. The second main challenge, which FEBIP shares with EBL, are proximity effects, referring to the unintended deposit broadening due to the contribution of backscattered and secondary electrons (BSE, SE) to the deposit formation outside of the electron beam impact point.

In this context, the objective of this thesis is to contribute to the growing field of FEBIP research, by addressing the aforementioned challenges and by expanding the EBID and EBISA techniques to novel substrates and precursors. To do so, the experimental approach was that all FEBIP experiments were performed in an ultra-high vacuum (UHV) environment to minimize the contribution of surface-adsorbed residual gas, unlike experiments by most other research groups which are usually performed in high vacuum (HV). UHV conditions also enable the preparation of atomically well-defined, clean surfaces to study their influence on the FEBIP process.

The two precursors used in this work were $Fe(CO)_5$ and $Co(CO)_3NO$. Previous studies have shown that under UHV conditions, deposits from both precursors can grow autocatalytically already at room temperature (RT), meaning they grow in size as long as precursor molecules are supplied. AG offers interesting advantages which are discussed in chapter 2.6.3. Both precursors were chosen due to the ability to grow autocatalytically, their ease of handling and also due to the prospect to fabricate (possibly bimetallic) magnetic nanostructures [11-14].

After introducing the theoretical and experimental aspects of the techniques used, the first chapter in the main part expands the EBISA technique to the precursor $Co(CO)_3NO$, by demonstrating that it is possible to correspondingly activate thin layers of 2HTPP on $TiO_2(110)$ and Si(111), while the 2HTPP layers also effectively prevent the unselective

catalytic decomposition of Co(CO)$_3$NO on both pristine surfaces. The second chapter presents a combined experimental and theoretical study to obtain fundamental, quantitative information concerning the minimum backscattered electron doses required to activate different surfaces in EBISA. The third chapter expands EBID and EBISA to a new, unique class of substrates: Surface-Anchored Metal-Organic Frameworks (SURMOFs), which offer a variety of interesting properties for the FEBIP process, and vice versa. The last chapter presents a new concept, along with first experimental results: the use of FEBIP to pattern suitable surfaces for the localized adsorption of functional molecules, here 2HTPP.

All FEBIP experiments and characterization were performed with a UHV-compatible SEM with a beam diameter < 3 nm. The chamber also houses a hemispherical electron energy analyzer, enabling local Auger Electron Spectroscopy (AES) by using the electron beam as an excitation source, providing spectromicroscopic information about the FEBIP deposits.

2 Fundamentals and techniques

2.1 Scanning Electron Microscopy (SEM)

In Scanning Electron Microscopy (SEM) [15, 16], a highly focused electron beam is raster-scanned over a sample area of interest and the intensity of the subsequently emitted backscattered and/or secondary electrons is detected as a function of the beam position. The primary electrons (PEs) forming the electron beam are accelerated to kinetic energies (E_{PE}) typically in the range of 1-30 keV. As the lateral resolution of an SEM is mainly determined by the electron beam spot size, the primary electrons are focused by a series of electromagnetic lenses to usually obtain the smallest possible beam diameter and thus resolution, typically 1-10 nm in state-of-the-art SEMs or even sub-nm [17, 18]. The possibility to investigate bulk samples is a major advantage over (Scanning) Transmission Electron Microscopy ((S)TEM), where the specimen must be sufficiently thin to be able to transmit enough electrons. A detailed description of the SEM instrument used in this work can be found in chapter 3.1.1.

Interaction of the PEs with the sample can result in the emission of backscattered electrons (BSEs), secondary electrons (SEs), Auger electrons (AEs) and electromagnetic radiation. BSEs result from elastic and inelastic scattering of PEs at the surface or in the sample, thus, they can have a kinetic energy E_{Kin} up to E_{PE} when escaping the substrate. These electrons have a certain mean free path of traveling through the substrate until they are absorbed, called the *penetration depth* R whereas the complete volume where scattering and formation of secondary electrons and electromagnetic radiation takes place is called *interaction volume*. The penetration depth increases with increasing PE energy and decreasing mean atomic number of the substrate. Due to the limited mean free path until they are absorbed, the electrons that result from beam-sample interactions can escape the sample only from a limited depth, called the *information* or *electron escape depth*.

As the information depth of BSEs can be in the order of μm, they might contain information concerning bulk properties of the sample. SEs are formed by ionization of substrate atoms by inelastically scattered BSEs and generally have a kinetic energy of < 50 eV, with an intensity maximum around 5 eV. A prevalent convention classifies all electrons with E_{Kin} < 50 eV as SEs irrespective of their origin [15].

4

Due to their relatively low kinetic energy, SEs have an information depth of only ~ 10 nm, making them more surface sensitive compared to BSEs. SEs are further classified into three subgroups: SE_Is are generated directly by PEs, SE_{II}s are generated by BSEs, therefore also at positions away of the point of impact of the electron beam, and SE_{III}s are SEs originating from outside the specimen, formed by BSEs hitting components in the SEM chamber. AEs are a special type of SEs, resulting from an Auger cascade that can follow the ionization of substrate atoms, as described in more detail in chapter 2.2. Their kinetic energy depends on the binding energy of the involved orbitals. Due to their relatively low intensity compared to BSEs and SEs, AEs are not dominant for image formation in SEM. However, in this work, they are used to obtain spectromicroscopic information in combination with a hemispherical electron energy analyzer (chapter 3.1.1). Another result of beam-sample interaction is electromagnetic radiation, such as continuous and characteristic X-ray emission following inelastic scattering of electrons and X-ray fluorescence respectively. Characteristic X-ray emission is the basis for energy dispersive (EDX) and wavelength dispersive (WDX) X-ray spectroscopy, an important method for elemental analysis, but not used in this work.

Depending on the type of interaction electrons detected a scanning electron micrograph has to be interpreted accordingly. Due to their surface sensitivity, SEs mainly provide information concerning topographic features of the sample. Exposed surface sites such as kinks and edges appear brighter, as less SEs are absorbed by the surrounding material compared to a flat surface or ditches. Depending on the type and location of the detector used, emitted SEs can be absorbed by features located in their path to the detector, giving rise to quasi-shadow effects. Other notable factors influencing the SE emission are the surface tilt, which can vary locally at rough surfaces, and the work function of the investigated substrate. In contrast to this, BSEs mainly provide information concerning material properties. The BSE coefficient, i.e. the number of emitted BSEs per incoming PE, increases with increasing average atomic number of the material, thus heavier elements appear brighter. As the number of emitted of SE_{II}s depends on the number of BSEs, this material contrast can also be observed when detecting SEs. Further material properties that influence BSE and consequently SE emission are conductivity, as local charging influences the trajectories of emitted electrons, and to a lesser extent electron diffraction at crystalline samples.

2.2 Auger Electron Spectroscopy (AES)

AES [19] is a surface science technique that utilizes the emission of so-called Auger electrons upon ionization of substrate atoms. The underlying intra-atomic relaxation pathway was first completely described by Pierre Auger in 1926 [20], but it took until the development of sufficiently sensitive detectors in the 1960s to apply the technique practically [21]. The Auger cascade consists of three basic steps. First, the atom gets ionized either by an electron, photon or ion and therefore an electron vacancy forms. An electron of lower binding energy can then fill the vacancy, leaving the ion in an excited state due to the energy gained in this transition. Disexcitation then occurs via a radiationless transition of the excess energy to another electron, which is then emitted as the Auger electron, leaving behind a doubly-ionized ion. The relatively low kinetic energy and thus short inelastic mean free path of Auger electrons makes AES surface sensitive. The Auger cascade is the complementary process to radiative relaxation via X-ray fluorescence, where the excess energy gained by filling the vacancy by a higher lying electron is emitted as a photon. The probability for an Auger cascade to take place increases with decreasing atomic number and increasing principal quantum number of the electron that is first ejected. The higher surface sensitivity and higher sensitivity for significant low-Z elements, such as carbon and oxygen, makes AES preferable compared to EDX or WDX when investigating FEBIP nanostructures.

The spectroscopic notation of Auger electrons is as follows: usually, the respective element is depicted, followed by three capital letters with a numeric subscript (if necessary), which denote the principal and total angular momentum quantum numbers of the involved orbitals, according to the X-ray notation. As an example, in a C KL_1L_3 transition, ionization takes place in the carbon K-shell, the vacancy is filled by an electron from the L_1-shell, and the subsequently emitted Auger electron originates from the L_3-shell. In some cases the letter V is used to denote an electron from a valence orbital.

In a simplified picture, the measured kinetic energy E_{XYZ} of an Auger electron, referenced to the Fermi level, is

$$E_{XYZ} = E_X - E_Y - E_Z - \Phi_{SP}$$

where E_x is the binding energy of the electron that is first ejected, E_Y the binding energy of the electron that fills the hole, E_Z the binding energy of the emitted Auger electron, and Φ_{SP}

the work function of the spectrometer. Note that this simplified equation does not consider additional energy contributions, amongst others final-state effects due to the presence of two electron vacancies. As the kinetic energy of the emitted electron mainly depends on the binding energies of the involved electrons, AES is sensitive to the chemical environment and chemical shifts can be observed. Auger transitions involving one set of principal quantum numbers exhibit peak splitting due to the different possible combinations of participating sub-shells (i.e. KL_1L_2, KL_1L_3, …) which have different binding energies. In the case of LMM-transitions of 3d transition metals, the resulting peak splitting amounts to more than 100 eV. In specific cases where valence electrons participate in the cascade, Auger peaks exhibit a fine structure that can be used as a chemical fingerprint [22, 23].

2.3 Quadrupole Mass Spectrometry (QMS)

Quadrupole Mass Spectrometry (QMS) [24] is commonly employed in UHV to investigate the composition of the gas phase. Atoms or molecules are ionized, usually by electron impact ionization, and the positively charged fragmentation products are accelerated and focused into the Quadrupole mass filter by an electric field. The mass filter consists of four metal rods aligned parallel and symmetrically around the flight path of the ions. Opposing rods are electrically connected, and a radiofrequency alternating current (AC) voltage offset by a direct current (DC) voltage is applied between them. At certain ratios of DC and AC voltage, the ions of a specific m/z (mass-to-charge ratio) can oscillate through the filter on stable trajectories and reach the detector, whereas all other m/z are deflected. The respective m/z able to pass the filter is proportional to the AC voltage, and the mass spectrum is obtained by either (1) keeping the frequency constant and varying both voltages while keeping their ratio constant or (2) varying the frequency while keeping both voltages constant. The filtered ions are then detected e.g. by a Faraday cup or a channel electron multiplier, resulting in a spectrum where the ion current is plotted versus the respective m/z. In this work, QMS was mainly used prior to FEBIP experiments in order to verify sufficient precursor purity.

2.4 Low Energy Electron Diffraction (LEED)

Low Energy Electron Diffraction (LEED) [25] is a standard surface science technique to determine the long-range order of a crystalline sample and a possible overlaying

superstructure. The sample is irradiated by electrons with kinetic energies of a few up to several hundred eV, corresponding to de Broglie-wavelengths in the order of inter-atomic distances in a crystal lattice. Constructive interference of elastically scattered electrons takes place when the Laue condition is satisfied, giving a diffraction pattern that depicts the reciprocal space lattice of the surface. Inelastically scattered electrons do not contribute to the diffraction pattern, therefore only the first few atomic layers of the sample are probed due to the short inelastic mean free path of the low energy electrons. The diffracted electrons are then accelerated towards a fluorescent screen, from which the diffraction pattern is recorded. LEED was used in this work to qualitatively judge the surface structure.

2.5 Scanning Probe Techniques

2.5.1 Scanning Tunneling Microscopy (STM)

In Scanning Tunneling Microscopy (STM) [26], a sharp metallic tip is raster-scanned over a surface in close proximity (typically several Å), and a tunneling current is measured as a function of the tip position. The basic principle of the tunneling current is the quantum mechanical tunneling effect, which states that unlike in classical mechanics, a particle can overcome a potential barrier which is larger than the energy of the particle. In an STM, the potential barrier is established by the vacuum gap between the two electrodes, tip and sample. Upon applying a potential difference (commonly denoted as bias voltage, U_B), the Fermi levels shift by eU_B with respect to each other, allowing electrons to flow from occupied into unoccupied states by tunneling through the vacuum gap. The direction of the current depends on the polarity of the applied voltage. In a simplified picture, for a very small bias voltage, the tunneling current I_C can be approximated as [27]

$$I_C \sim U_B \rho_S(0,E_F) \exp(-\hbar^{-1}2d\sqrt{2m\Phi})$$

where $\rho_S(0,E_F)$ is the local density of states (LDOS) of the sample surface near the Fermi level, d the distance between tip and sample, m the electron mass and Φ the mean value of the work functions of tip and sample. The exponential dependence of I_C on d leads to a high vertical resolution in the sub-pm regime. As I_C depends on the LDOS, an STM always maps

electronic states of the surface, and in a first approximation these can be correlated to the surface topography.

2.5.2 Atomic Force Microscopy (AFM)

Atomic Force Microscopy (AFM) is another widespread scanning probe technique [28], where a sharp tip mounted on a cantilever is raster-scanned over a surface, and various tip-sample interactions can be probed at each point. This is done by following the tip response, typically by measuring changes in the oscillation behavior (amplitude, frequency, phase) of the cantilever which is oscillating near its resonance frequency. Depending on the tip-sample distance, different forces (e.g. van der Waals, electrostatic, magnetic, capillary) predominate which allows mapping the respective surface properties. In this work, AFM was used measuring in non-contact mode (NC-AFM), in which the tip oscillates in close proximity to the surface but does not get in contact. From the FEBIP perspective, a distinct advantage of AFM is the ability to determine the true surface topography of deposits, unlike in SEM, where the emission of electrons is always influenced by properties not directly related to topographical features, such as work function and atomic number.

2.6 FEBIP techniques

In the following chapters, a brief introduction of the FEBIP techniques utilized in this work is given. These include EBID and EBISA, as well as the autocatalytic growth process, which was the main means in all experiments for material deposition, and is therefore considered as an important expansion of the FEBIP processes despite the absence of an electron beam when AG takes place.

2.6.1 Electron Beam Induced Deposition (EBID)

EBID is a powerful, direct-write method for the controlled, lithographic fabrication of nanostructures on planar and non-planar surfaces, with an extensive amount of possible compositions. The deposition of carbonaceous layers from residual gases in electron microscopes, i.e. beam damage, was already reported in 1934 [29] and long considered only as a nuisance, but an increasing amount of research on the deposition with defined precursors has been conducted beginning in the 1960s [30, 31] and especially in the past
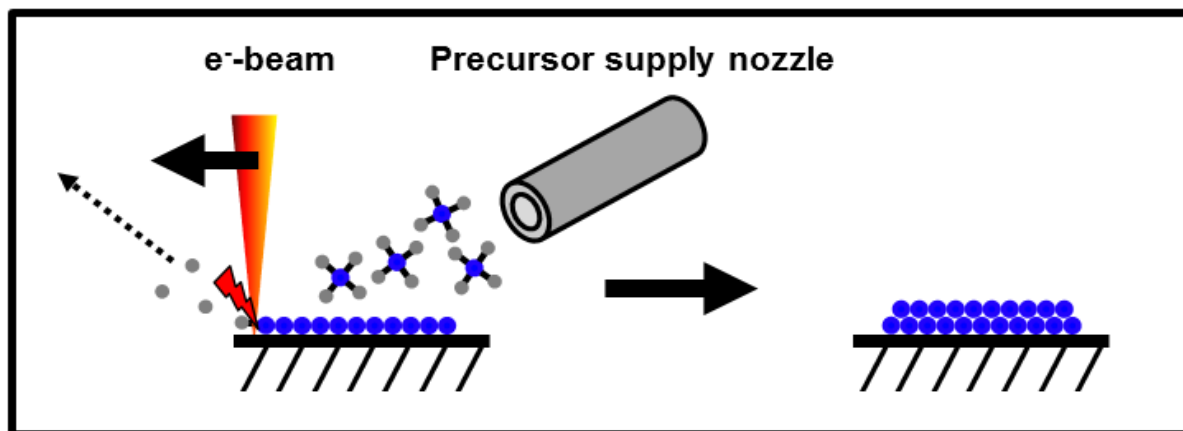
9

Figure 2-1: *Scheme of the EBID process. While scanning over the surface with a focused electron beam, a precursor compound is supplied by means of a nozzle in close vicinity. By the impact of the beam, adsorbed precursor molecules are dissociated, leaving behind a deposit at irradiated areas, whereas volatile dissociation products can desorb into the vacuum.*

two decades. Several review papers concerning FEBIP have been published, to which the interested reader is referred to [5, 6, 32-34]. The EBID procedure is schematically depicted in Figure 2-1. A gaseous precursor compound, typically an organometallic complex, is introduced into the vacuum through the gas phase and supplied onto a substrate, usually through a nozzle that is in close proximity. The focused electron beam of an electron microscope is scanned over the substrate with lithographic control, and upon the impact of PEs and subsequently generated backscattered and secondary electrons, the dissociation of precursor molecules is induced. Volatile dissociation products desorb from the surface and are eventually pumped off the chamber, whereas non-volatile dissociation products remain and form the deposit. The advantage of EBID over the related EBL is the fact that it requires only one processing step, its flexibility, i.e. the ability to fabricate three-dimensional structures, which can consist of a large amount of possible materials due to the large number of available precursor compounds. The deposit size can be, in principle, as small as the beam diameter, and point deposits with a full width at half maximum (FWHM) of < 1 nm have been achieved [35]. A variety of devices have already been fabricated by EBID, amongst many others: Pt field emitter and nanowires from $C_5H_5Pt(CH_3)_3$ [36, 37], Co tips from $Co_2(CO)_8$ for Magnetic Force Microscopy [38], solder connections between carbon nanotubes and microelectrodes from $(CH_3)_2Au(C_5H_7O_2)$ [39], and even mesoscale electron

optics [40]. In the semiconductor industry, EBID is commercially applied as part of a tool to repair photolithography masks [41, 42]. These masks can exhibit nanoscale defects, practically rendering them unusable, which are repaired by adding (EBID) or removing (Electron Beam Induced Etching, EBIE) material.

In general, EBID faces three main challenges: 1) the contribution of backscattered and secondary electrons to deposit formation, called *proximity effects*, 2) the precise control over the chemical composition of the deposit and 3) the low deposition rate compared to nanofabrication techniques such as photolithography, due to the serial nature of the process.

As described in chapter 2.1, the interaction of the electron beam with the substrate leads to the emission of backscattered and secondary electrons which are distributed with radial symmetry around the impact point. The emission can occur up to several µm away from the beam, depending on its energy and substrate properties such as mean atomic number and density. In EBID, PEs can also scatter in already deposited material, leading to the formation of forward scattered electrons (FSE). Upon crossing the substrate-vacuum interface, all these electrons can dissociate precursor molecules, which leads to an unwanted broadening of the deposit. Backscattered and secondary electrons exhibit a wide range of kinetic energies from > 0 eV up to the primary beam energy, and therefore exhibit significantly different cross-sections for the various interactions with precursor molecules. Due to the rather limited amount of quantitative information concerning cross-sections and the statistical nature of electron scattering, making precise and reliable predictions about the contribution of proximity effects to the growth rate is challenging for most systems. This is further complicated by the fact that the deposition of material strongly influences surface properties such as the work function and topography, therefore the emission backscattered and secondary electrons is dynamic during the EBID process. The spatial and energy distribution can be fairly accurately predicted by Monte-Carlo simulations, however, the simulation of the emission of low energy electrons is difficult.

In order to fabricate EBID nanostructures with well-defined properties, predicting and controlling the elemental and chemical composition of the deposit is essential. Most of the reported deposit compositions from metal-organic precursors show a co-deposition of non-metallic impurities, typically carbon, oxygen and/or elements that make up the precursor ligands. The corresponding metal contents can vary, from < 10 at-% (Pt from $C_5H_5Pt(CH_3)_3$, Mo from $Mo(CO)_6$ [43]), ~ 20 – 80 at-% (Co from $Co_2(CO)_8$ [44]) up to > 95 at-% (Fe from $Fe(CO)_5$ in UHV [45]), with a strong dependence on processing parameters such as sample

temperature and beam current. As most EBID experiments are performed in high vacuum environments, the origins of these impurities are usually considered to be surface-adsorbed residual gases (e.g. hydrocarbons), which are dissociated and incorporated during deposition, as well as non-volatile precursor fragments. In order to eliminate the contribution of residual gases as far as possible, one unique approach in this thesis was to perform all FEBIP experiments in a UHV environment. An increasing amount of different methods to purify deposits, either during or post deposition has also recently been demonstrated [46-52].

In order to obtain deposits with defined compositions, a detailed understanding of the growth process on an atomic scale is desirable, which would allow for a knowledge-based adaptation of the processing parameters. This requires the understanding of the various interactions between electrons, precursor and substrate, and merge this knowledge into a theoretical description. However, due to the large number of parameters involved, this is a challenging task. Besides the aforementioned electron-substrate interactions, one has to consider electron-precursor and substrate-precursor interactions. When an electron hits a precursor molecule, a variety of processes that lead to different dissociation pathways can occur [53], such as: electronic excitation, neutral and dipolar dissociation (ND, DD), electron impact ionization, dissociative ionization (DI), electron attachment and dissociative electron attachment. All these processes exhibit different cross sections which depend on the electron energy, with maxima typically at a few eV up to over 100 eV, and it is therefore assumed that low-energy secondary electrons play a crucial role in the deposition process. In addition, the cross sections can strongly differ for various precursor-substrate interactions [54]. Besides this, the precursor-substrate interactions (e.g. diffusion behaviour, adsorption geometry, sticking coefficient) are decisive for the local precursor concentration and therefore the deposit growth rate. As it will be demonstrated in this thesis, the substrate cannot always be considered as a passive agent, but instead it can be catalytically active towards precursor decomposition, depending in some cases even on the actual surface reconstruction. Just as the electron-substrate interactions, electron- and substrate-precursor interactions are dynamic in the EBID process due to the significantly changing surface properties when the deposit is forming.

Despite these challenges, promising progress in modeling the deposition process is being made [55].

2.6.2 Electron Beam Induced Surface Activation (EBISA)

The second FEBIP method used in this thesis, EBISA, was introduced by Walz et al. in 2010 [7] and the recent development of the technique is depicted in a review paper [56]. The procedure is displayed schematically in Figure 2-2. A suitable surface is irradiated with a focused electron beam in the absence of a precursor gas, thereby the irradiated sites are chemically modified such that they become catalytically active towards the decomposition of a subsequently supplied precursor. As a result, a thin seed layer forms at pre-irradiated sites, which can be developed in a secondary, autocatalytic growth process (chapter 2.6.3), where additional material is deposited to obtain solid, voluminous nanostructures.
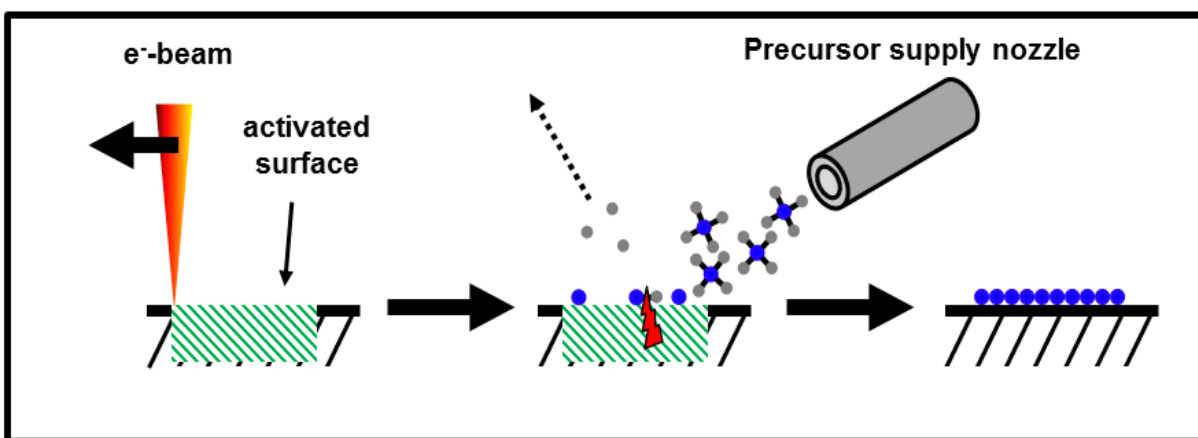

Figure 2-2: *Scheme of the EBISA process. First, the surface is irradiated with a focused electron beam, leading to a chemical modification and therefore catalytic activity. This activity leads to the decomposition of a subsequently supplied precursor and formation of a deposit at irradiated sites.*

Unlike the EBID process, EBISA is more restricted to certain combinations of substrate and precursor, as the electron beam irradiation not always leads to the desired catalytic activity. The first system where EBISA was successfully employed was $Fe(CO)_5$ on a 300 nm $SiO_x/Si(001)$ surface in UHV [7]. In a successive study [8] it was demonstrated that prolonged irradiation of a 0.5 nm $SiO_x/Si(001)$ surface with a 15 keV electron beam leads to a darkening of the substrate in SEM, as well as a decrease in the O_{KLL} signal intensity, followed by deposition of Fe upon exposure to $Fe(CO)_5$. The chemical nature of the irradiated, catalytically active sites was therefore identified as a sub-stoichiometric substrate in the form of SiO_{2-x}, i.e. oxygen vacancies which are generated by electron stimulated

desorption (ESD) of oxygen via the Knotek-Feibelman mechanism [57]. Similar observations were made for $Fe(CO)_5$ on rutile $TiO_2(110)$ 1×1 in UHV ([9], see also chapter 4.1.2): electron irradiation leads to darkening in SEM, decrease in oxygen content on the surface, and a site-selective nucleation was observed with STM after 10 L of precursor exposure, followed by autocatalytic growth. As the nature of the catalytically active sites was thus again identified as oxygen vacancies following ESD via the Knotek-Feibelman mechanism, one might anticipate that at least for $Fe(CO)_5$, oxides are in general susceptible for EBISA. A distinctly different system that was successfully employed is $Fe(CO)_5$ on mono- and multilayers of 2HTPP on Ag(111) in UHV [10]. Here, a closed layer of 2HTPP was used to inhibit the unselective decomposition of $Fe(CO)_5$ on the pristine surface at RT. The EBISA protocol again lead to deposition of Fe, considerably expanding the technique to a new class of substrates. It was further demonstrated that after irradiation with the same primary electron dose, multilayers of 2HTPP exhibit an increased catalytic activity compared to monolayers, which was attributed to a quenching of the monolayer activity by the nearby support.

Performing EBISA in a UHV environment is certainly beneficial due to the lower probability that active sites become passivated by reacting with residual gas molecules, compared to an HV environment. It was indeed demonstrated that in UHV, the catalytic activity after electron beam irradiation is retained for at least two days [7]. However, Muthukumar et al. [58] demonstrated that deposits can also be obtained in HV by using the EBISA protocol with $Co_2(CO)_8$ on SiO_2. These deposits have a metal content of ~ 76 %, and density functional theory (DFT) calculations demonstrate that dissociation most likely starts by a strong dissociative bonding of $Co_2(CO)_8$ to the partially dehydroxylated surface that results from electron irradiation. Furthermore, the concept of site-selective material deposition following electron beam irradiation of self-assembled monolayers (SAMs) has also been demonstrated for other techniques, such as electrodeposition [59] and atomic layer deposition (ALD) [60].
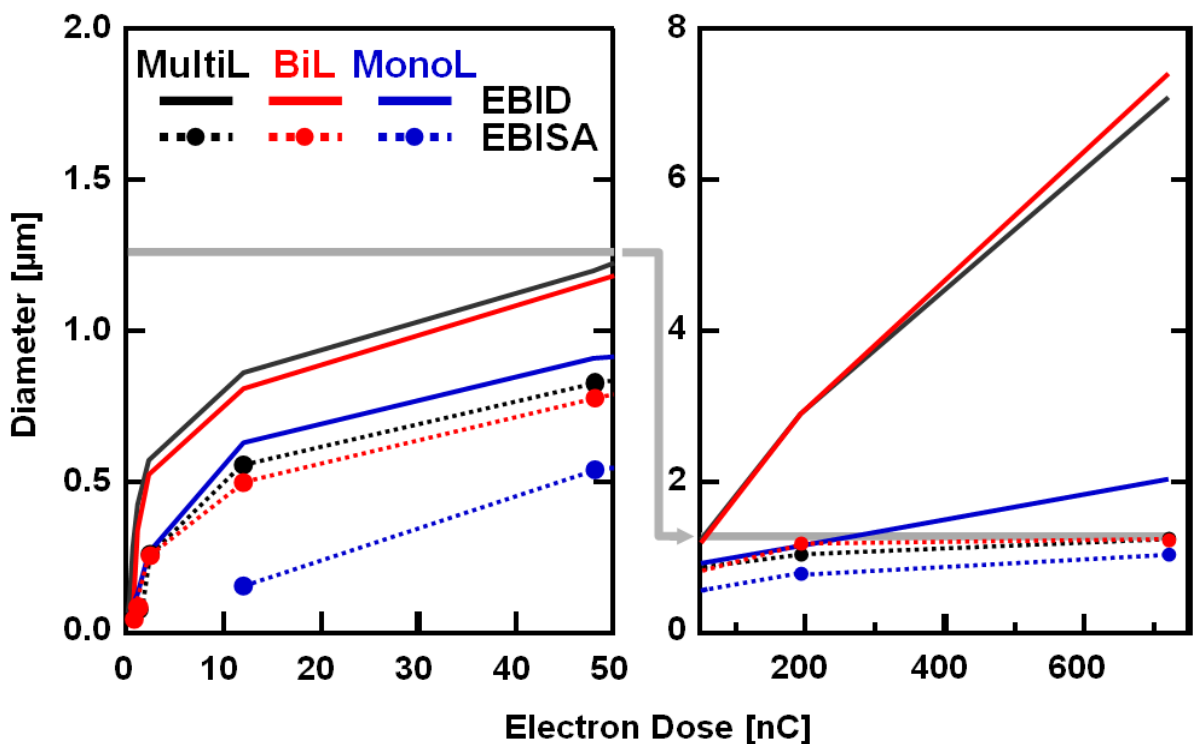
Figure 2-3: Evolution of the diameter of point deposits, in which the electron beam dwells at one pixel, as a function of primary electron dose. The deposits were fabricated by EBID and EBISA with Fe(CO)$_5$ on 2HTPP/Ag(111) with different 2HTPP thicknesses. With increasing electron dose, a logarithmic increase of the deposit diameter is first observed for both techniques, as the maximum diameter of BSE emission is approached. In EBISA, the diameter continues to converge to this value with further increasing electron dose, whereas in EBID, the diameter increases significantly. This is ascribed to the formation of a pillar-shaped deposit at the point of impact of the electron beam, leading to emission of FSE that exceeds the BSE exit diameter. Reprinted from Vollnhals et al. [10].

The fact that in EBISA electron irradiation and precursor dosage are temporally separated leads to some fundamental differences compared to the EBID process. As no electron-precursor interaction takes place and material deposition only occurs via catalytic processes, the growth mechanisms are in principle easier to investigate, both experimentally (e.g. by temperature programmed photoelectron and infrared spectroscopy) and theoretically (DFT), provided the chemical nature of the activated surface is known and is mostly homogeneous. As no material is deposited during electron irradiation, no FSEs are generated, therefore only BSEs, SEs and AEs that originate from the bulk contribute to the

surface activation. This fact has already been proven by following the radius of a point deposit (beam dwells at one position) in both EBID and EBISA as a function of electron dose (see Figure 2-3) and utilized in comparative studies about proximity effects on free-standing 50 and 200 nm Si_3N_4 membranes, Si_3N_4 on bulk Si and SiO_x on bulk Si [61, 62]. The contribution of backscattered electrons is significantly easier to assess by means of Monte-Carlo simulations, which simplifies the theoretical description and prediction of the process.

2.6.3 Autocatalytic growth

In all FEBIP experiments presented in this work, which were throughout performed with the precursors $Fe(CO)_5$ or $Co(CO)_3NO$, autocatalytic growth of the initial deposits took place. Autocatalysis is defined as a chemical reaction in which its catalyst is one of the reaction products [63]. In the case of $Fe(CO)_5$ the simplified, total reaction equation can be expressed as:

$$Fe(CO)_5 + Fe \rightarrow 2\ Fe + 5\ CO$$
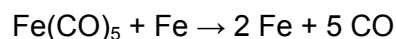
In a FEBIP context, Kunz et al. were in 1987 the first to explain the unexpectedly high deposition yields in EBID deposits fabricated with $Fe(CO)_5$ at 125 °C by thermal, autocatalytic decomposition of $Fe(CO)_5$ on a thin Fe seed layer that was directly formed by electron beam induced dissociation [64, 65]. As a result, polycrystalline, pure bcc α-Fe deposits formed selectively at irradiated sites. The characteristic non-linear growth kinetics in form of an induction period were observed [66]. The autocatalytic growth behavior of $Fe(CO)_5$ was then reported on different substrates even at RT and below, e.g. Pt(111) [67], Rh(110) [68], Ag(111) [10] and in the course of the investigation of EBISA on SiO_x [7] where the high purity of the deposits was confirmed. The chemical composition of the first, initial layer which is either formed by catalytic or electron beam induced decomposition, is less clear. The presence of pure Fe in the first layer might be necessary to induce the autocatalysis, however, in contrast to the crystalline pure Fe that grows on top it exhibits a rather amorphous structure in SEM. A detailed, combined TEM/EDX analysis of this initial growth stage is currently being conducted.

The autocatalytic growth behavior of the second precursor used in this thesis, $Co(CO)_3NO$, was investigated by Vollnhals et al. in a combined SEM-, Scanning

Transmission X-ray microscopy (STXM-) and Near Edge X-ray Absorbtion Fine Structure Spectroscopy (NEXAFS-) study [69]. It was found out that with increasing additional precursor dosage, EBID deposits on a 100 nm Si_3N_4 membrane exhibit an increased brightness and granularity in SEM, and NEXAFS data of deposits with different precursor dosage times verified that autocatalytic growth took place. Additionally, NEXAFS revealed that the cobalt is in an oxidized state, and with additional AES data the authors concluded a deposit composition of $CoO_xN_yC_z$. Interestingly, catalytic decomposition of $Co(CO)_3NO$ and autocatalytic growth was also observed on crystalline iron deposits that were fabricated before, also resulting in a composition of $CoO_xN_yC_z$. In contrast to autocatalytic growth of $Fe(CO)_5$, where catalytic sites can unambiguously be identified as metallic iron, the deposit composition in the case of $Co(CO)_3NO$ appears to be more complex, and the nature of the catalytic activity is still unclear.

Autocatalytic growth is essential in the EBISA process, as no electron beam irradiation takes place and material deposition solely relies on autocatalytic effects. This limits its applicability to certain systems, however, it also offers interesting processing strategies. Firstly, the potential throughput is significantly higher than in an EBID process, since compared to the fairly slow serial deposition in EBID, all structures can grow in size in parallel after activating the surface. Secondly, an increased deposit size in EBISA only requires additional autocatalytic growth time, whereas in EBID, additional electron beam irradiation is required which leads to more pronounced proximity effects and thus widening of the deposit. Thirdly, the amount of possible reaction products in the autocatalytic growth process is very limited, such as in the case of $Fe(CO)_5$ where only metallic iron is formed. This has the advantage that the elemental and even chemical deposit composition can easily be predicted and controlled, unlike in EBID, where the different electron-precursor interactions may lead to distinctly different reaction products. However, autocatalytic growth also has drawbacks. Firstly, since structures are written sequentially in EBID and only the sample as a whole can be exposed to the precursor, the structures will experience different autocatalytic growth times, and therefore different amounts of material are deposited. Secondly, autocatalytic growth can lead to unintended broadening of a deposit.

3 Experimental details

3.1 The UHV instrument

All experiments presented in the work at hand, except for AFM measurements, were conducted in a commercial UHV system (Multiscan Lab, Scienta Omicron). The instrument has been described in detail in previous works [70-72], and its main components will be briefly summarized in this chapter.

The main experimental setup consists of an analysis chamber, where FEBIP experiments/characterization and STM measurements are conducted, and a preparation chamber which contains tools for surface preparation and characterization. Both chambers are connected by a linear transfer rod that includes a gate valve, which allows for quick sample transfer between the two chambers. The preparation chamber is additionally connected to a fast entry lock chamber by a linear transfer tube and a gate valve as well. The fast entry lock chamber can be separately pumped, which allows for swift sample transfer from ambient to UHV and vice versa. A separate, self-constructed UHV chamber (referred to as 'gas dosing chamber') allows purging and monitoring the composition of precursors and gases by QMS before their use in the main chambers. To obtain and maintain UHV conditions, all chambers can be pumped by turbomolecular (TMP) and roughing pumps, ion getter pumps and titanium sublimation pumps. A network of stainless steel tubes for handling gases interconnects the analysis, preparation and gas dosing chambers to the precursor and gas containers.

All chambers are mounted on a bench, which itself rests on four self-levelling damping columns to isolate the system from low-frequency external vibrations.

3.1.1 Analysis chamber

A photograph of the analysis chamber is depicted in Figure 3-1, with its most important parts indicated. The main component is a UHV-compatible SEM column (Gemini, Zeiss [73]), with a minimal beam spot size and thus resolution of 3 nm at 15 kV / 400 pA, as determined by the 80 / 20 criterion on a Au / C sample. A scheme of the instrument is depicted in Figure 3-2. A thermal field emitter is used as an electron source, consisting of a
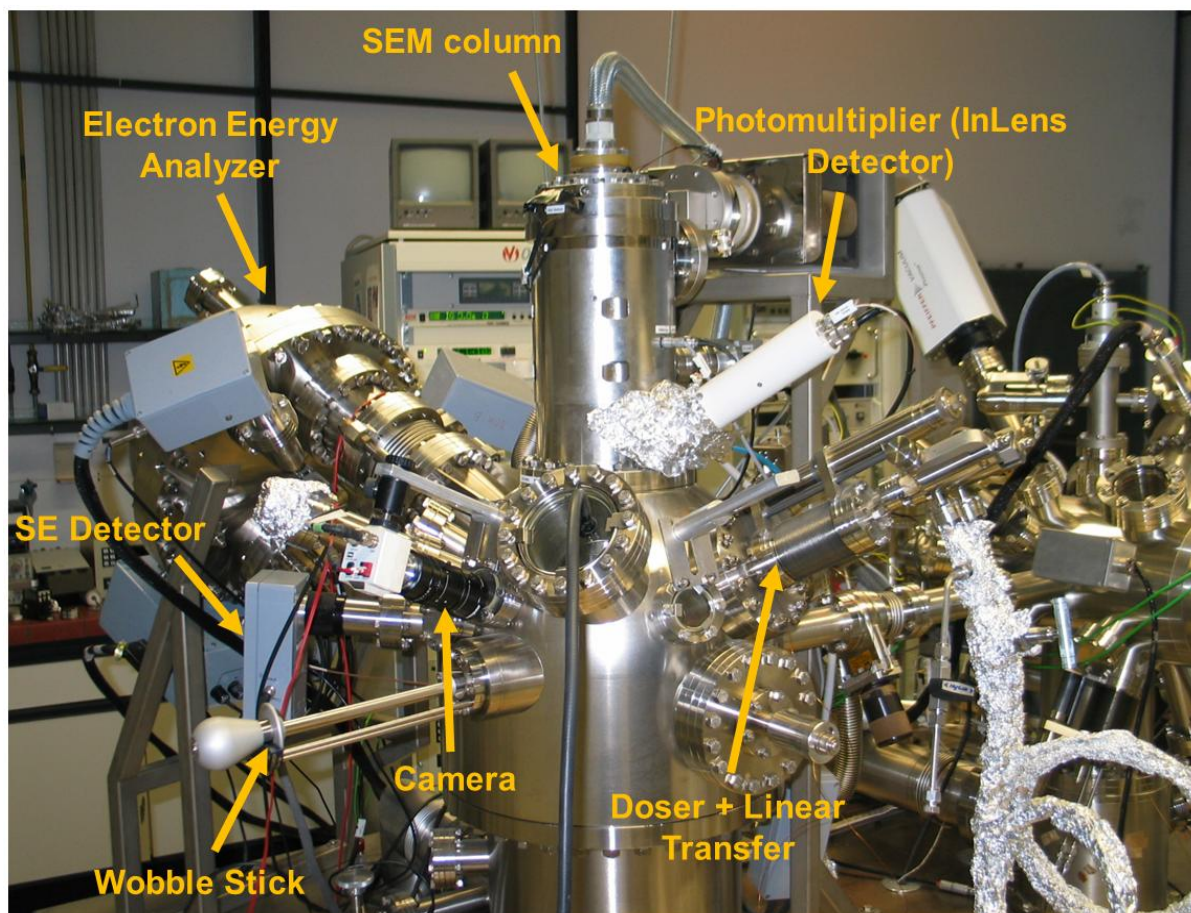
Figure 3-1: *Photograph of the analysis chamber with its most important parts indicated.*

(100)-oriented W tip that is covered by ZrO. The emitted electrons are pre-focused by a suppressor cup before being accelerated by the anode into a series of electromagnetic and electrostatic lenses. For all beam energies < 20 keV, a so-called beam booster unit accelerates the electrons by further 8 kV before entering the lenses, to reduce any aberration caused by magnetic and electric stray fields or lens errors. After the crossover-free focusing, the electrons are again decelerated by 8 kV at the objective lens to obtain the nominal energy. The inlens-detector consists of a scintillator that converts the impinging electrons into photons, which are conducted to a photomultiplier and converted into an electric signal. The objective lens also contains the electromagnetic scan coils which control the beam position during scanning and lithography.
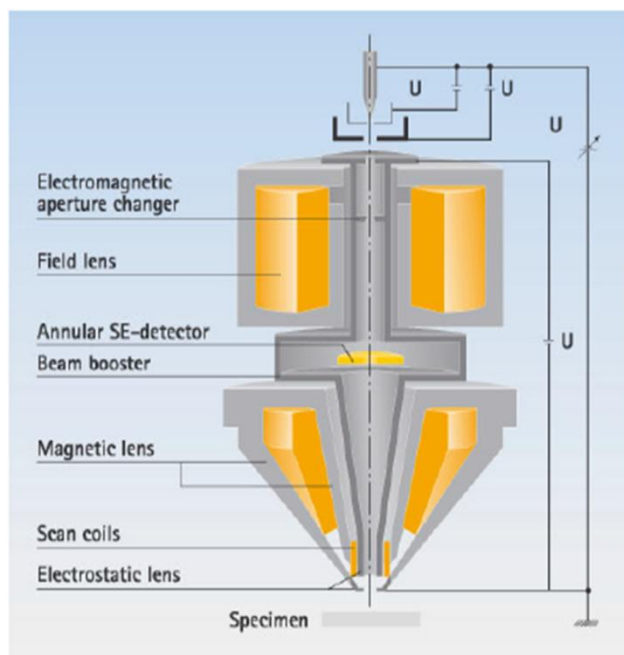
Figure 3-2: *Scheme of the Gemini column components, see text for details. Adopted from ref. [73].*

The hemispherical electron energy analyzer (NanoSAM, Scienta Omicron) required to perform local AES is located next to the SEM column. The entry tube pointing towards the sample consists of a series of electrostatic lenses that focus the emitted electrons into the energy filter and decelerates them to the analyzer pass energy.

The sample stage is located below the SEM column. It is mounted on a goniometer stage allowing a rotation of up to 25° towards the electrostatic lens system of the hemispherical electron energy analyzer to maximize the signal-to-noise ratio. Lateral positioning of the sample is realized by moving the sample with piezo actuators. The sample stage also houses the STM scanner, which is can be positioned between the SEM column and sample. In this work, etched W or self-cut Pt/Ir wires were used as tip materials. The tips are mounted on a tip holder which is inserted into the scanner, and can be attached to a special sample holder and transferred in the UHV system.

A self-constructed retractable nozzle ('doser') pointing towards the sample surface is used to introduce gases (usually the FEBIP precursor). When fully approached, the nozzle exit is ~ 10 mm away from the surface, effectively increasing the local precursor pressure on the surface with respect to the measured background pressure by a factor of ~ 30 for precursors such as $Fe(CO)_5$ and $Co(CO)_3NO$, as estimated with the software GIS [71, 74].

When not in use, the nozzle is retracted from the surface to minimize its influence on measurements and to enable stage rotation.

The analysis chamber houses a two-storey carousel, in which up to twelve sample holders can be stored under UHV conditions and which acts as a receiving end for sample holders transferred from the preparation chamber. A wobble stick enables transfer between carousel and sample stage. Additionally, the chamber houses a QMS (Pfeifer Vacuum, Prisma QMS/QMA200) and another external secondary electron detector.

3.1.2 Preparation chamber

Photographs of the preparation chamber are depicted in Figure 3-3, with its most important parts indicated. A manipulator allows precise sample positioning with respect to the corresponding instruments and houses the necessary connections for sample heating and cooling. The chamber consists of several common surface science tools for surface preparation and characterization: A sputter gun (Scienta Omicron, ISE 10), LEED optics (Scienta Omicron, SPECTALEED), a quartz crystal microbalance (Syscon, OSC-100A), an electron beam metal evaporator (Focus, EFM 3i) and a self-constructed electron flood gun.
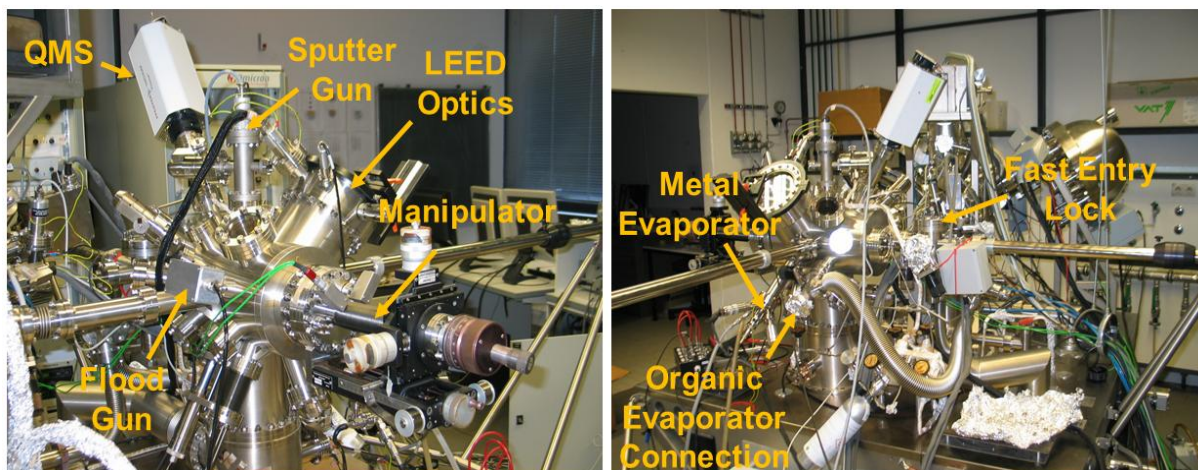

Figure 3-3: Photographs of the preparation chamber with its most important parts indicated.

A self-constructed Knudsen cell evaporator for organic materials was originally directly flanged to the chamber. In order to be able to replace the evaporator material without breaking the vacuum, the evaporator was relocated as part of this work. Figure 3-4 depicts
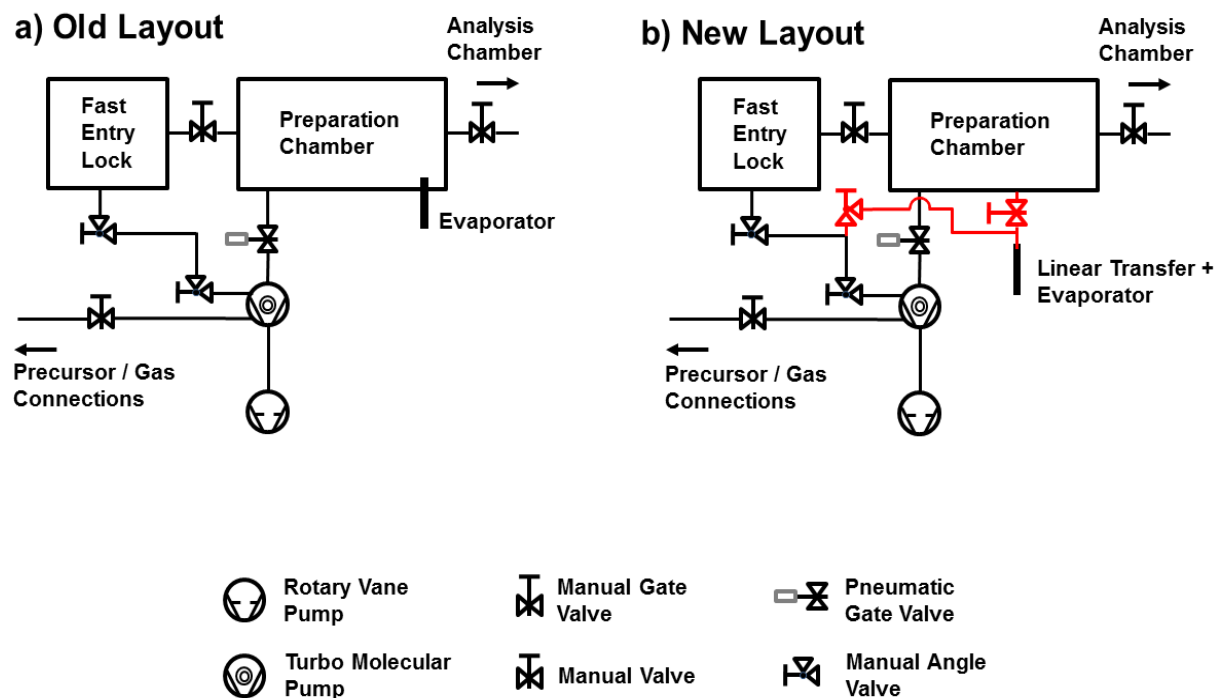
Figure 3-4: *Scheme of the relevant vacuum system connections a) before and b) after relocation of the Knudsen cell evaporator. Red indicates new components.*

schematics of the corresponding connections before and after the modification. Instead of being directly connected, the evaporator is separated from the chamber by a manual gate valve, a T-piece and a linear transfer. The T-piece between gate valve and linear transfer connects to a flexible tube, which itself connects via a manual angle valve to the line between preparation chamber TMP and fast entry lock (all connections CF40). This way the evaporator part can be pumped down independently via the preparation chamber TMP, and the evaporator can be positioned in the chamber with the linear transfer. To ensure the same distance between evaporator head and sample as before the modification, the evaporator was extended accordingly by refitting the thread bars and heating/temperature readout connections.

3.1.3 Sample Holder

Different types of sample holders were used during this work, depending on the sample geometry and temperature requirements during preparation. Samples that do not require heating and/or had an arbitrary geometry (some SURMOF samples) were mounted on a
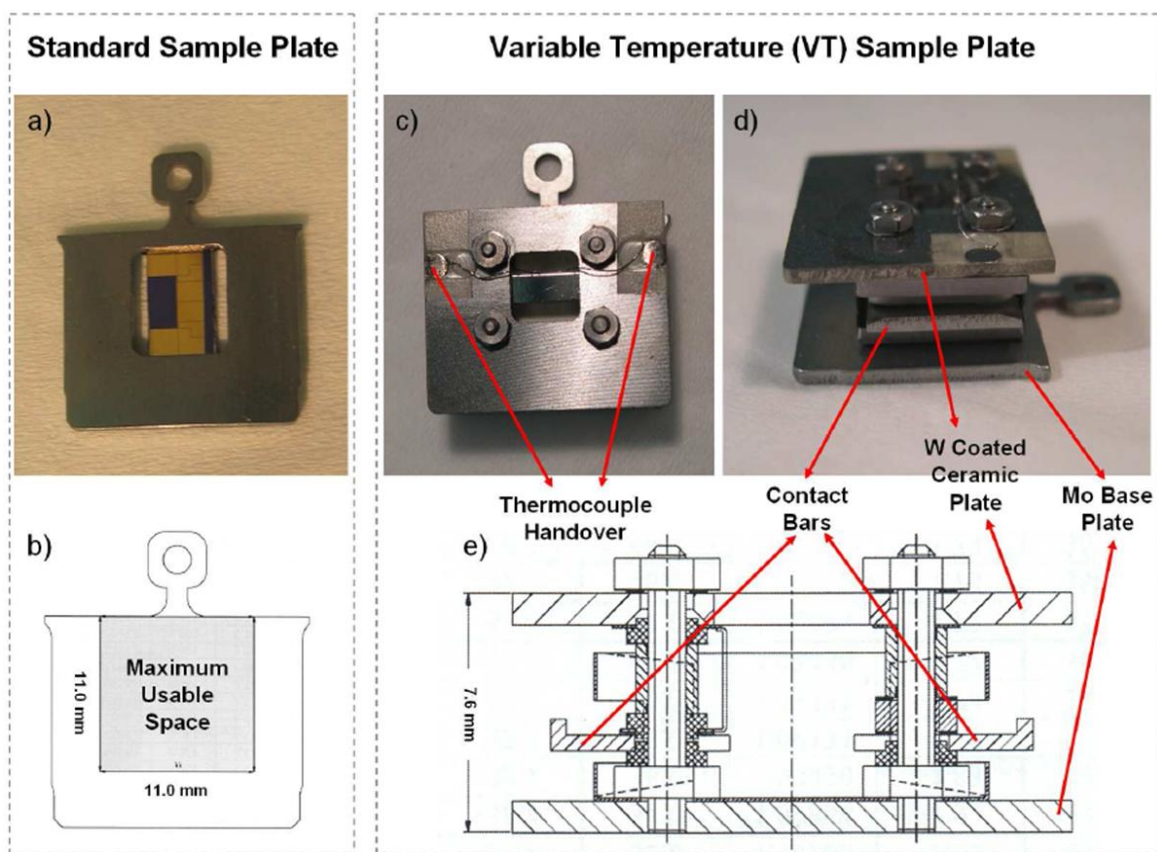
Figure 3-5: *a, b) Photograph and scheme of a standard single plate sample holder with window; the outer parts of the plate must not be covered in order to not interfere in the transfer process; c-e) photographs and scheme of a VT sample holder for a resistive heating setup; the electrical contact to the manipulator is realized via the contact bars; other setups include a PBN element or a W filament between both contact bars for radiative and electron beam heating respectively. Adopted from ref. [70].*

simple Ta plate (photo in Figure 3-5a), spot-welded with Ta foil below a rectangular window in the centre of the plate. Using two-storey sample holders (Figure 3-5c-e, 'VT (variable temperature) sample holders') allows heating a sample by different methods. These sample holders consist of a Mo base plate, with four threaded rods attached perpendicular to it. These rods hold all parts for the respective electrical connections/isolations, and the sample is fixed below another plate with window that is on top of the assembly. The ceramic top plate is covered with tungsten to prevent charging, e.g. when conducting LEED or SEM. The top plate also houses the thermocouple contacts.

In a resistive (direct) heating setup (used for Si samples, as depicted in the scheme in Figure 3.5e), a current flows directly through the sample, thereby heating it. In a PBN (pyrolitic boron nitride) heating setup, a current flows through a PBN element that is located below the sample, and the sample is heated by the emitted radiation. In an electron beam heating setup, a current flows through a W filament that is located below the sample. The filament is electrically isolated from the rest of the (grounded) sample holder. By applying a negative high voltage to the heated filament, the emitted electrons are accelerated towards the back of the sample and thereby heating it.

3.2 AFM instrument

AFM measurements were conducted under ambient conditions with an easyScan DFM instrument (NanoSurf). A silicon tip mounted on a cantilever was used in the non-contact dynamic force mode (DFM). In DFM, the tip is oscillating close to its resonance frequency and the amplitude changes due to the tip-surface interactions are measured, and a feedback loop regulates the amplitude to a constant value. The instrument sits on a damping table (Table Stable TS-150, HWL Scientific Instruments) to isolate it from vibrations.

3.3 Samples and precursors

3.3.1 Si(111)

Si(111) samples were purchased from the Institute of Electronic Materials (Warsaw). They come as 1 mm × 10 mm pieces, laser-cut into a 0.5 mm thick, polished wafer. Resistive heating was applied to remove carbonaceous impurities and the native oxide layer that forms when exposed to ambient conditions. The heating procedure consists of heating to 1000 K for ~ 3 h, and flash heating afterwards (5 × 5 s at each temperature) to 1200 K, 1330 K, 1430 K, and 1500 K. The surface quality was assessed by LEED, AES and SEM, as well as STM if the surface was subject to further STM studies, e.g. investigation of porphyrin adsorption behaviour. Temperature readout was conducted with a pyrometer (ε = 0.67).

3.3.2 TiO$_2$(110)

Rutile TiO$_2$(110) single crystals were purchased from CrysTec (Berlin). The 5 mm × 10 mm plates are initially yellow-transparent. TiO$_2$ is one of the most investigated of all metal oxides in surface science and has been thoroughly reviewed [75]. Heating in vacuum induces bulk defects which make the crystal conductive, opening up a variety of surface science techniques that would otherwise not be possible due to charging. The crystal colour changes from yellow-transparent over light blue to black upon increasing annealing times. Sample preparation was performed by alternate Ar ion sputtering (E = 1 keV, p = 4 × 10^{-6} mbar) and annealing by e-beam heating to 1040 K and 1080 K to obtain the 1×1 and 1×2 reconstructed surfaces respectively. The sputtering and annealing times were correspondingly adjusted depending on the state of the surface, which was assessed by LEED, AES, SEM and STM. Temperature readout was conducted with a pyrometer (ε = 0.20).

3.3.3 Cu(111)

A Cu(111) single crystal (2 mm × 10 mm) was purchased from Surface Preparation Laboratories (Zaandam, Netherlands). Surface preparation was done by alternate Ar ion sputtering (E = 1 keV, p = 4 × 10^{-6} mbar) and annealing to 850 K for 30 min on a PBN heater. The new crystal was sputtered for 120 min for initial preparation, and 10 min when only removing the copper oxide layer (chapter 4.4). The surface was again assessed by LEED, AES, SEM and STM. Temperature readout was conducted with a type K thermocouple spot-welded to the crystal.

3.3.4 Surface-Anchored Metal-Organic Frameworks (SURMOFs)

SURMOFs [76] are metal-organic frameworks (MOFs) [77, 78] which are epitaxially grown on a surface. They consist of coupling units, usually metal ions, linked together by organic linker molecules to form a highly porous framework. These can be employed as materials e.g. for gas storage, purification, separation, as well as catalysis [79-82]. In this regard, the ability to precisely tune properties, such as the pore size, by varying the building blocks is a distinguished advantage of MOFs. In 2009, Shekhah et al. presented a procedure to mount MOFs on a Au substrate covered with a self-assembled monolayer

(SAM) [83], as depicted in Figure 3-6. By alternating dipping of this substrate in separate solutions containing the metal ions and organic ligands, SURMOFs can be grown epitaxially in a controlled layer-by-layer fashion. This method gives even more control over the composition of the framework, as solutions containing different building blocks can be used during the framework buildup, as opposed to the conventional solvothermal synthesis of MOFs, where the solutions containing the building blocks are mixed at elevated temperatures.
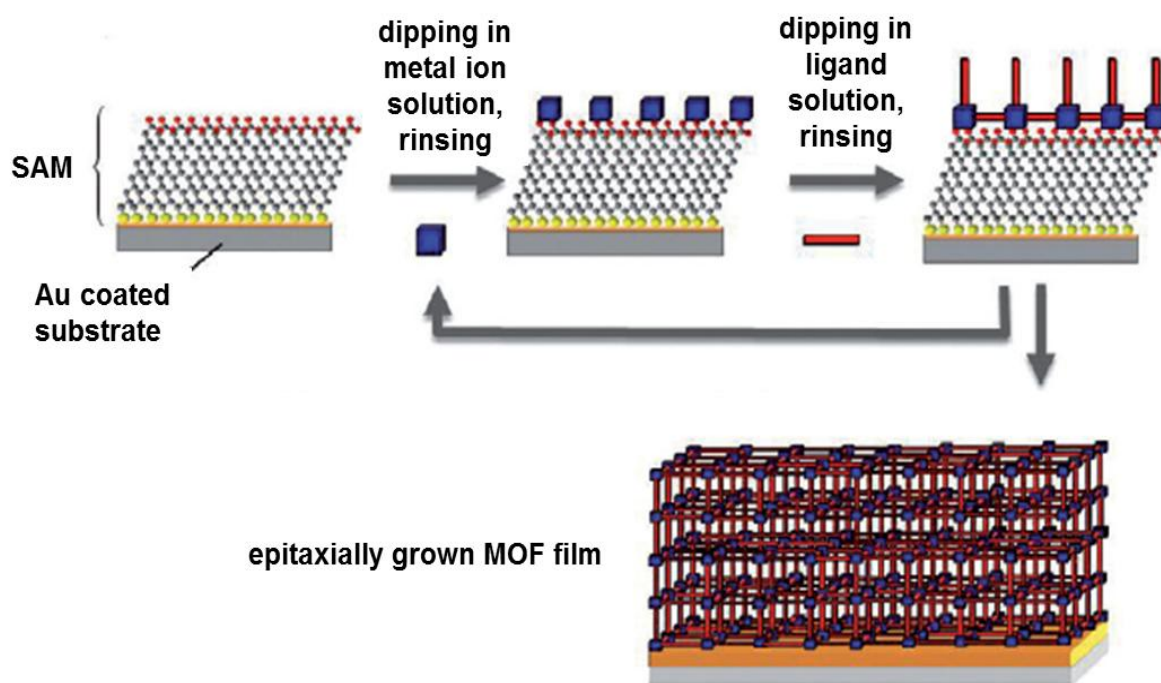

Figure 3-6: *Scheme of the epitaxial layer-by-layer growth of SURMOFs on a SAM-coated Au substrate, by alternate dipping into solutions containing the framework building blocks. This method gives full control over the composition and thickness of the SURMOF layer. Adopted from ref. [76].*

In a collaborative effort, SURMOF samples were prepared by the group of Prof. C. Wöll and Dr. H. Gliemann at the Karlsruhe Institute of Technology (KIT), Karlsruhe. The samples were then used as substrates for FEBIP experiments in Erlangen. These have been conducted on two different SURMOFs: Copper benzene-1,3,5-tricarboxylate (HKUST-1 [84],

Figure 3-7a) and Zinc 5,15-diphenyl-10,20-di(4-carboxyphenyl)porphyrin (DPDCPP/Zn [85], Figure 3-7b). HKUST-1 was chosen as it is a very well investigated (SUR)MOF, and because it exhibits a relatively smooth surface. It consists of benzene-1,3,5-tricarboxylate (btc) linker units which coordinate Cu(II) ions and form dicopper(II)tetracarboxylate ('paddlewheel') units, where each copper centre is additionally coordinated by one water ligand, to form a network with pore diameters of 9.5 – 13.3 Å [86]. DPDCPP/Zn also consists dizinc(II)tetracarboxylate paddlewheel structures, however these link the porphyrin units to form two-dimensional sheets, which are not interconnected and are oriented parallel to each other, perpendicular to the surface. It was chosen due to its similarity to 2HTPP, which, in form of mono- and multilayers on Ag(111), has been demonstrated to be a suitable

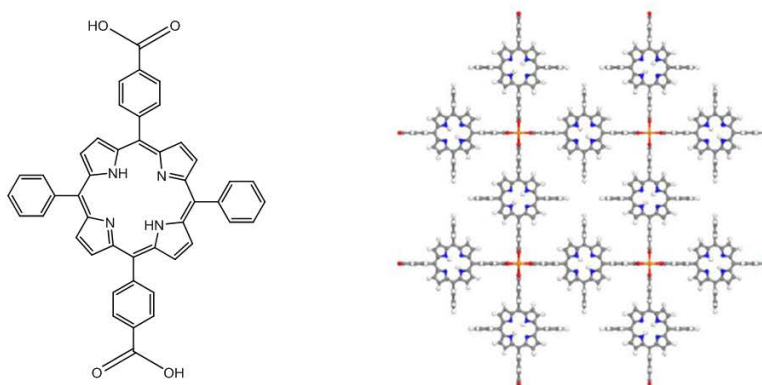**a) HKUST-1**
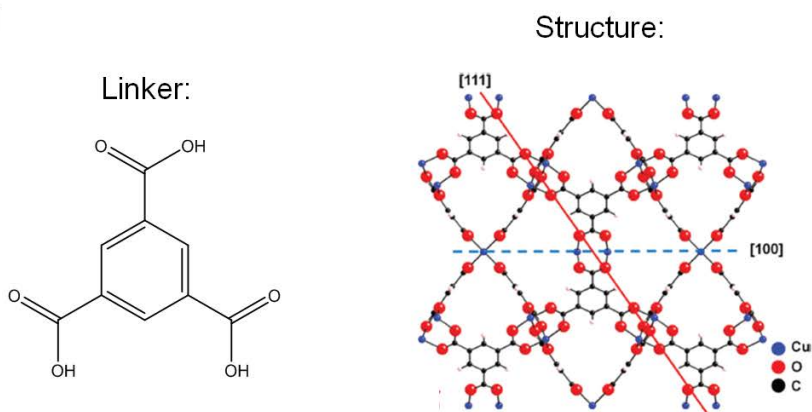
Linker:

Structure:

b) DPDCPP/Zn

Figure 3-7: *a) The HKUST-1 linker unit benzene-1,3,5-tricarboxylic acid, and the corresponding MOF structure, adopted from ref. [84]; b) the Zn-DPDCPP linker unit 5,15-diphenyl-10,20-di(4-carboxyphenyl)porphyrin, and the MOF structure (side-view on one sheet), adopted from ref. [85].*

substrate for EBID and EBISA [10]. With this in mind, one objective is to find out potential similarities and differences between Zn-DPDCPP and 2HTPP in FEBIP, such as the suitability for the EBISA process, i.e. the possibility to locally form catalytically active species after electron beam irradiation.

3.3.5 $Fe(CO)_5$

$Fe(CO)_5$ was purchased from ACROS Organics. It was chosen as a precursor due to its ability to grow autocatalytically at RT, resulting in practically pure Fe deposits, and its ease of handling due to its relatively high vapor pressure and stability. The orange liquid is sensitive to air and UV light, and was therefore filled into a glass/stainless steel hybrid vessel in a glove box under N_2 atmosphere, and the container was permanently wrapped in aluminium foil. Prior to each FEBIP experiment, the stainless steel line connecting the
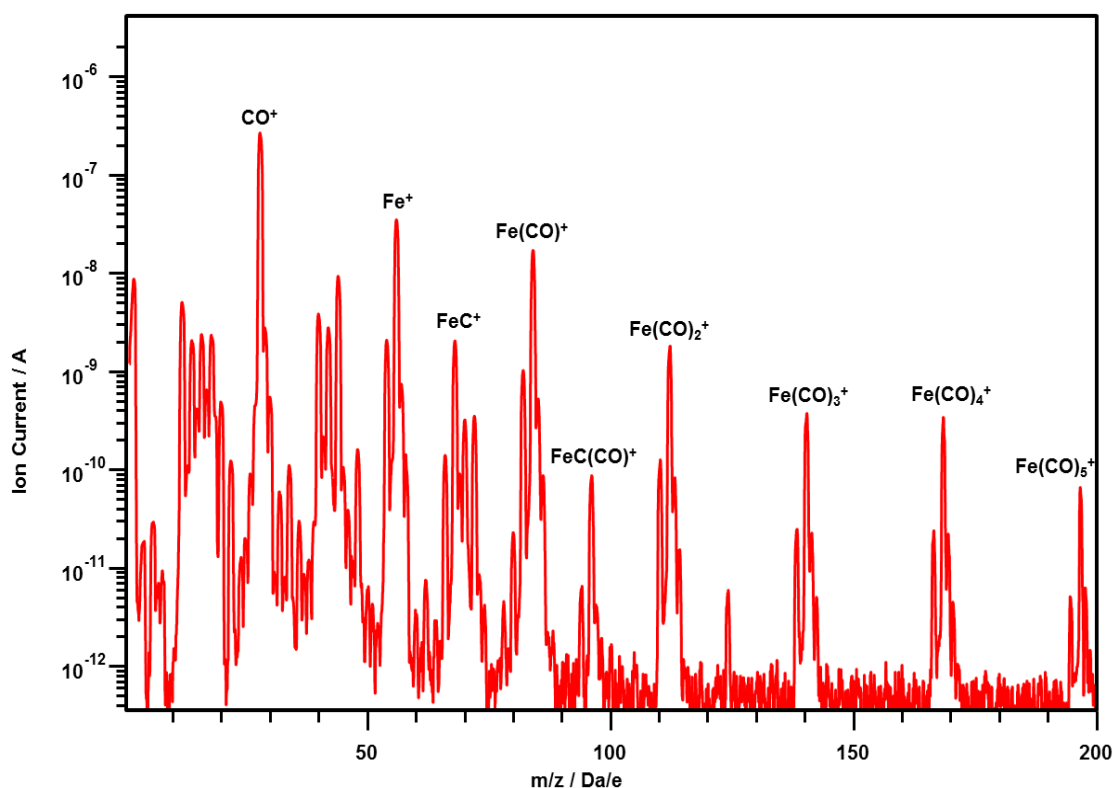

Figure 3-8: *Exemplary mass spectrum of $Fe(CO)_5$, as recorded in the gas dosing chamber prior to a FEBIP experiment, with the most important fragments indicated.*

28

container and the analysis chamber was purged with gaseous $Fe(CO)_5$ several times, and afterwards a mass spectrum of the gas was recorded in the gas dosing chamber. A typical mass spectrum is depicted in Figure 3-8, with the most important fragments indicated. As a measure for the precursor purity, the intensity ratio of Fe^+/CO^+ ($m/z(Fe^+)$ = 56 Da/e, $m/z(CO^+)$ = 28 Da/e) was used: it was found that a ratio of at least 0.05-0.10 is required for autocatalytic growth.

3.3.6 Co(CO)₃NO

$Co(CO)_3NO$ was purchased from abcr. It also has the ability to grow autocatalytically at RT, and is easy to handle. Like $Fe(CO)_5$, the dark brown liquid is sensitive to air and was handled under protective gas. Preparation prior to a FEBIP experiment was the same as with $Fe(CO)_5$, and Figure 3-9 depicts a typical mass spectrum with the most important

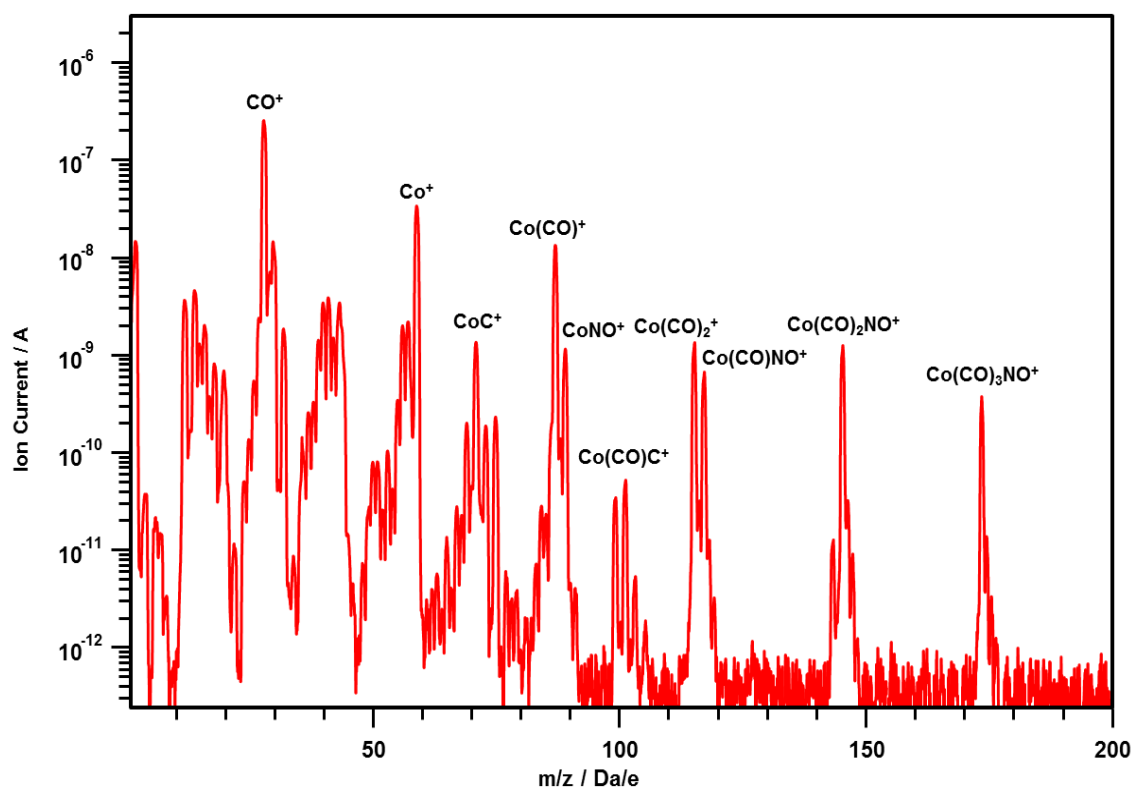**Figure 3-9:** *Exemplary mass spectrum of Co(CO)₃NO, as recorded in the gas dosing chamber prior to a FEBIP experiment, with the most important fragments indicated.*

fragments indicated. The intensity ratio Co^+/CO^+ ($m/z(Co^+)$ = 59 Da/e, $m/z(CO^+)$ = 28 Da/e) was again used as a measure for the precursor purity. In all experiments, a ratio > 0.15 was observed, and autocatalytic growth always occurred.

3.4 Lithography

3.4.1 Fundamentals

Electron beam positioning was controlled via a self-programmed, LabVIEW 8.6 (National Instruments) based software package ('Nanoscribbler') developed by F.Vollnhals. The interested reader is referred to ref. [72] for an extensive description. The SEM hardware (Zeiss) contains external scan inputs to control the beam position in x- and y-direction. The inputs accept two DC voltages from -10 V to +10 V, one for each direction. The maximum extent of the beam deflection is always given by the current field of view selected in the SEM software. The input voltages are generated by a PCIe-based digital-analog-converter (DAC) card with 14 bit resolution, meaning it accepts values from -2^{13} ($\triangleq$ -10 V) to $+2^{13}$ ($\triangleq$ +10 V) and converts these values to the corresponding voltage. The minimum possible step size is therefore the field of view divided by 2^{14}. The beam dwell time per pixel (t_d) at each surface position is restricted by the minimum (1 kHz) and maximum (60 MHz) sampling rates of the DAC card, which can additionally only be adjusted in increments of 1 kHz. In principle, this limits the minimum and maximum dwell times to ~16.7 ns (60 MHz) and 1 ms (1 kHz), therefore a dedicated timing program was implemented that allows using practically arbitrary dwell times [72].

The software package contains several sub-programs to fabricate different patterns, e.g. squares, lines, points etc. These sub-programs calculate the corresponding data pairs for beam deflection in x- and y-direction, and sampling rates, based on the user input. Together with additional exposure information (exposure time (remaining), electron dose etc.) the data is part of a global cluster variable, which is processed by a dedicated sub-program that controls the data transfer to the DAC card.

3.4.2 Fabrication of arbitrary shapes

During the work at hand, a LabVIEW program ('bitmap exposure.vi') was developed and used which allows writing arbitrary shapes in the FEBIP process. By using a bitmap file (*.png format only) consisting of 8-bit grey value pixels (RGB colour space) as an input, the electron beam raster-scans the surface from top left to bottom right, according to the position of the pixels in the input file. White pixels (RGB value 255) do not get irradiated, and the dwell time of grey/black pixels scales with the RGB grey value, with black pixels having the highest dwell time. This allows a flexible adjustment of dwell times of individual pixels, e.g. to compensate for proximity effects. Figure 3-10 depicts a simple input file consisting of 5 × 5 pixels with varying RGB grey values, which are given next to the image. In the 24-bit RGB (**r**ed, **g**reen, **b**lue) colour space, colours are represented by three 8 bit values, i.e. 256 values for each of the three colours. A value of 0/0/0 is black, 255/255/255 is white. As grey colours have the same value in all three colour channels, they can be represented by one value. Note that the code requires the input file to have the same amount of pixels in width and height (can be filled up with white pixels if necessary).

In the following, a description is given on how the size of the resulting deposit is calculated as a function of the step size input, as well as how the dwell time per pixel is calculated as a function of its RGB value and user inputs.
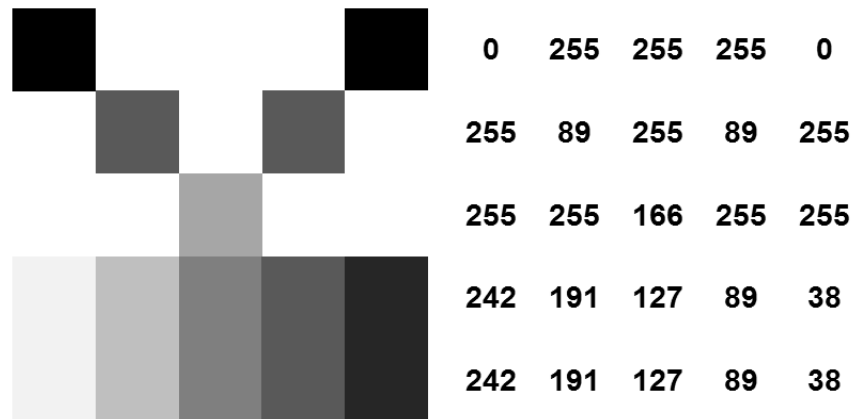

Figure 3-10: *Left: exemplary bitmap input pattern for the 'bitmap exposure.vi', consisting of pixels with varying grey scales, including black and white; right: RGB grey values of the corresponding pixels.*

Deposit size. The size of the resulting deposit is given by the 'step size' input Δx and number of (irradiated) pixels in the input file. Δx determines the distance between the centre of two neighbouring pixels, i.e. how far these pixels will be irradiated away from each other on the surface. As an example, when using a step size of 10 nm, the distance between the centres of the two black pixels in the top row in Figure 3-10 will be 40 nm, as there are three (white) pixels between them; the distance between each pixel is 10 nm, therefore 4 × 10 nm

RGB:	colour:	Input: grey scales			
		2	4	8	16
255	white	0	0	0	0
254					1
				1	2
			1		3
				2	4
					5
				3	6
					7
⋮		1	2	4	8
					9
				5	10
					11
				6	12
			3		13
				7	14
0					15
		Base dwell time multiplier			

Figure 3-11: Dwell time calculation as a function of RGB value and selected grey scales. Each pixel will be irradiated by the base dwell time $t_{d,base}$ multiplied with a factor (highlighted green) that depends on the RGB grey value of the pixel (left) and the selected number of grey scales n (top, highlighted yellow). See text for detailed description.

= 40 nm. The user has to make sure that the field of view selected in the SEM software is at least as big as the irradiated pattern, otherwise it will be distorted. The pattern will always be irradiated in the centre of the current scan area.

Dwell time calculation. The dwell time of each pixel is calculated by its RGB grey value and the 'base dwell time' ($t_{d,base}$) and 'grey scales' (n) inputs. Their correlation is depicted in Figure 3-11. The selected number of grey scales determines how many different dwell times are possible at most, and these dwell times will always be integer multiples of $t_{d,base}$. This multiplier depends on the RGB grey value, which is depicted to the left in Figure 3-11 along with the corresponding colour scale from white to black. For white pixels, the multiplier is always zero, therefore the pixel will not be irradiated. All other RGB grey values from 254 to 0 are assigned to a certain multiplier using the following formula:

$$[t_{d,base} \text{ multiplier}] = \frac{(255 - \text{RGB grey value})}{255} \times (n - 1)$$

i.e. the resulting value always gets rounded up to the next highest integer, if not an integer itself. Thus, when using n = 2, all non-white pixels will be irradiated with $t_{d,base}$, as the multiplier is always 1. It is important to keep in mind that when using n > 2, the dwell time of a black pixel does *not* equal $t_{d,base}$, but $t_{d,base} \times (n - 1)$.

Future expansions of the program might include calculating the resulting BSE densities based on the current bitmap input, based on Monte-Carlo simulations (similar to what is demonstrated in chapter 4.1.3 for a simple square pattern). This would allow a more sophisticated compensation for proximity effects before the FEBIP process, without having to optimize the structure in multiple experimental iterations.

3.5 Data acquisition and processing

SEM data was recorded with SmartSEM (Zeiss) and saved in the *.tif format. For improved visibility of certain features, contrast and brightness were adjusted in some images. AE spectra were recorded with MATRIX 3.1 (Scienta Omicron), and further processed with Igor Pro 5.05A. The raw data was smoothed by box smoothing, i.e. simple averaging, usually with an influence radius of five neighbouring points. Peak areas were determined by numerical integration after linear background subtraction. Differential peak

heights were determined by measuring the difference between minima and maxima of the respective peak in the derived spectrum. STM data was recorded with MATRIX 3.1 (Scienta Omicron) and processed with WSxM. QMS data was recorded with Quadstar (Pfeiffer Vacuum). AFM data was recorded with easyScan DFM 2.0.

The determination of line deposit FWHM was done with line profiles that were measured perpendicular to the lines, as depicted in Figure 3-12a. The baseline value ($\triangleq$ 0% Intensity) was defined as the mean value of the two adjacent minima.

The radius of a dot deposit was defined as the distance between the electron impact point and the point where the SEM brightness drops to 10% of its maximum value in an average radial profile, as depicted in Figure 3-12b. This method was applied as the deposit edge in several measured point deposits was not well-defined, but rather consisted of a gradually decreasing amount of crystalline material, making it difficult to evaluate an exact radius using an SE micrograph only.

Line and radial profiles were determined with ImageJ 1.33u, using a radial profile plugin.

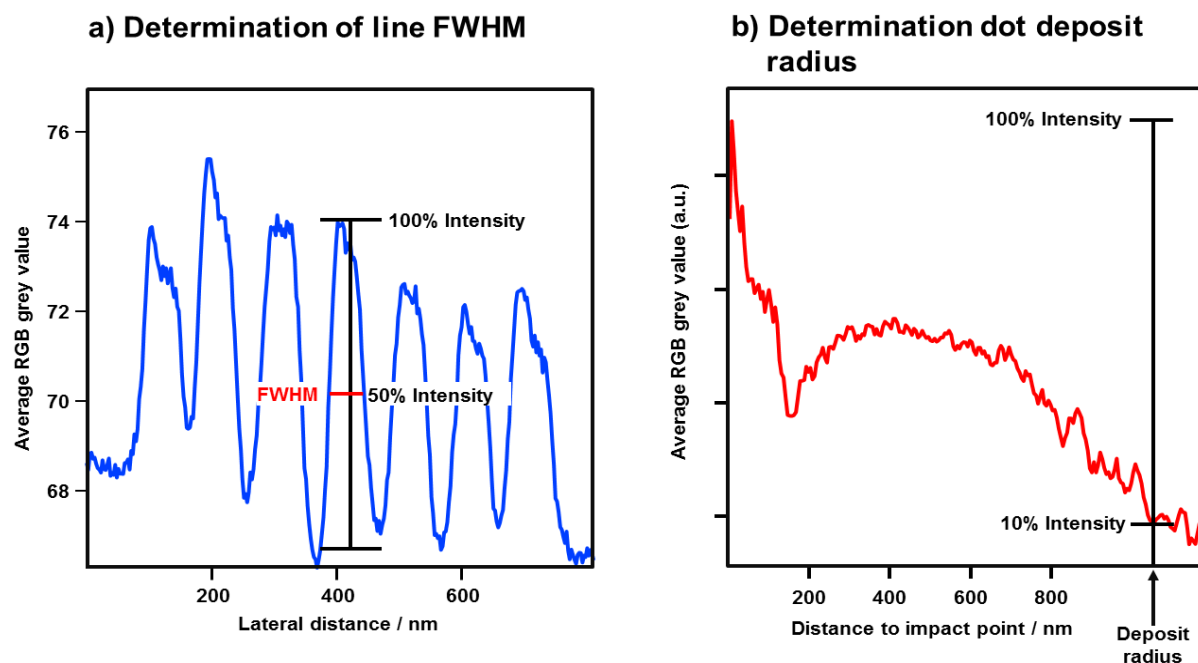**a) Determination of line FWHM**   **b) Determination dot deposit radius**

Figure 3-12: a) Line profile perpendicular to seven lines that were deposited by EBID. To determine the FWHM, the baseline was defined as the average value of the two minima adjacent to the respective line; b) radial profile over an EBID point deposit. The deposit radius is defined as the point where the SEM brightness intensity drops to 10% of its maximum value.

34

4 Results and discussion

4.1 FEBIP on pristine and 2HTPP-covered rutile TiO$_2$(110) and Si(111)

4.1.1 Introduction

In a recent study, Vollnhals et al. [10] have demonstrated that the catalytic activity of a Ag(111) surface towards the spatially unselective decomposition of Fe(CO)$_5$ at RT in UHV can be inhibited by pre-covering the surface with a thin, closed layer of 2HTPP. On this layer, it is then possible to selectively fabricate clean Fe nanostructures using either the EBID or EBISA procedure and autocatalytic growth with Fe(CO)$_5$. This finding considerably increased the scope of EBISA, as it was shown for the first time that a non-oxidic, that is an organic surface, can be activated correspondingly. However, as so far EBISA has been demonstrated to work only with Fe(CO)$_5$ [7] and Co$_2$(CO)$_8$ [58], the motivation of the following study is also to verify whether Co(CO)$_3$NO is suitable for EBISA on organic layers, as it has been shown to grow autocatalytically on EBID deposits on SiOx/Si$_3$N$_4$ at RT [69], but EBISA experiments on native SiO$_x$ on Si(100) and Si$_3$N$_4$ were not successful, i.e. no material deposition was observed.

In the first part of this chapter, the concept of surface passivation is expanded by showing that a thin, closed 2HTPP layer prevents the unselective decomposition of Co(CO)$_3$NO on rutile TiO$_2$(110) 1×1 and Si(111) 7×7, again at RT in UHV. Nanostructures from Co(CO)$_3$NO can then be fabricated on the 2HTPP covered substrates with high site selectivity, using EBID and EBISA protocols and subsequent autocatalytic growth, showing the first time that Co(CO)$_3$NO is suitable for EBISA. This procedure is compared to FEBIP experiments on the same substrates with the precursor Fe(CO)$_5$, where the deposition is site selective on both the pristine and the 2HTPP covered substrates. Additional FEBIP experiments performed on the 1×2 reconstructed TiO$_2$(110) reveal that in contrast to the 1×1 surface, EBID with Co(CO)$_3$NO is spatially selective, whereas Fe(CO)$_5$ dissociates and nucleates at 1×2 strands.

During the investigation of FEBIP deposits fabricated on 2HTPP covered substrates it was observed that most deposits, fabricated with either Co(CO)$_3$NO or Fe(CO)$_5$, exhibit a pronounced SEM brightness difference between periphery and interior of the structure, with a sharp, defined boundary between these two areas. In the second part of this chapter, a detailed spectro-microscopic analysis and an attempt to explain the formation of these areas is presented. It is shown that while the periphery contains significant amounts of carbon, the interior part contains none. In the third part of this chapter, it will further demonstrated that both areas exhibit different catalytic activities towards decomposition of the respectively other precursor that is subsequently supplied, leading to the formation of stepped pyramid shaped, layered structures upon alternate dosing of Co(CO)$_3$NO and Fe(CO)$_5$.

FEBIP experiments were performed with Co(CO)$_3$NO and Fe(CO)$_5$ on different substrates: Rutile TiO$_2$(110) 1×1 and 1x2, Si(111) 7×7, and both TiO$_2$(110) and Si(111) covered with a multilayer of 2HTPP with a thickness of 0.5 - 1.0 nm (2-3 layer). The autocatalytic growth time for all EBISA structures was 270 min, and is indicated in the corresponding captions. The background pressure during all precursor exposures was 3.0 × 10^{-7} mbar, corresponding to a local pressure of approximately 9.0 × 10^{-6} mbar at the sample surface (see chapter 3.1.1). For all deposits presented in this chapter 4.1, the electron beam energy was 15 keV and the nominal beam current 400 pA in EBID and 3 nA in EBISA processes.

4.1.2 Catalytic effects and passivation of rutile TiO$_2$(110) and Si(111)

TiO$_2$(110) 1×1 and 1×2. Summarized in Figure 4-1 are SE micrographs of FEBIP deposits from (CO)$_3$NO (a-c) and Fe(CO)$_5$ (d-f) on TiO$_2$(110) 1×1. Figure 4-1a and b depict square (4×4 µm²) deposits, fabricated by EBISA and EBID respectively, Figure 4-1c depicts a non-irradiated surface site after a FEBIP experiment, i.e. after an exposure of approximately 1.1×10^5 L of Co(CO)$_3$NO. It can be extracted that on the whole surface the formation of a thick film (i.e. substrate signals are completely attenuated in AES, Figure 4-2) with granular morphology occurs without electron irradiation. In contrast to the previous investigation of Fe(CO)$_5$ on Ag(111), no preferred grain orientation induced by the underlying anisotropic surface can be observed. Based on AES measurements the composition of the deposit was estimated with ~ 48 at. % Co, ~ 48 at. % O, and minor amounts (< 5 at. %) of N and C (Figure 4-2). Areas which were electron irradiated before (EBISA) or during (EBID)

36

precursor dosage exhibit the same morphology, however, they appear brighter in SEM (Figure 4-1a and b). Local AES shows that the corresponding FEBIP areas contain a similar cobalt/oxygen ratio of ~ 1:1, but no carbon, unlike the non-irradiated areas (Figure 4-2).
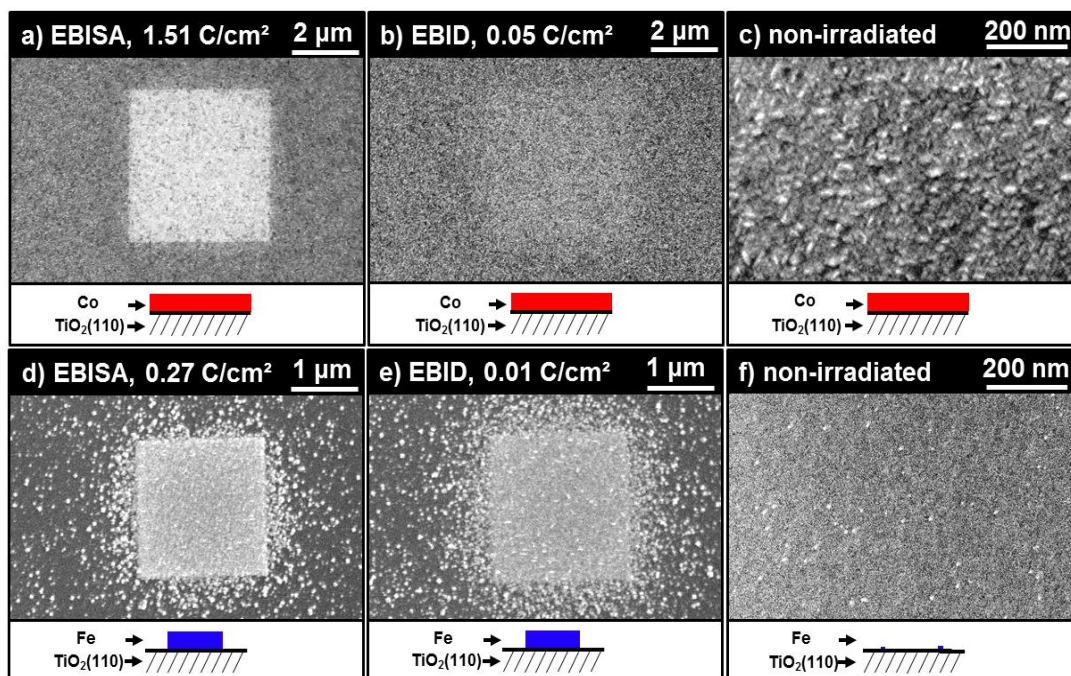

Figure 4-1: FEBIP on $TiO_2(110)$ 1×1. a) EBISA 4x4 µm² square from $Co(CO)_3NO$: a granular film has grown on the whole surface after a precursor exposure of ~1.1×10^5 L: the pre-irradiated surface area appears brighter in SEM; b) EBID 4x4 µm² square from $Co(CO)_3NO$, autocatalytic growth time t_{AG} = 217 min: lower contrast and less defined boundaries compared to EBISA areas; c) Blowup of a non-irradiated surface area after the experiment with $Co(CO)_3NO$; d), e) EBISA and EBID (t_{AG} = 128 min) 2×2 µm² square deposits from $Fe(CO)_5$: deposition and autocatalytic growth of bcc-Fe is mainly confined to irradiated areas, unselective growth is only observed at surface defects; f) blowup of a non-irradiated surface area after the experiment with $Fe(CO)_5$, again showing only scattered unselective growth of bcc-Fe.

To further investigate the peculiar role of the substrate an additional FEBIP experiment with $Co(CO)_3NO$ was performed on the 1×2 reconstructed $TiO_2(110)$. Figure 4-3a displays a scanning tunneling micrograph of the surface prior to the experiment, and Figure 4-3b depicts the corresponding LEED pattern. The reconstructed surface basically consists of bright strands oriented in the [001]-direction [75, 87, 88]. Figure 4-3c depicts the result of a
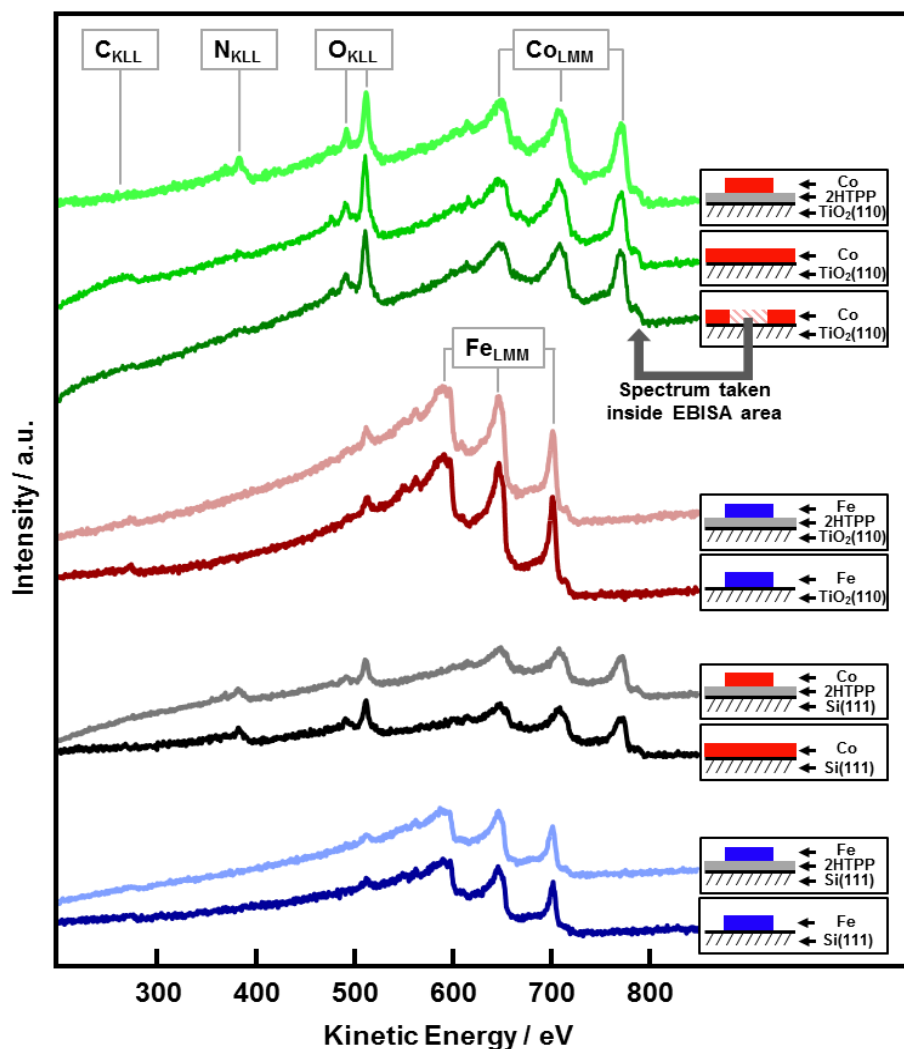
Figure 4-2: *Local AE spectra acquired from the different investigated systems, with the corresponding Auger transitions and schemes of the systems depicted. Spectra of the unselectively grown films from Co(CO)₃NO were taken at a random non-irradiated surface positions. For improved comparability by eye, all spectra were normalized (see experimental section) to account for possible deviations originating from small differences in the measurement setup.*

2×2 µm square EBID exposure with Co(CO)$_3$NO and subsequent 60 min autocatalytic growth time (~ 2.4×10^4 L Co(CO)$_3$NO). The actual deposit extends beyond the irradiated area due to proximity effects and exhibits a pronounced contrast in SEM. Local AES (Figure 4-3d, red) reveals that the deposit again consists of mostly Co and O as well as minor amounts of N and C, while AES recorded on a non-irradiated site (Figure 4-3d, blue)

38

predominantly shows substrate signals and very minor Co. This finding clearly demonstrates that a rather subtle surface modification can be sufficient to quench the catalytic activity of the latter.

FEBIP experiments with Fe(CO)$_5$ on TiO$_2$(110) 1×1 have been reported before [9], and

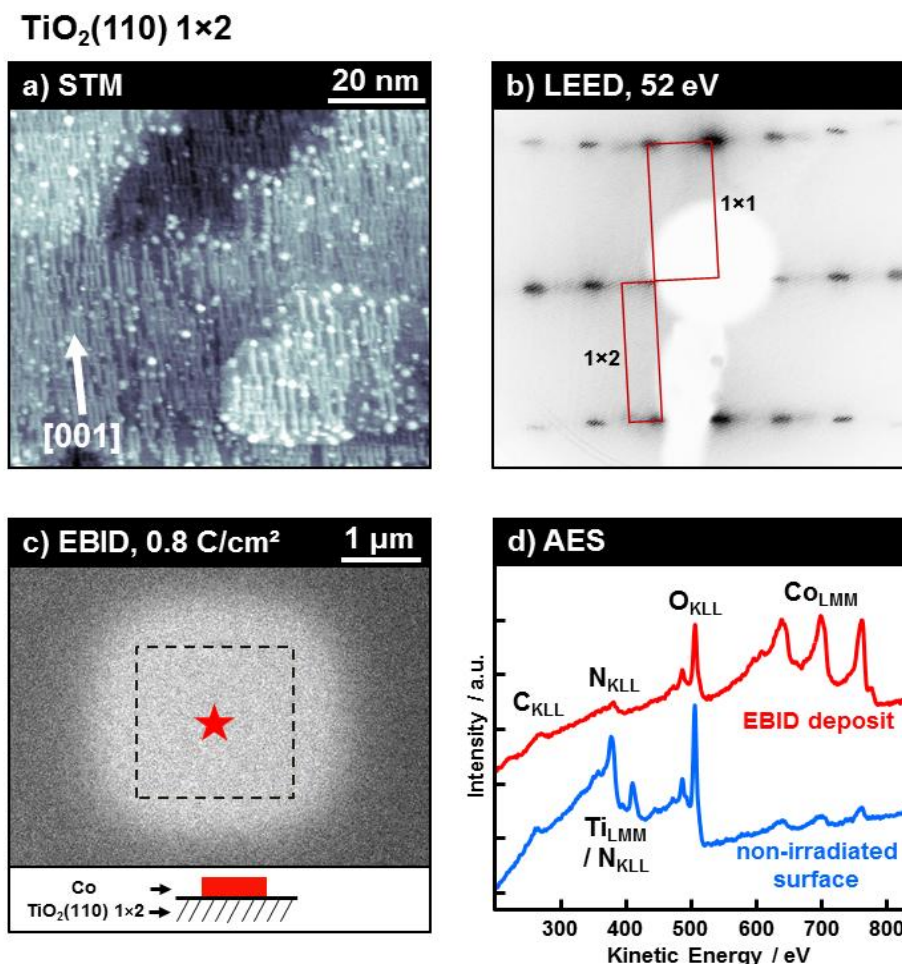***Figure 4-3***: *a) Scanning tunneling micrograph of a TiO$_2$(110) 1x2 surface that was used as a substrate for a FEBIP experiment with Co(CO)$_3$NO. The reconstructed surface appears as bright strands which are oriented in the [001]-direction (U$_{Bias}$ = 2.3 V, I = 1 nA); b) corresponding LEED pattern, recorded at 52 eV; c) EBID 2x2 µm² square deposit from Co(CO)$_3$NO, t$_{AG}$ = 60 min. Material deposition occurred outside the irradiated area (dashed frame) due to proximity effects. The red star indicates the position where local AES was conducted; d) AE spectra of the EBID deposit shown in c) (red) and a non-irradiated surface site after the exposure to Co(CO)$_3$NO.*

are briefly summarized in the following. Figure 4-1d and e depict square (2×2 µm²) deposits, fabricated by EBISA and EBID, Figure 4-1f depicts again a non-irradiated area after a FEBIP experiment, i.e. after corresponding exposure to the precursor. The non-irradiated surfaces areas appear mostly uniform, with only few scattered cubic bcc-Fe crystallites (bright spots in the depicted micrographs). The origins of this non-selective growth are local 1×2 reconstructed sites which act as nucleation centres, leading to the formation of pure bcc-Fe upon autocatalytic growth. However, the majority of the non-irradiated surface remains unchanged throughout the precursor exposure. The structures fabricated by FEBIP likewise consist of bcc-Fe crystallites formed by FEBIP and subsequent autocatalytic growth. The Fe content of these deposits was estimated by AES as ~ 95 at. % with minor carbon and oxygen contaminations. At low PE doses the crystallite formation is confined to electron beam irradiated areas, and exceeds them at higher PE doses due to proximity effects. As it has already been reported before [10], deposit formation using EBISA requires higher PE doses compared to EBID in order to obtain a similar sized deposits. This is presumably due to the different deposit formation mechanisms, i.e. modification of the substrate in EBISA and direct precursor dissociation in EBID.

From these findings the following is concluded: At RT, $TiO_2(110)$ 1×1 is catalytically active towards the decomposition of $Co(CO)_3NO$. The resulting overlayer formation is not self-limiting, i.e. catalytic activity is retained, leading to the formation of a thick granular film, remarkably consisting of approximately equal parts of cobalt and oxygen, as well as very minor amounts of carbon and nitrogen. The film deposition is not completely unselective: electron irradiation prior or during precursor exposure leads to less carbon being incorporated, presumably as a result of different dissociation pathways at pristine and irradiated surface sites. The different dissociation pathways may result in different growth rates and consequently a thicker film at pre-irradiated sites, and the observed SEM contrast can then be explained by chemical and topographical differences. However, areas where EBID was conducted exhibit a less pronounced SEM contrast compared to EBISA areas, even at relatively high PE doses (not shown). The reason for this observation remains speculative based on the available data and might be related to the different precursor dissociation mechanisms in EBISA and EBID. In contrast to the findings with the Co precursor, FEBIP with $Fe(CO)_5$ on $TiO_2(110)$ 1×1 is highly selective. Deposit formation occurs almost exclusively at pre-irradiated surface sites (EBISA) following ESD of oxygen via the Knotek-Feibelman mechanism [9, 57], and at sites where EBID was performed. Interestingly, selective deposition in FEBIP can be also observed for $Co(CO)_3NO$ if the the

experiment is performed on a 1×2-reconstructed $TiO_2(110)$ surface. After an exposure ~ $2.4×10^4$ L $Co(CO)_3NO$, only traces of Co are detected on non-irradiated surface areas, probably due to remaining 1×1 surface areas, as can be seen in the scanning tunneling micrograph in Figure 4-3a. On the other hand, $Fe(CO)_5$ decomposes at 1×2 sites, and we anticipate the growth of a closed layer on a fully reconstructed 1×2 surface. The investigated systems therefore exhibit a prime example of how surface reconstructions can play an active role in the FEBIP process due to their catalytic activity, or lack of the latter, while this catalytic activity can severely differ even for chemically closely related precursors such as $Co(CO)_3NO$ and $Fe(CO)_5$.

$2HTPP/TiO_2(110)$ 1×1. As demonstrated previously, a thin layer of organic molecules, namely 2H-tetraphenylporphyrins, is suitable to act as a "protective capping", e.g. to prevent the unselective decomposition of $Fe(CO)_5$ on Ag(111) at RT. Consequently, this concept was transferred to the system $Co(CO)_3NO$ on $TiO_2(110)$ 1×1, by covering the surface with a thin layer of 2HTPP (thickness ~ 0.5 - 1.0 nm, 2-3 layer) prior to the FEBIP experiments. In a first step, STM was performed on a single layer of 2HTPP on the TiO_2. This was done to exclude a pronounced island (i.e. Volmer-Weber) growth, as the surface has to be fully covered for complete passivation (see Figure 4-4a and caption). Figure 4-5a-d depict SEM micrographs of FEBIP point deposits (i.e. the e-beam is kept stationary at one position for the indicated PE dose), using EBISA and EBID with both precursors, on $TiO_2(110)$ covered with 2HTPP. Figure 4-5e depicts the logo of the Excellence Cluster "Engineering of Advanced Materials", using EBID with $Co(CO)_3NO$, demonstrating the ability to lithographically fabricate structures with defined shape. It is obvious that FEBIP with $Co(CO)_3NO$ (Figure 4-4a, b, e) leads to deposit formation only at irradiated sites, whereas on the non-irradiated organic layer, no deposition is observed.
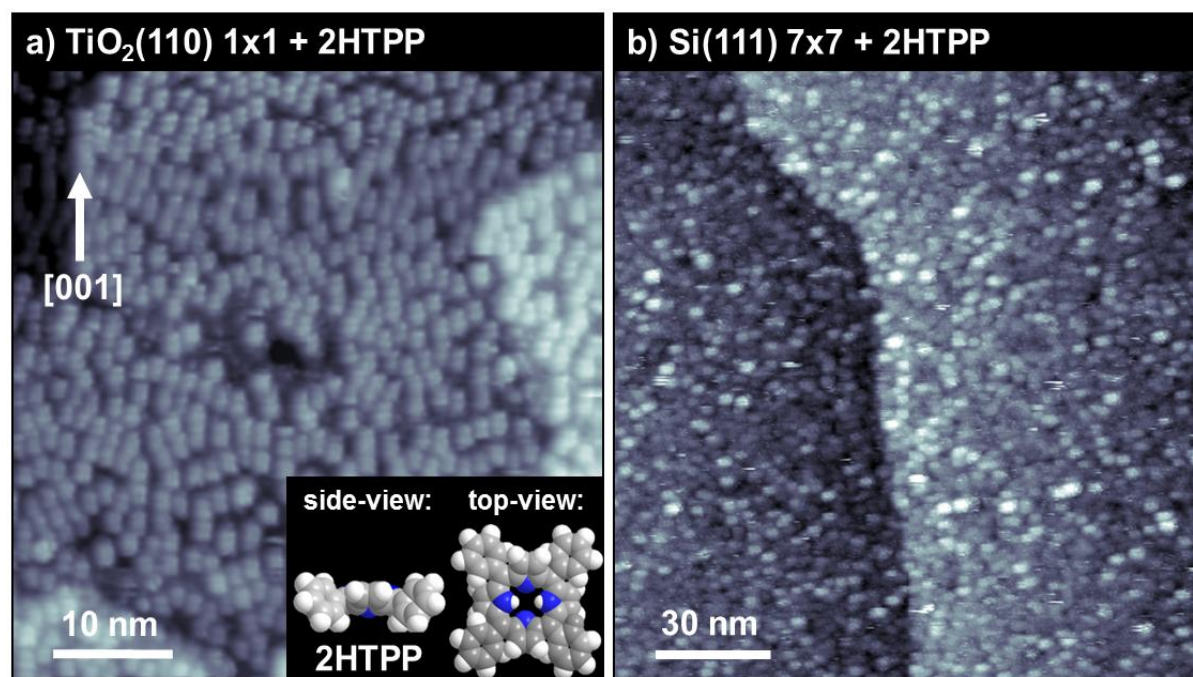
Figure 4-4: *a) Scanning tunneling micrograph of approximately one closed layer of 2H-Tetraphenylporphyrin (2HTPP) on rutile TiO$_2$(110) 1×1. Individual molecules appear as two parallel rods, perpendicular to the [001]-direction. This appearance stems from the well-known "saddle-shape" conformation of 2HTPP (see CPK model in the lower right), where the nitrogen atoms of two opposing pyrrol ring pairs either point towards the surface or away from it. The resulting intramolecular repulsive forces lead to a bending of the phenyl ring plane with respect to the surface. Some molecules agglomerate in small, ordered two-dimensional domains, and no island growth is observed; b) scanning tunneling micrograph of 2HTPP on Si(111) 7×7, with a coverage slightly above one closed layer. No intramolecular features are resolved, however, individual molecules can be distinguished as bright protrusions with a rectangular aspect ratio (note the different scale compared to a)). No long-range ordering or pronounced island growth takes place.*

All structures exhibit a granular morphology, and local AES (Figure 4-2) was used to estimate their composition to ~ 50 at. % Co, ~ 40 at. % O and ~ 10 at. % N. The deposits grow autocatalytically, resulting in an increased thickness and slightly increased lateral extension upon prolonged precursor exposure.
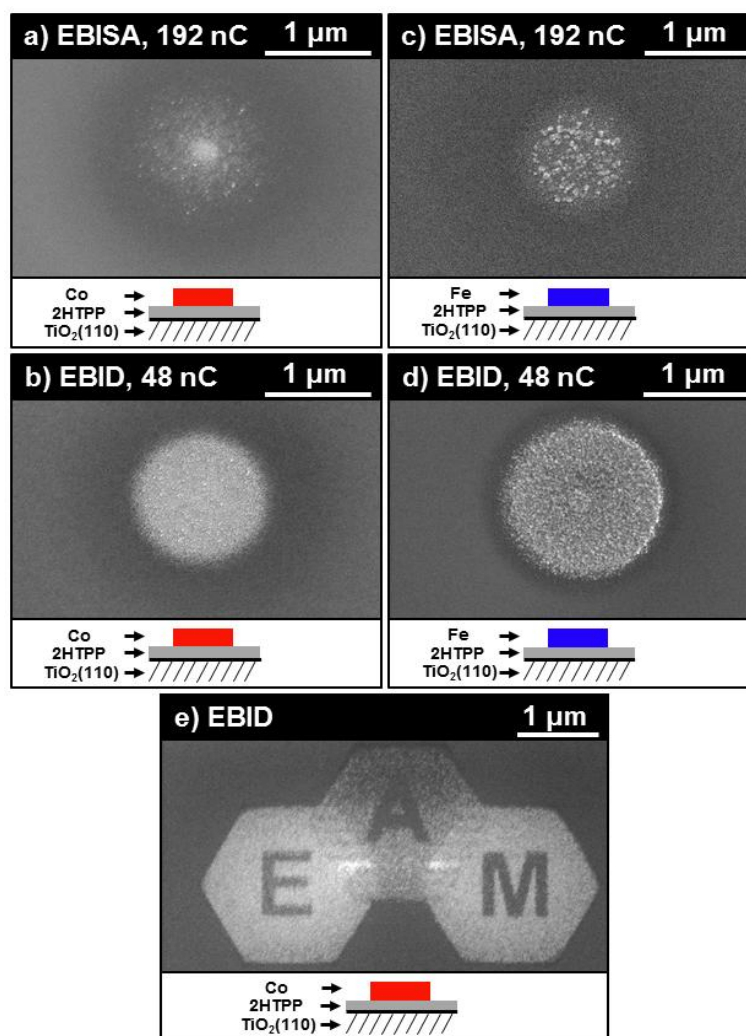
Figure 4-5: *FEBIP on 2HTPP/TiO$_2$(110) 1×1; a), b) EBISA and EBID (t$_{AG}$ = 215 min) point deposits, e) EBID area deposit (t$_{AG}$ = 144 min) from Co(CO)$_3$NO on 2HTPP/TiO$_2$(110). Non-irradiated surface areas exhibit a homogeneous SEM intensity, deposition and autocatalytic growth is confined to irradiated sites, and their surroundings due to proximity effects; c), d) EBISA and EBID (t$_{AG}$ = 255 min) deposits from Fe(CO)$_5$: as with Co(CO)$_3$NO, deposition and autocatalytic growth of bcc-Fe is confined to irradiated sites.*

Regarding the selectivity, FEBIP with Fe(CO)$_5$ shows the same results as observed before on the pristine surface, i.e. formation of crystalline bcc-Fe, again due to autocatalytic growth, is confined to sites where EBISA and EBID was performed, and the non-irradiated surface exhibits no changes. Local AES again shows an Fe content of ~ 95 at. % and only minor amounts of carbon and oxygen (Figure 4-2). Furthermore, we demonstrate that it is
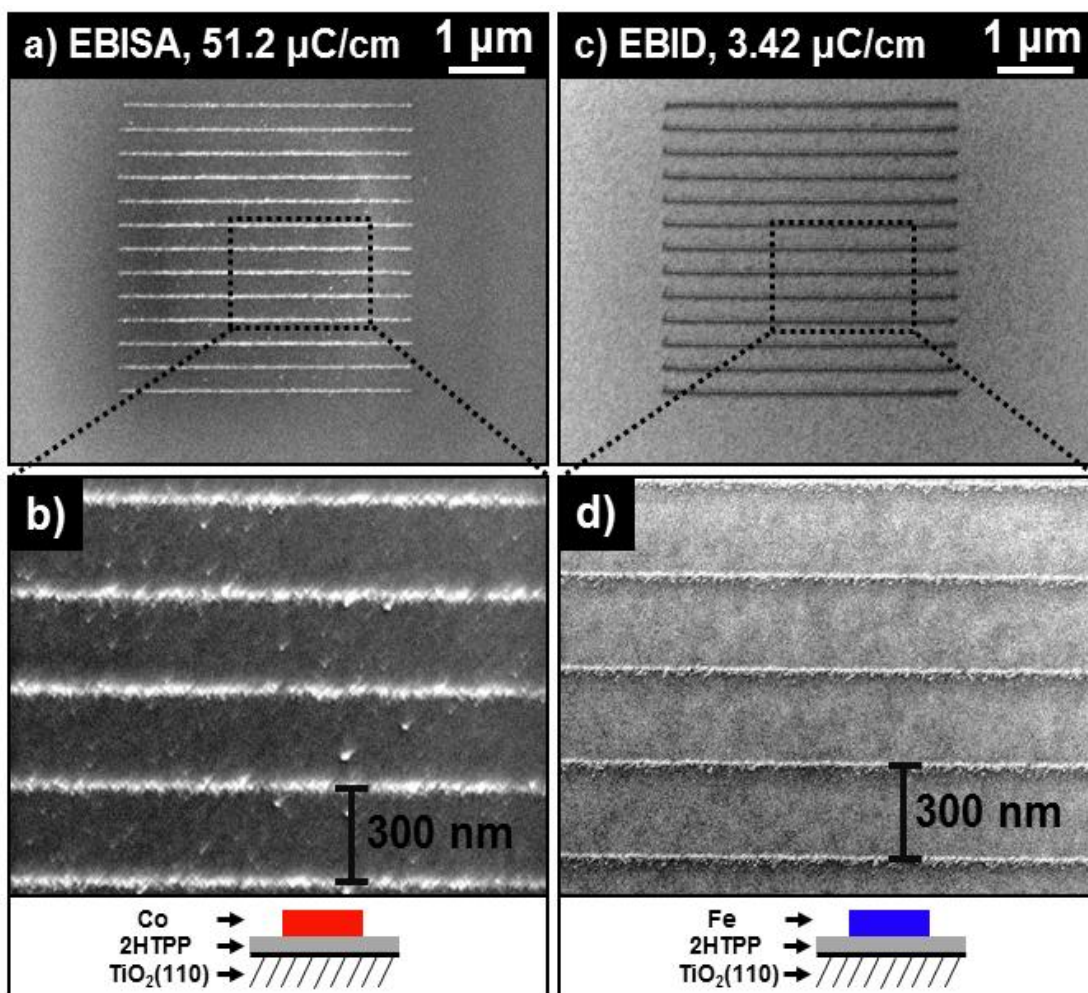
Figure 4-6: *FEBIP on 2HTPP/TiO$_2$(110) 1×1; a), b) EBISA line structures from Co(CO)$_3$NO with an average FWHM < 32 nm. Sporadically scattered deposits between the lines most likely result from proximity effects; c), d) EBID line structures (t$_{AG}$ = 34 min) from Fe(CO)$_5$ with an average FWHM < 20 nm; note the lack of crystalline bcc-Fe, due to the relatively low autocatalytic growth time compared to other FEBIP deposits shown in this work.*

possible to fabricate line deposits with an average FWHM < 32 nm (Figure 4-6a and b) using EBISA Co(CO)$_3$NO and < 20 nm (Figure 4-6c and d) using EBID with Fe(CO)$_5$. The latter were fabricated using a relatively low autocatalytic growth time of 34 min to minimize structure broadening. This results in a deposit with granular morphology, clearly distinguishable from the crystalline morphology that follows prolonged autocatalytic growth. Note that the autocatalytic growth time for the EBISA line structures from Co(CO)$_3$NO was

270 min, thus, to obtain deposits with the lateral extensions shown, a low autocatalytic growth time is not essential, but depends on the growth rate.

The concept of passivating the catalytic activity of a surface with a thin 2HTPP layer has been expanded in this chapter. From the presented results one can conclude that the organic layer effectively decouples the substrate from the FEBIP process. The catalytic activity, which in the case of $Co(CO)_3NO$ leads to the unselective decomposition and subsequent film growth at RT, is suppressed. The same applies for $Fe(CO)_5$ and its decomposition at 1×2 reconstructed sites. Instead, deposit formation is completely selective, and both EBID and EBISA protocols can be applied. It is thus demonstrated for the first time that $Co(CO)_3NO$ is a suitable precursor for EBISA on thin porphyrin layers, i.e. the substrate can be activated by the electron beam. This is especially remarkable since EBISA did not work for the cobalt precursor in previous experiments on $SiO_x/Si(100)$ and SiO_x/Si_3N_4, substrates which worked well with $Fe(CO)_5$ as precursor [69]. This aspect is interesting because it reflects a delicate chemical sensitivity of the EBISA process depending on the actual choice of one of the two precursors, which are otherwise apparently similar. Furthermore, the probed deposit sites fabricated from $Co(CO)_3NO$ contain no carbon, but a similar elemental composition compared to previous reports of FEBIP experiments with the same precursor [69, 89, 90], i.e. about 50 at. % Co and varying contents of O and N. However, it has to be noted that in the periphery of most deposits, carbon was detected (see chapter 4.1.3). One cannot conclude on the exact chemical nature of the deposits, however, a Co oxidation state higher than zero is likely, as it was reported for similar systems, e.g. for EBID and autocatalytic growth with $Co(CO)_3NO$ on Si_3N_4-membranes [69] and thermal decomposition of $Co_2(CO)_8$ on titanate nanowires [91]. The formation of carbon-free deposits from $Co(CO)_3NO$ on amorphous carbon was recently also reported in a UHV study by Rosenberg *et al.* [92]. They observe the formation of $(CO)_xOCoN$ (x = 1-2) upon 500 eV electron irradiation of an adsorbed $Co(CO)_3NO$ layer at a substrate temperature of -168 °C. Upon annealing to RT, the remaining CO and carbon desorb, resulting in a carbon free CoO_yN species. The data presented here suggests the same elemental composition, thus, no carbon is incorporated during autocatalytic growth, at least in the volume probed by AES. When comparing the AE spectra of the systems $Fe/2HTPP/TiO_2(110)$ and $Fe/TiO_2(110)$ 1×1 (Figure 4-2), minor carbon impurities of similar intensity are observed. This suggests that in FEBIP deposits from both precursors, the carbon concentration is independent of the underlying 2HTPP layer. Despite the carbon-rich environment with the 2HTPP layer, no additional carbon is incorporated during the autocatalytic growth process.

At this point the possible electron beam activation mechanisms of the 2HTPP layer will be briefly discussed. To the authors knowledge, no detailed studies concerning the chemical modifications of thin porphyrin layers on surfaces upon electron beam irradiation have been conducted so far. With the available data one cannot fully conclude on the chemical nature of the electron beam activation of the 2HTPP layer and the following precursor dissociation. However, some conclusions might be drawn from studies concerning electron beam irradiation of a variety of other organic compounds, mostly with a focus on low energy electrons. Amongst others, the observed dissociation pathways include C-C chain scission and formation of diamond-like-carbon (DLC) in undecylenic acid and 1-decene SAMs [59], dehydrogenation and intermolecular cross-linking of aromatic groups in biphenyl thiol SAMs [93, 94] and anion desorption from hydrocarbons following dissociative electron attachment (DEA) [95]. Given the vast number of potential dissociation pathways, the effect of electron beam irradiation on a 2HTPP layer remains speculative. Possible reactions might be C-C bond scission and loss of the phenyl groups, dehyrogenation followed by C-C bond formations, accompanied by formation of reactive hydrocarbon species, such as radicals and ions.

Si(111) 7×7 and 2HTPP/Si(111). To expand the investigations to other substrates, FEBIP experiments with both precursors were performed on Si(111) 7×7 and 2HTPP/Si(111) 7×7. Figure 4-7a and b depict SEM micrographs of EBID structures (4×4 µm² squares) fabricated from $Co(CO)_3NO$ and $Fe(CO)_5$, respectively, on Si(111) 7×7. Surprisingly, the deposition and autocatalytic growth of $Co(CO)_3NO$ is unselective, similar to the observations on $TiO_2(110)$ 1×1. That means the growth of a film with granular morphology can be observed on the entire surface. Chemical analysis of the latter by AES yields ~ 51 % cobalt, ~ 34 % oxygen and ~ 15 % nitrogen, but no carbon, in contrast to the film grown on $TiO_2(110)$ 1×1. Only a weak SEM contrast difference between areas where EBID was conducted and non-irradiated surface is observed (not shown), and both exhibit the same elemental composition.

In contrast, EBID with Fe(CO)$_5$ on Si(111) 7×7 is selective: deposition and growth of crystalline bcc-Fe (Fe content ~ 95 %) is only observed at irradiated sites, and partially their surroundings due to proximity effects. It has to be noted that with both precursors, EBISA is not possible on pristine Si(111) 7×7. For Fe(CO)$_5$ this is obviously again due to the lack of a
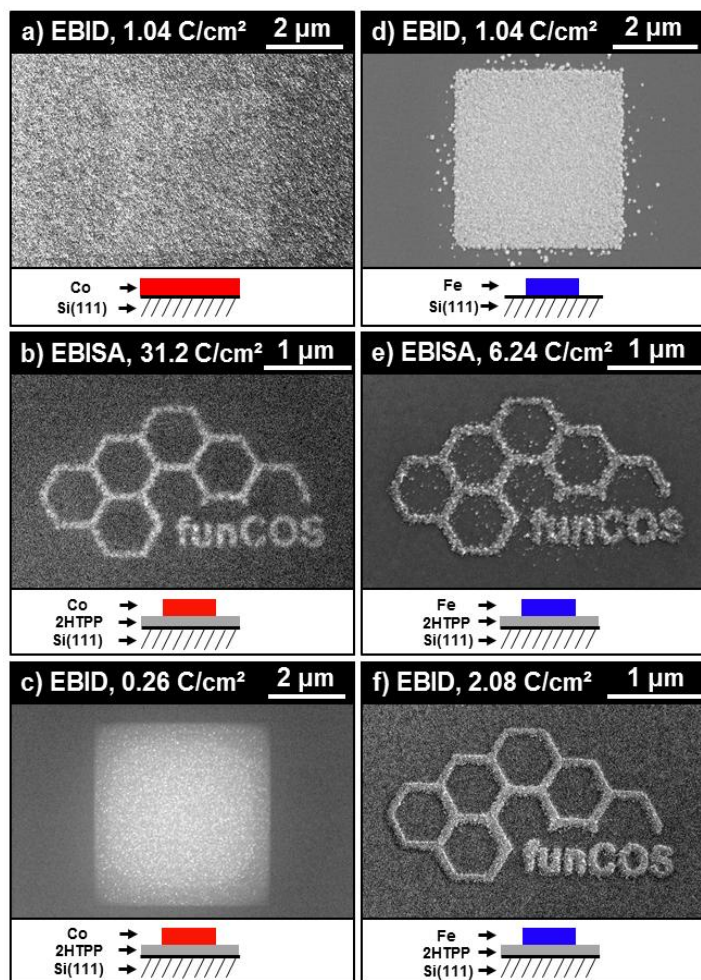

Figure 4-7: FEBIP on Si(111) 7×7 and 2HTPP/ Si(111) 7×7. a) EBID 4x4 µm² square (t$_{AG}$ = 246 min) from Co(CO)$_3$NO on pristine Si(111) 7×7. Just as on TiO$_2$(110) 1x1, growth of a granular film is observed on the entire surface. Areas where FEBIP was performed exhibit the same morphology, with only a minor SEM brightness difference. b), c) EBISA and EBID (t$_{AG}$ = 256 min) deposits from Co(CO)$_3$NO on 2HTPP/Si(111) 7×7: deposition and autocatalytic growth is confined to irradiated areas. d) EBID 4x4 µm² square (t$_{AG}$ = 252 min) from Fe(CO)$_5$ on pristine Si(111) 7×7; e), f) EBISA and EBID (t$_{AG}$ = 256 min) deposits from Fe(CO)$_5$ on 2HTPP/Si(111) 7×7: on both substrates, deposition and autocatalytic growth of bcc-Fe is confined to irradiated areas.

suitable activation mechanism, i.e. e-beam irradiation does not lead to the formation of catalytically active surface sites. At the same time, $Co(CO)_3NO$ is immediately decomposed on Si(111) 7×7 at RT, which results in the observed unselective decomposition on the whole surface. Next, STM measurements ensured the formation of a closed layer of 2HTPP on Si(111) 7×7 (Figure 4-4b in the SI). FEBIP experiments with both precursors were then performed on a 0.5 - 1.0 nm thick layer of 2HTPP on Si(111). The results are summarized in Figure 4-7b, c, e and f, which depict selected SE micrographs, including the logo of the research unit FOR 1878 "funCOS" and a 4×4 µm² square deposit. In analogy to the system 2HTPP/TiO_2(110), deposition is now confined to surface areas where FEBIP was conducted. Both EBISA and EBID protocols are successful, and autocatalytic growth at RT is observed. Local AES shows deposits from $Co(CO)_3NO$ consist of ~ 61 % cobalt, ~ 34 % oxygen and ~ 12 % nitrogen, while deposits from $Fe(CO)_5$ again consist of > 95 % iron and minor oxygen and carbon contributions.

It is concluded that the delicate chemical sensitivity of the precursors and the concept of surface passivation with 2HTPP can be expanded to the Si(111) 7×7 surface and appears to be of general character. Like on TiO_2(110) 1×1, the catalytic activity of the pristine surface towards the decomposition of $Co(CO)_3NO$ is suppressed by the thin organic layer, enabling the fabrication of nanostructures with high spatial selectivity. Unlike the pristine Si(111) 7×7, the 2HTPP layer is suitable for EBISA with $Co(CO)_3NO$ and $Fe(CO)_5$. This enables interesting nanofabrication strategies: all substrates that lack a suitable e-beam activation mechanism can be used for EBISA by covering it with a thin layer of 2HTPP, or another suitable compound. A requirement for this would be a sufficiently flat and clean pristine surface, such that the organic layer is completely closed and, ideally, grows in a layer-by-layer fashion. Due to the tendency to adsorb in a nearly flat lying fashion [96], porphyrin derivatives generally appear to be good candidates for this approach.
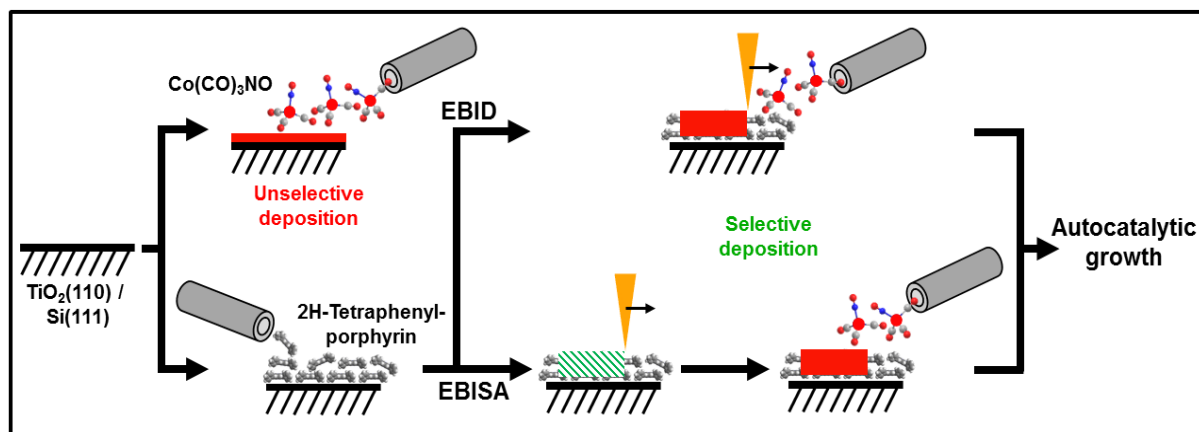
Figure 4-8: *Scheme of the concept of surface passivation with 2HTPP. Upon dosing of Co(CO)$_3$NO on either rutile TiO$_2$(110) 1×1 or Si(111) 7×7, unselective precursor decomposition and film growth takes place. By covering the pristine surface with a thin layer of 2HTPP, the catalytic activity of the surface is suppressed. Instead, nanostructures can be fabricated with high site selectivity, using either of the EBID or EBISA routines and subsequent autocatalytic growth. The depicted procedure of FEBIP on 2HTPP covered substrates also works with Fe(CO)$_5$.*

Figure 4-8 illustrates the concept that was demonstrated in this chapter. At RT, the pristine surfaces of rutile TiO$_2$(110) 1×1 and Si(111) 7×7 are catalytically active towards the decomposition of the precursor Co(CO)$_3$NO, resulting in an unselective deposition and subsequent film growth at surface sites where no FEBIP was performed. Interestingly it was found that on TiO$_2$(110) 1×2, the situation is significantly different: no unselective deposition was observed with Co(CO)$_3$NO, except on remaining 1×1 areas. In contrast, FEBIP with Fe(CO)$_5$ on TiO$_2$(110) 1×1 and Si(111) 7×7 is spatially selective. This is especially remarkable, since one anticipates similar reactivities for the apparently similar precursors. However, it appears that the sensitivity towards the corresponding surface sites is delicate. In that perspective, more efforts have to be made to understand the reactivity of such compounds on a fundamental level. One might envision to design precursor molecules for the selective decomposition at specific surface sites, which would open up new pathways for the controlled fabrication of well-defined nanostructures. The decomposition of Co(CO)$_3$NO can be prevented by pre-covering the surface with a thin layer (~ 0.5 - 1.0 nm) of 2HTPP. This organic layer is a suitable substrate for highly site selective deposition and autocatalytic growth with both precursors, either using the EBID or the EBISA protocol. Local AES of

these deposits indicates that despite the carbon-rich surface layer, no carbon incorporation during autocatalytic growth occurs. Line structures on 2HTPP/TiO$_2$(110) with an average FWHM < 32 nm (EBISA with Co(CO)$_3$NO) and < 20 nm (EBID with Fe(CO)$_5$) were fabricated, demonstrating that it is possible to fabricate nanoscale structures in a controlled manner on this surface. These results expand the applicability of EBISA, by showing for the first time that Co(CO)$_3$NO is a suitable precursor for the method, in addition to the precursors Fe(CO)$_5$ and Co$_2$(CO)$_8$ that have already been shown to work [7, 58]. Even a substrate that lacks a suitable e-beam activation mechanism, i.e. Si(111) 7×7, can be used for EBISA by pre-covering it, e.g., with 2HTPP and activating the thin organic layer. Even though the detailed chemical mechanisms are not yet fully understood, it is clear that the present findings significantly expand the scope of FEBIP and open several novel pathways for controlled nanofabrication. For example one might envision to use the thin organic layer in only for passivation or "enabling" EBISA, and then thermally desorb it after the FEBIP step. A requirement for this would be sufficiently low desorption temperature in order to prevent thermal decomposition of the FEBIP deposits. Another idea is to use molecular architectures, e.g. from porphyrins that form supramolecular well-ordered structures with regular pores in the single digit nanometer-regime [97, 98]. At the pores the surface is consequently exposed and thus potentially active towards the corrresponding decomposition of precursor molecules. In this way, regular pattern of catalytically deposited material might be realized with dimensions well below the usual structures fabricated via FEBIP protocols.

4.1.3 Binary composition on 2HTPP-covered rutile TiO$_2$(110) and Si(111)

In the course of investigating the FEBIP structures fabricated on 2HTPP-covered substrates, a peculiar, heterogeneous SEM brightness of the deposited material was observed (e.g. Figure 4-7c), which was the starting point for further investigations. Figure 4-9 depicts additional, selected SE micrographs of deposits fabricated by EBID and EBISA, with both Fe(CO)$_5$ and Co(CO)$_3$NO on 2HTPP-covered rutile TiO$_2$(110) and Si(111). Figure 4-9a and the corresponding blowup depict a grating structure, Figure 4-9b the logo of the Excellence Cluster "Engineering of Advanced Materials", both fabricated by EBID with Co(CO)$_3$NO on 2HTPP/TiO$_2$(110). The applied primary electron line dose in the grating structure and the primary electron area dose in the hexagons surrounding the letters E and M were constant. It can be observed that both structures exhibit a distinct contrast between
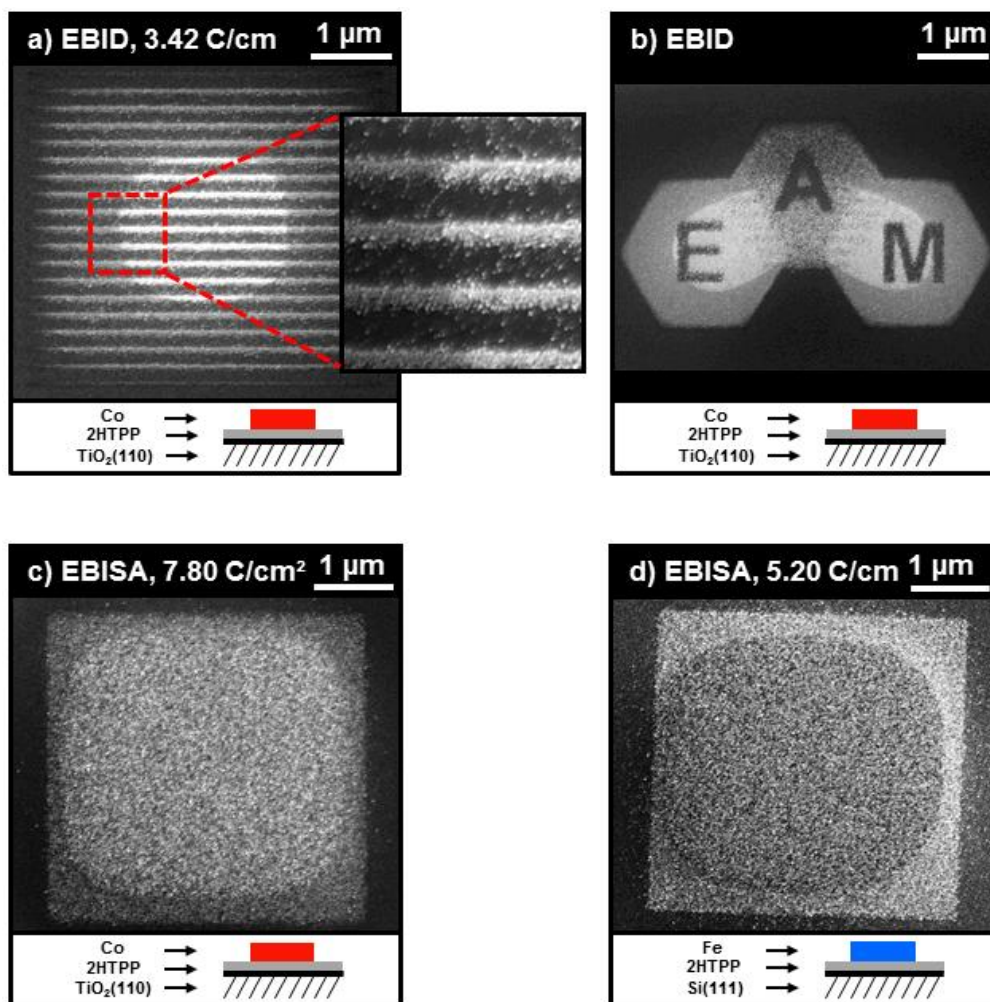
Figure 4-9: *Selected SE micrographs of FEBIP deposits fabricated on 2HTPP-covered substrates. a) EBID grating structure, Co(CO)$_3$NO on 2HTPP/TiO$_2$(110), 3.42 C/cm², t_{AG} = 222 min; b) EBID deposit, Co(CO)$_3$NO on 2HTPP/TiO$_2$(110), t_{AG} = 261 min; note that no electron area dose is given, as it varies in the different irradiated areas; c) EBISA 4×4 µm² square deposit, Co(CO)$_3$NO on 2HTPP/TiO$_2$(110), 7.80 C/cm²; d) EBISA 4×4 µm² square deposit, Fe(CO)$_5$ on 2HTPP/Si(111), 5.20 C/cm².*

the brighter interior (referred to as 'inner part') and darker peripheral areas ('outer part'), with a sharp, defined boundary where the brightness changes abruptly. This boundary is well visible in the blowup image, where it can also be seen that the material in both areas exhibits the same appearance and therefore morphology. Figure 4-9c and d depict 4×4 µm² square deposits fabricated by EBISA with Co(CO)$_3$NO on 2HTPP/TiO$_2$(110) (Figure 4-9c) and Fe(CO)$_5$ on 2HTPP/Si(111) (Figure 4-9d). Again, both structures exhibit a pronounced

contrast between interior and periphery. Unlike in the other depicted micrographs, in the case of EBISA with $Fe(CO)_5$ on 2HTPP/Si(111) the inner part appears darker than the periphery, which, however, has occasionally also been observed for the other systems, e.g. EBID with $Co(CO)_3NO$ on 2HTPP/TiO_2(110) (Figure 4-15a).

In order to obtain spectromicroscopical information concerning these areas of different brightness, local AES was conducted. Figure 4-10a depicts a series of local AE spectra recorded on the inner and outer parts of 4×4 µm² square deposits, fabricated by EBID, with $Co(CO)_3NO$ on 2HTPP/TiO_2(110), with all deposition parameters the same except for different autocatalytic growth times. The corresponding SE micrographs are depicted above, with the coloured stars indicating the position where the respectively coloured spectra were recorded. Following the signal intensities of the inner part with increasing autocatalytic growth time, one can observe an increasing Co_{LMM} signal, an almost constant O_{KLL} signal, a decreasing C_{KLL} signal and an almost vanishing Ti_{LMV} signal. In the outer part the Co_{LMM} signal increases, the O_{KLL} signal remains almost constant and the Ti_{LMV} signal vanishes as well, however all are less intense compared to the inner part. In contrast, the C_{KLL} signal is more intense after t_{AG} = 30 min and decreases only slightly, resulting in a significantly higher intensity after t_{AG} = 180 min compared to the inner part. Additionally, all spectra presumably exhibit a N_{KLL} peak that can only unambiguously be identified when the overlapping Ti_{LMM} signal (and therefore the Ti_{LMV} signal) is completely attenuated, e.g. in the outer part with t_{AG} = 188 min. Additionally, local AES was conducted on the inner part of 4×4 µm² square deposits, again fabricated with $Co(CO)_3NO$ on 2HTPP/TiO_2(110), with all deposition parameters the same (t_{AG} = 164-166 min) except for different primary electron doses (Figure 4-10b). With increasing electron dose one can observe an increasing Co_{LMM} signal, an almost constant O_{KLL} signal and vanishing C_{KLL} and Ti_{LMV} signals. Again the N_{KLL} signal can be unambiguously assigned as the overlapping Ti signals becomes completely attenuated. Therefore the inner part of the deposit fabricated with the highest electron dose (0.41 C/cm²) consists of cobalt, oxygen and nitrogen whereas the outer part exhibits significant amounts of carbon (corresponding spectrum not shown). The same observations regarding the carbon content of inner part and periphery of the deposits were made for any combination of aforementioned precursors and 2HTPP-covered substrates, using either EBID or EBISA.
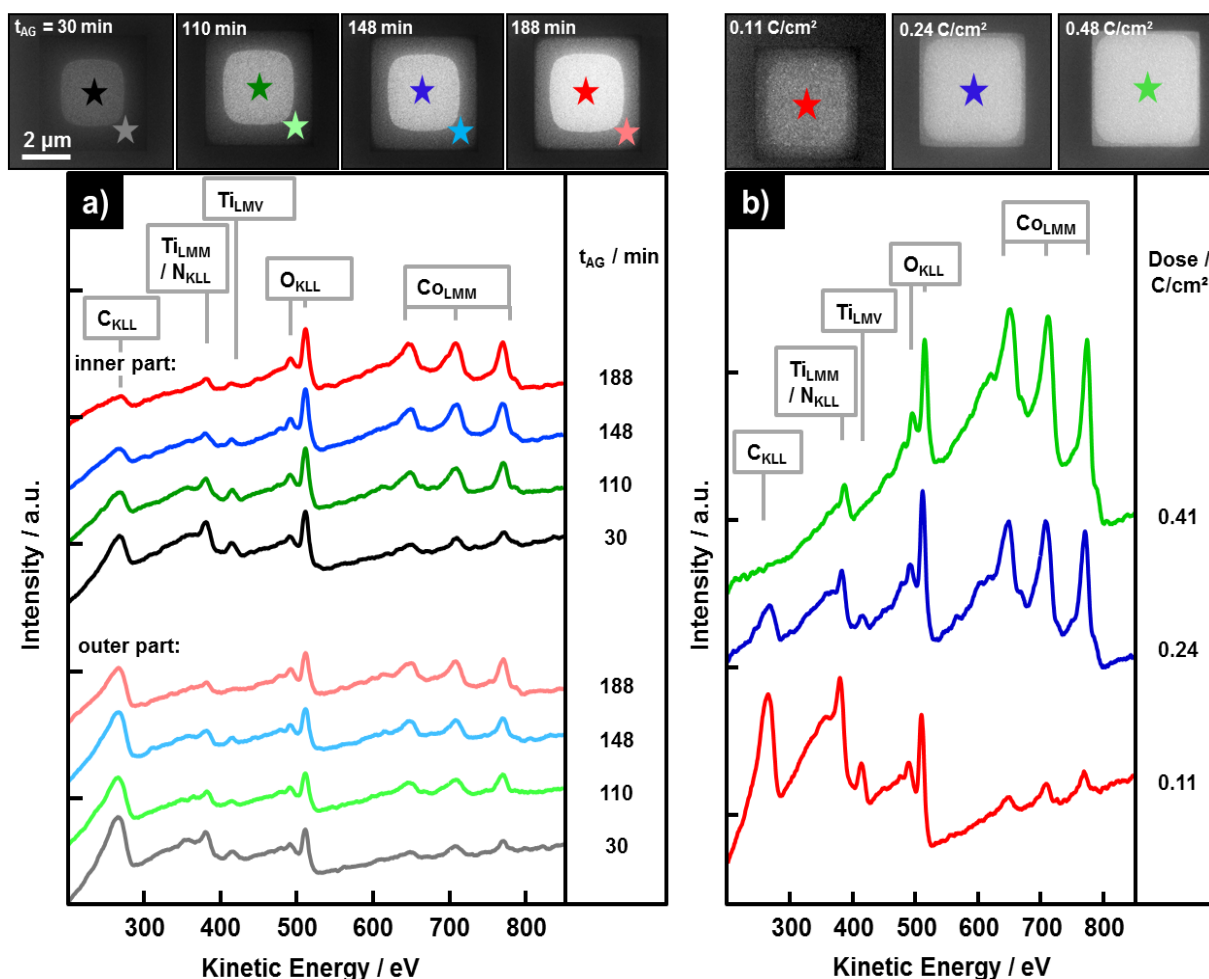
Figure 4-10: *Series of AE spectra recorded on 4×4 µm² square deposits fabricated by EBID with Co(CO)₃NO on 2HTPP/TiO₂(110), with the positions indicated by respectively coloured stars in the SE micrographs above. a) Spectra recorded on the inner and outer parts of deposits fabricated with different t$_{AG}$, highlighting the different carbon contents in the two parts; b) spectra recorded on the inner part of deposits fabricated with different primary electron doses, showing that this part of the structure contains no carbon.*

The following can be concluded from these findings. Deposits fabricated with EBID and EBISA, with both Fe(CO)₅ and Co(CO)₃NO on 2HTPP-covered rutile TiO₂(110) and Si(111) exhibit a pronounced SEM contrast between the inner part and periphery of the structure. This contrast is only observed on 2-dimensional deposits, i.e. not on point deposits as depicted in Figure 4-5. The extent of the inner part increases with increasing primary electron dose (Figure 4-10b), therefore it is assumed that the formation of the inner part

requires a critical total electron dose (including secondary and backscattered electrons), which is not reached when irradiating a single pixel in the point deposit. The contrast was observed using EBID or EBISA, with both precursors, on all investigated substrates covered with 2HTPP, and since it was never observed on a pristine substrate, its formation is consequently ascribed to the presence of the 2HTPP layer in the FEBIP process. Previous FEBIP experiments with $Fe(CO)_5$ on 2HTPP/Ag(111) only included 0- (point) and 1-dimensional (singular line) deposits [10], which is regarded as the reason why the contrast was not observed in this system.

Local AES reveals that the inner part does not contain carbon, which is apparent from the spectrum of the structure fabricated with the highest electron dose in Figure 4-10b. In the spectra of the deposits fabricated with lower electron dose, the substrate Ti signals are not completely attenuated, and the carbon signal observed here is therefore ascribed to the 2HTPP layer that is presumably still present between the deposit and the TiO_2 substrate. In contrast, the periphery contains significant amounts of carbon. This is evident when comparing the two spectra of the deposits fabricated with t_{AG} = 188 min in Figure 4-10a. The inner part is not thick enough to completely attenuate the substrate Ti signals, and the observed C_{KLL} signal is consequently again ascribed to the 2HTPP layer between deposit and substrate. The outer part exhibits even less intense Ti signals, therefore one would also expect a less intense C_{KLL} signal if it originates from the underlying 2HTPP layer as well. However, it is significantly more intense and is therefore assumed to originate from the deposited material. It is in principle possible that this intense C_{KLL} signal is caused by the 2HTPP layer next to the deposit, due to the close proximity of the measurement position to the deposit edge and thus contribution of BSEs and SEs escaping the substrate outside of the deposit to the formation of C_{KLL} Auger electrons. However, this is ruled out, as one would then expect to observe Ti signals as well. The deposits thus exhibit a binary composition, i.e. with and without carbon, and both areas with approximately the same ratio of Co, O and N, or Fe in case of deposits fabricated from $Fe(CO)_5$. However, the SEM brightness difference cannot solely be ascribed to a chemical contrast, i.e. a brighter appearance due to a smaller carbon content and thus higher mean atomic number, as the reversed contrast (darker interior and brighter periphery) has been observed on several occasions. Despite the high carbon content, autocatalytic growth of the outer part was observed in all systems. In the case of deposits from $Fe(CO)_5$ on 2HTPP-covered substrates, the catalytically active, crystalline Fe cubes were observed in the outer part as well. As the incorporation of such significant amounts of carbon atoms into the Fe crystal lattice is can be regarded as very

unlikely, the deposit might consist of Fe crystals embedded in a carbonaceous matrix, or a mixture of crystalline Fe and Fe_xC_y. In the case of $Co(CO)_3NO$ the deposit chemistry following autocatalytic growth is not well understood, therefore predictions concerning the incorporation of carbon would be of too speculative nature. It also has to be emphasized that the point deposits are carbon-free (spectra not shown), therefore their composition corresponds to the inner part of area deposits. Considering that most of the deposition in point deposits is caused by BSEs and SEs, with a lower total dose than in the carbon-rich periphery of area deposits (where neighbouring pixels lead to pronounced proximity effects), it is speculated that a complex interplay of PEs, BSEs and SEs leads to the incorporation of carbon.

Next, a series of experiments was performed in order to obtain information concerning the formation of the different areas. As the effect was observed for both EBID and EBISA, a first assumption is that electron-precursor interactions are not decisive. The extent of the inner part was found to increase with increasing primary electron dose (SE micrographs in Figure 4-10b), therefore proximity effects that might lead to, e.g., different 2HTPP dissociation pathways at sites with high BSE emission density are first considered. A possible scenario would be a critical BSE dose that is be required to activate the 2HTPP layer such that no carbon incorporation in the deposit occurs, e.g. due to complete decarbonylation of the precursor in the inner part and only partial decarbonylation in the outer part.

In order to do so, the BSE emission density, derived from Monte Carlo (MC) simulations calculated with the Penelope code, at the boundary between inner and outer part in EBISA deposits fabricated with different electron doses, with $Co(CO)_3NO$ on $2HTPP/TiO_2(110)$, is evaluated (Figure 4-11). EBISA was chosen because FSEs, which are not calculated by the MC simulations, do not contribute to the deposit formation. By means of a python script, the
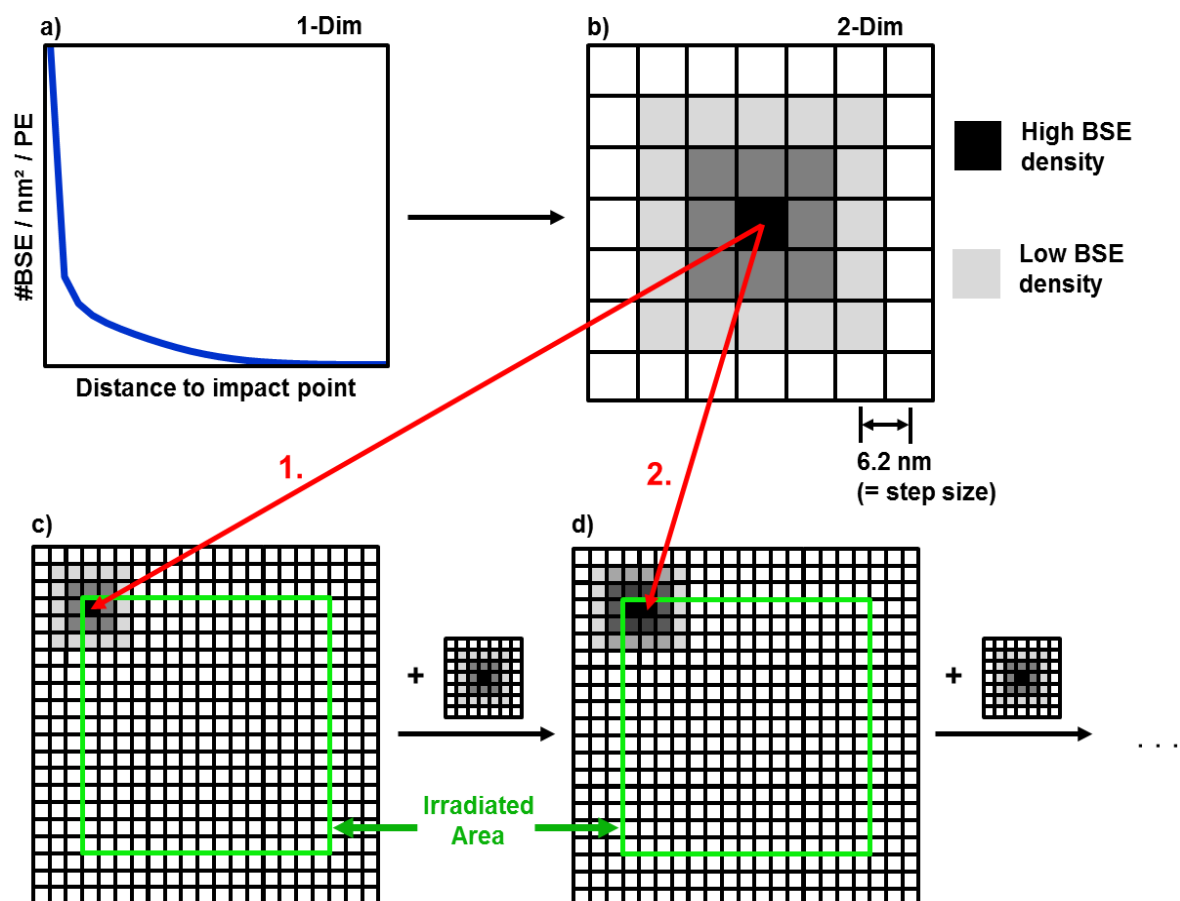

Figure 4-11: *Scheme of calculating the BSE density when irradiating a square pattern, based on a) a one-dimensional dataset (BSE density as a function of the distance to the beam impact point) obtained by MC simulations; b) scheme of a matrix calculated from the one-dimensional dataset, resulting in a two-dimensional gaussian distribution; c) the matrix obtained in b) is added into a zero matrix, representing the irradiation of one pixel in a square pattern; d) the next irradiation step is calculated by adding the matrix b) to matrix c), with the center point of b) moving to the next element, representing one step size in the experiment. This is continued until the complete irradiated area (matrix) is calculated.*

simulations were conducted by first calculating the BSE emission density matrix of a single point irradiation, based on a 1-dimensional dataset (i.e., BSE emission density as a function of distance to the impact point, Figure 4-11a) obtained with Penelope (Figure 4-11b). The experimentally obtained square patterns are formed by irradiating a point matrix with a fixed step size of 6.2 nm between each point. Therefore the BSE emission density of the irradiated pattern is obtained by adding up the single point irradiation matrices into a zero matrix (Figure 4-11c), with the center point shifting by one pixel, corresponding to the step size of 6.2 nm, between each addition (Figure 4-11d), until the complete irradiated square/matrix is calculated. In Figure 4-12a, two series of SE micrographs of 4×4 µm² square deposits with three different primary electron doses, fabricated by EBISA in two separate experiments, are depicted. Again, a contrast between the inner and outer part is observed, with the extent of the inner part increasing with increasing electron dose. Below, the corresponding simulated BSE emission densities of the square patterns, scaled to the three primary electron doses, are depicted. In Figure 4-12b, line profiles over the simulated squares, with their positions indicated in the images, are depicted. The BSE emission extends the irradiated area, and increases when approaching the central part until an extended saturation area is reached. Additionally, the position of the boundary between the carbon-rich and carbon-free areas of the respective EBISA deposits is indicated; as the extent of the inner part slightly deviated in both experiments, the arithmetic mean is used.
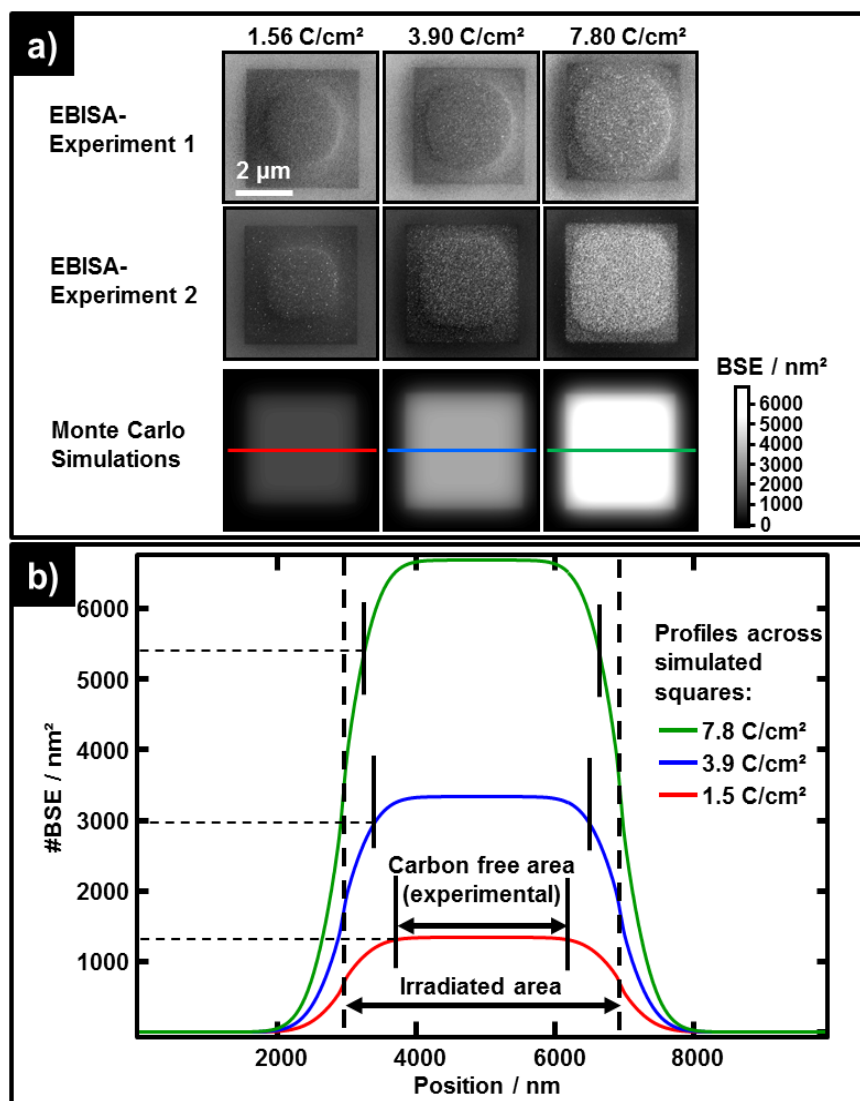
Figure 4-12: a) SE micrographs of 4×4 µm² square deposits fabricated by EBID with Co(CO)₃NO on 2HTPP/TiO₂(110) (two experiments), and the corresponding Monte Carlo simulations (see text for detailed description); b) line profiles over the simulated squares, as indicated in the respective colour. The extent of the experimentally obtained carbon free area for the three primary electron doses is indicated, showing a pronounced difference in BSE density at the boundaries.

It is clearly visible that the BSE emission densities at the boundaries are different, with a factor of almost 5 between the structures fabricated with 1.5 C/cm² and 7.8 C/cm². This indicates that there is no constant, critical BSE density to form carbon-free areas. However,

one has to consider that the calculated BSE density includes electrons of all energies from 50 eV to 15000 eV (primary beam energy), which likely have varying cross sections to induce the corresponding reactions. A different energy distribution and thus different average cross sections at the boundaries might then explain the varying amounts of electrons required to obtain the carbon-free material. A further explanation might be a different distribution of low-energy electrons with $E_{Kin} < 50$ eV, which have the highest cross sections for variety of reactions [53] and are not considered in the simulations.

To further explore the observed phenomenon, another EBID experiment was performed with $Co(CO)_3NO$ on $2HTPP/TiO_2(110)$, with the corresponding SE micrographs depicted in Figure 4-13. A series of circular deposits with varying primary electron dose and deposit radius was fabricated, with two deposits for each dose and radius: one with the complete circular area irradiated ('circular deposit'), another one with the inner part left non-irradiated, i.e. a ring structure ('ring deposit'). The corresponding SE micrographs were cut (dashed red line) such that only half of the structure is visible, allowing for a direct comparison of the appearance of the two structures that were fabricated with identical electron area dose and radius by placing the complementary halves of a circular and a ring deposit next to each other. The boundaries of the irradiated areas are indicated with turquoise lines in the lower half of each image. Note that for an electron dose of 1.184 C/cm² with 2959 nm and 4030 nm deposit radii, no irradiation of a full circle was conducted due to time reasons. Again, the formation of the two areas of different brightness is observed in the circular deposits, with the radius of the inner part increasing with increasing electron dose. Most ring deposits exhibit the contrast as well, and the radius is always the same as in the corresponding circular deposits. This is surprising, as the effective electron dose (including BSE and SE) in the ring structures is lower because the inner part is not irradiated. As indicated with the orange arrows, the ring structures exhibit no brighter area if the brighter area of the corresponding circular structure does not extent into the irradiated area of the ring structure. As indicated with the green arrow, the ring structure fabricated with a radius of 2015 nm and an electron dose of 1.184 C/cm² is extended over its irradiated area due to proximity effects. The bright part only extends into this non-irradiated area, again corresponding to the radius of the fully irradiated circular structure.

It can therefore be concluded that the extent of the inner part does not solely depend on the electron dose, even though its extent increases with increasing electron area dose. This is clearly the case in the deposits fabricated with electron area doses of 0.237 and 0.592
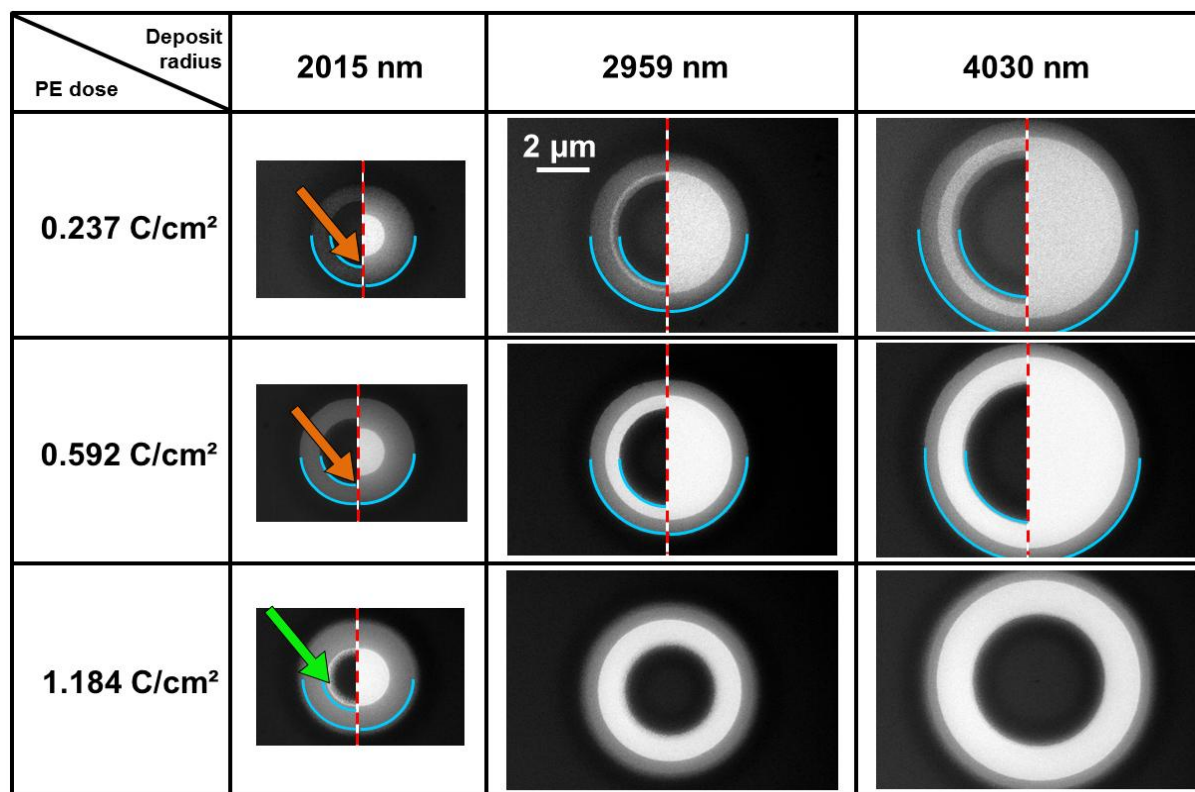
Figure 4-13: *SE micrographs of circular (complete area irradiated) and ring-shaped (central part not irradiated) EBID deposits fabricated with Co(CO)$_3$NO on 2HTPP/TiO$_2$(110) with different radii and electron area doses. Micrographs of circular and ring-shaped deposits fabricated with the same parameters are cut in half and the complementary halves placed next to each other, except for deposits fabricated with an electron dose of 1.184 C/cm² and radii of 2959 and 4030 nm.*

C/cm² and radii of 2959 and 4030 nm, where the effective electron dose (including BSE and SE) on the boundary between inner and outer part in the ring deposit is lower compared to the boundary of the circular deposit, as there is no contribution from irradiating the inner area. It can further be stated that primary electrons do not contribute to the formation of the inner part: in the ring deposit fabricated with a radius of 2015 nm and an electron dose of 1.184 C/cm² (green arrow), the inner part only extends on material that was deposited due to proximity effects, with a distance of ~ 100 nm away from the irradiated area. At this distance away from the impact point of the electron beam, the density of electrons that still have the primary beam energy is negligible due to the limited inelastic mean free path, which suggests that only certain interaction products of the primary electrons lead to the

formation of the inner part. One might speculate that, under the assumption that the cross section of the corresponding electron-induced reaction for electrons in the keV-regime is negligible compared to low energy electrons, only secondary electrons yield the formation of the carbon-free area. This might explain the aforementioned different amounts of BSEs needed to obtain the carbon-free area, which were acquired from simulations that neglect electrons with $E_{Kin} < 50$ eV. However, the reason why the radius of the inner part is the same in ring deposits as in fully irradiated circles, despite a lower total electron dose at the boundary, is still unclear.

An EBID experiment was then conducted to find out if diffusion of 2HTPP during the deposition process also influences the extent of the two areas. It is well established that in the case of a precursor diffusion limited deposition rate, which is the case in the UHV experiments conducted in this work, the deposition yield is increased when a deposit is fabricated by increasing the number of sweeps (i.e. the number of scan iterations, also referred to as loops), and reducing the dwell time at each point by the same factor to keep

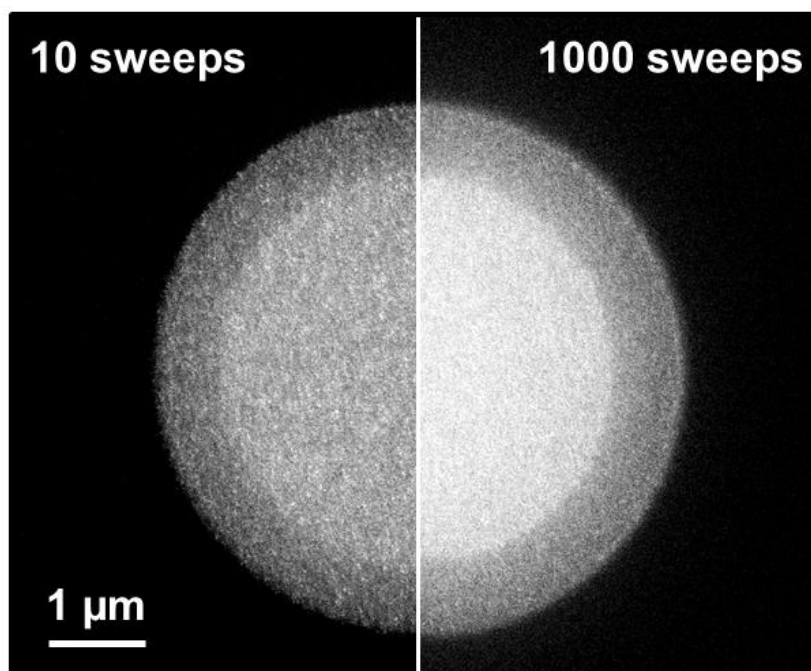**Figure 4-14:** *SE micrographs, cut in half, of a circular deposits fabricated with Co(CO)₃NO on 2HTPP/Si(111) with 10 (left half) and 1000 sweeps (right half), for a total electron dose of 0.66 C/cm². t_{AG} (left) = 263 min, t_{AG} (right) = 136 min.*

the total primary electron dose constant [6]. This is due to the so-called replenishment effect: when the beam dwells at a certain point, the deposition rate decreases over time as the surface-adsorbed precursor molecules become depleted. During irradiation of the rest of the structure, precursor molecules can diffuse or adsorb to this point, resulting again in an increased precursor concentration and thus deposition rate at the next sweep. Based on this principle, the idea for this experiment was that during electron beam irradiation, 2HTPP molecules might diffuse into the irradiated area, leading to decomposition and thus an increased carbon concentration at the periphery. By varying the number of sweeps, the 2HTPP concentration and deposition rate at the periphery and therefore the extent of both areas might be controlled.

In Figure 4-14, a deposit fabricated by EBID with $Co(CO)_3NO$ on 2HTPP/Si(111) is depicted. Two circular deposits with identical primary electron dose and radius, but different amounts of sweeps (10 and 1000) were fabricated. For improved comparability, the deposit micrographs were again cut and the complementary halves placed next to each other. The structure fabricated with 1000 sweeps appears more homogeneous and brighter, which is ascribed to an increased amount of deposited material due to the replenishment effect. It can clearly be seen that the extent of the inner part in both structures is nearly the same, the only difference is that the boundary in the structure written with less sweeps is less defined, probably due to the generally granular nature of the deposit. One can therefore conclude that, at least with the processing parameters used here, the extent of both parts is not influenced by a replenishment effect.

In conclusion, it was observed that deposits fabricated with $Co(CO)_3NO$ or $Fe(CO)_5$, with either EBID or EBISA, on 2HTPP-covered $TiO_2(110)$ and Si(111) exhibit a pronounced SEM contrast between inner part and periphery of the structure. At the boundary of these two areas, the change in brightness occurs abruptly, and local AES reveals that while the outer part contains significant amounts of carbon, the inner part does not. The extent of the inner part has been found to increase with increasing primary electron dose, suggesting that above a critical electron dose, the 2HTPP layer (as the effect was also observed in EBISA and never on a pristine substrate) is chemically modified such that no carbon incorporation in the deposit above takes place. One possibility might be the formation of a particularly reactive species that leads to a complete precursor decarbonylation, in contrast to only partial decarbonylation at the periphery where the electron dose is lower. However, further experiments and simulations suggest that the electron dose is not the only factor

determining the extent of the inner part. On the one hand, the simulated BSE density at the boundary was evaluated for three square deposits fabricated with different electron doses, showing a difference by up to a factor of ~ 5. A further experiment revealed that the radius of the inner part in a fully irradiated, circular deposit is the same as in a circular deposit where the inner area was left non-irradiated, despite different (secondary and backscattered) electron doses at the respective boundaries. In order to investigate a possible influence of diffusion of 2HTPP, circular deposits were fabricated with different amounts of sweeps, but no difference in the radii of the inner parts was observed.

Other effects that can occur upon electron irradiation, but were not investigated, are local charging and electron beam induced heating. However, these are assumed to be insignificant, as charging would presumably lead to lateral spreading of structural features [61], and the heat dissipation is presumably not influenced by 2-3 layer of 2HTPP. The origin of the formation of the carbon-free and carbon-rich areas therefore remains speculative, but the peculiar composition offers interesting possibilities for further nanostructuring, as demonstrated in the following chapter.

4.1.4 Catalytic activity of deposits on 2HTPP-covered substrates

Next, experiments were conducted to investigate if the different carbon contents in the deposits described in the previous chapter result in different catalytic activities of the inner and outer part. In order to do so, and with the idea of fabricating layered, bi-compositional deposits with a stacking sequence ABAB by means of autocatalytic growth, deposits fabricated on 2HTPP-covered substrates were exposed to alternating precursors, i.e. deposits from $Co(CO)_3NO$ were exposed to $Fe(CO)_5$, then again to $Co(CO)_3NO$ and so on. Sufficient catalytic activity of the deposit can then lead to precursor decomposition and subsequent autocatalytic growth at RT, as observed for $Co(CO)_3NO$ on pure Fe deposits from $Fe(CO)_5$ [69]. Note that for each characterization between individual precursor dosing steps described in the following, a new structure was used in order to avoid electron beam induced effects due to the SEM imaging, i.e. the base layer was fabricated four times.

Figure 4-15a depicts a 4×4 µm² square deposit fabricated by EBID, with $Co(CO)_3NO$ on 2HTPP/TiO_2(110). As expected, a pronounced SEM contrast between inner and outer part is observed, however the inner part is darker in this case. Local AES was conducted, with the respectively coloured stars indicating the positions. The results described in the previous
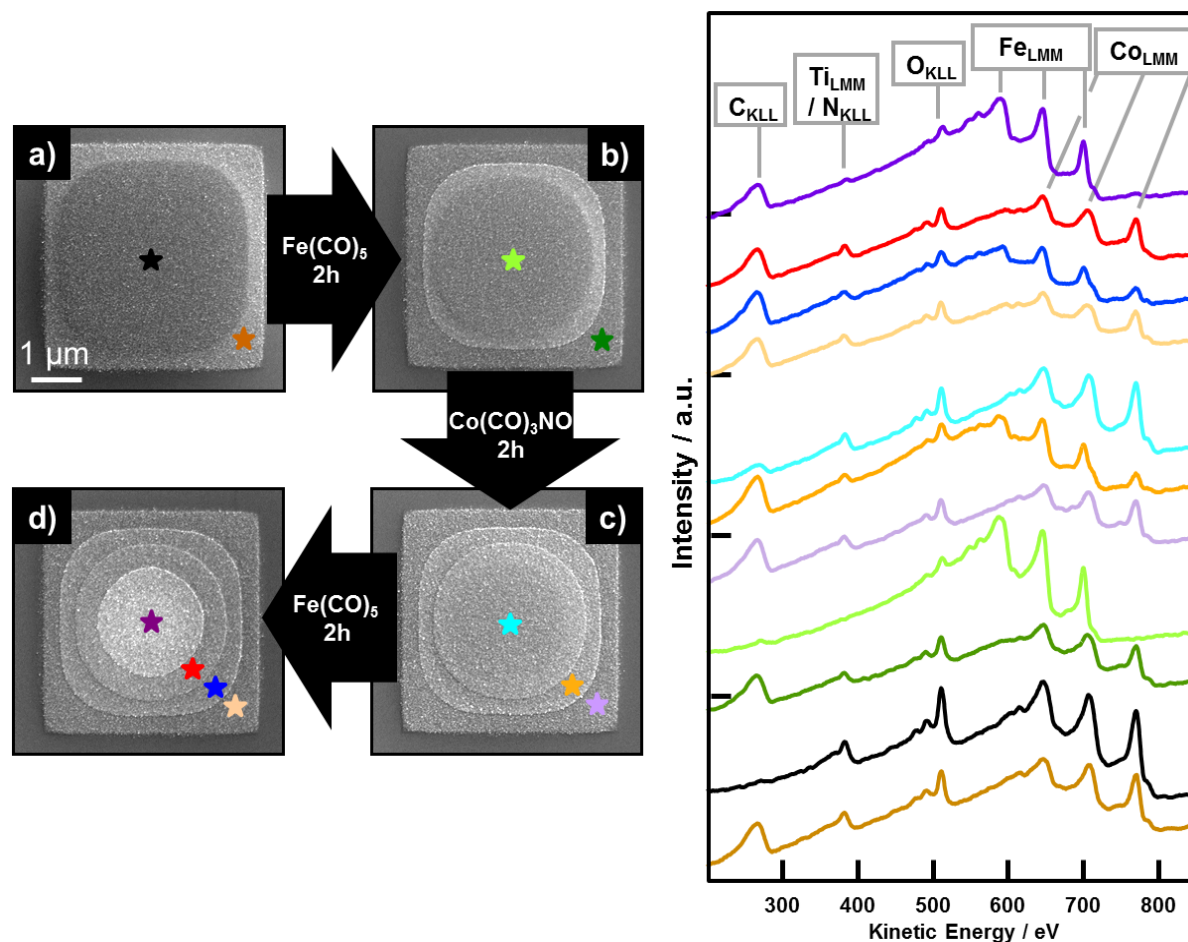
Figure 4-15: *Formation of a bicompositional, layered deposit on 2HTPP/TiO$_2$(110). a) SE micrograph of a 4×4 µm² square deposit fabricated with Co(CO)$_3$NO (EBID, 0.59 C/cm², t_{AG} = 259 min); b) deposit after an additional dosage of ~ 4.8 × 10^4 L Fe(CO)$_5$: this second layer is confined to the inner part of the first layer, and exhibits an SEM contrast and different carbon contents as well; c),d) deposit after additional dosages of ~ 4.8 × 10^4 L Co(CO)$_3$NO (c) and Fe(CO)$_5$ (d): both layers are also confined to the inner part of the layer below; the carbon content of the inner part is increasing with increasing number of layers. Right side: local AE spectra recorded at positions indicated with respectively coloured stars.*

chapter are reproduced, i.e. both areas predominantly consist of cobalt, smaller amounts of oxygen and nitrogen, and the outer part contains carbon whereas the inner part does not. Next, the deposit was exposed to ~ 4.8 × 10^4 L Fe(CO)$_5$, and the resulting structure is depicted in Figure 4-15b. It can be seen that an additional layer has grown in the inner part, whereas the outer part is unchanged. High magnification SE micrographs show that the second layer consists of cubic Fe crystallites (not shown). This is confirmed by local AES:

the inner part consists of almost pure Fe with only minor carbon and oxygen impurities, and the outer part has the same composition as before. Interestingly, the second layer also exhibits an SEM contrast like the first layer, i.e. a darker inner part and a brighter outer part. In a third step, the deposit was exposed to ~ 4.8×10^4 L $Co(CO)_3NO$, and the result is depicted in Figure 4-15c. Again, an additional layer has grown, but confined to the inner part of the second layer. Local AES shows that the third layer again consists of cobalt, oxygen, nitrogen and minor amounts of carbon, and the outer part of the second layer (orange) exhibits signals of cobalt, iron, oxygen, nitrogen, and significant amounts of carbon. The composition of the first layer is practically unchanged. The third layer again exhibits an SEM contrast, a darker inner part and brighter outer part, albeit less pronounced than in the first and second layer. In a fourth step, the deposit was again exposed to ~ 4.8×10^4 L $Fe(CO)_5$, with the result depicted in Figure 4-15d. As before, the fourth layer is confined to the inner part of the layer below, resulting in a stepped pyramid shaped deposit after the final dosing step. Local AES shows that the top layer consists of iron, with significant carbon impurities. The third layer exhibits a higher carbon content, but was measured on the outer part in contrast to before, and the first and second layer are practically unchanged.
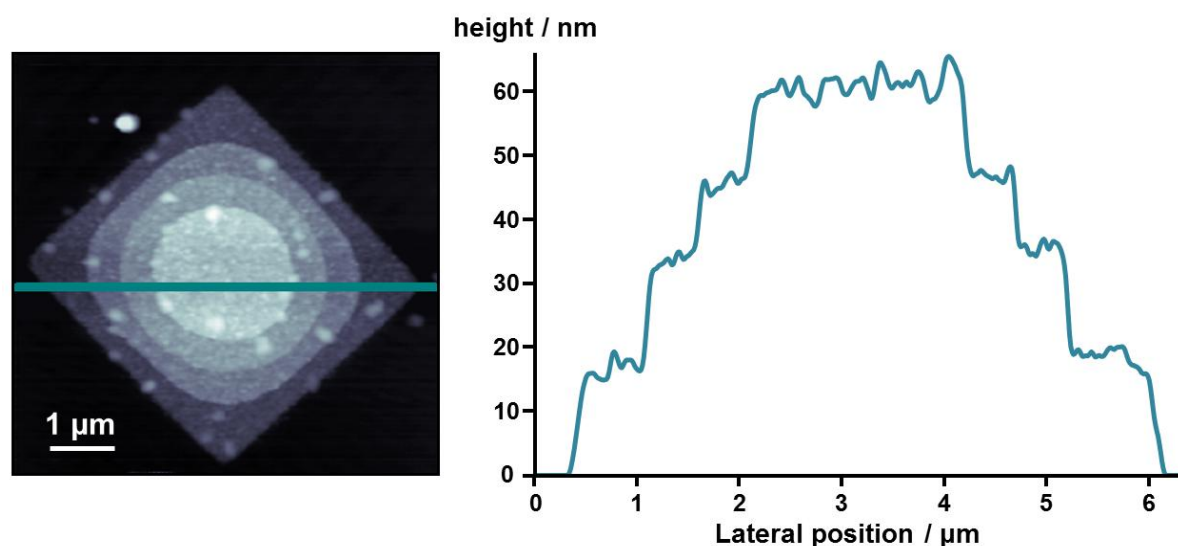
Figure 4-16: *Left: AF micrograph of the layered deposit depicted in Figure 4-15 (4). Bright particles are attributed to impurities due to exposure to ambient conditions. Right: Line profile over the deposit, with the position indicated in the micrograph.*

To obtain information concerning the topography of the deposit depicted in Figure 4-15d, it was investigated with an ambient AFM. The resulting micrograph is depicted in Figure 4-16, along with a line profile across the structure. Small particles on the deposit, which are not observed in the SE micrograph, are presumably impurities due to the exposure to ambient conditions. The linear profile confirms the stepped, pyramidal shape of the deposit, with the individual layers being 10-20 nm thick and almost flat on top.

From these findings, the following can be concluded. Upon exposure of deposits fabricated from $Co(CO)_3NO$ on $2HTPP/TiO_2(110)$, and probably on any suitable substrate covered with 2HTPP, to $Fe(CO)_5$, dissociation and subsequent autocatalytic growth occurs spatially selective on the inner, carbon-free area. Note that this was also observed for the exposure of $Co(CO)_3NO$ on a deposit fabricated from $Fe(CO)_5$ on $2HTPP/TiO_2(110)$ (not shown). It is assumed that the relatively high carbon content in the outer part is the reason for its lack of catalytic activity. As both parts exhibit the same morphology, and only differ in SEM brightness and carbon content, a possible explanation might be that catalytically active sites are covered with a carbonaceous layer. During the formation of the next layer, again a

separation into brighter and darker areas takes place. These areas again come along with different carbon contents, however this difference becomes smaller with increasing number of layers. This can be concluded from the spectra recorded on the third layer, where the outer part (red) exhibits a considerable carbon content, and the inner part (turquoise) exhibits a smaller, but detectable content, in contrast to the first layer, where no carbon is present (black). This principle of the formation of two different areas and spatially selective precursor dissociation continues to the fourth layer, which exhibits a significant carbon content in the inner part. The binary appearance and composition of the second and higher layers resembles the first layer, but it is assumed that their formation mechanisms are different as in the first layer, the electron beam is involved, and the extent of the inner part increases with increasing primary electron dose, whereas the growth of additional layers
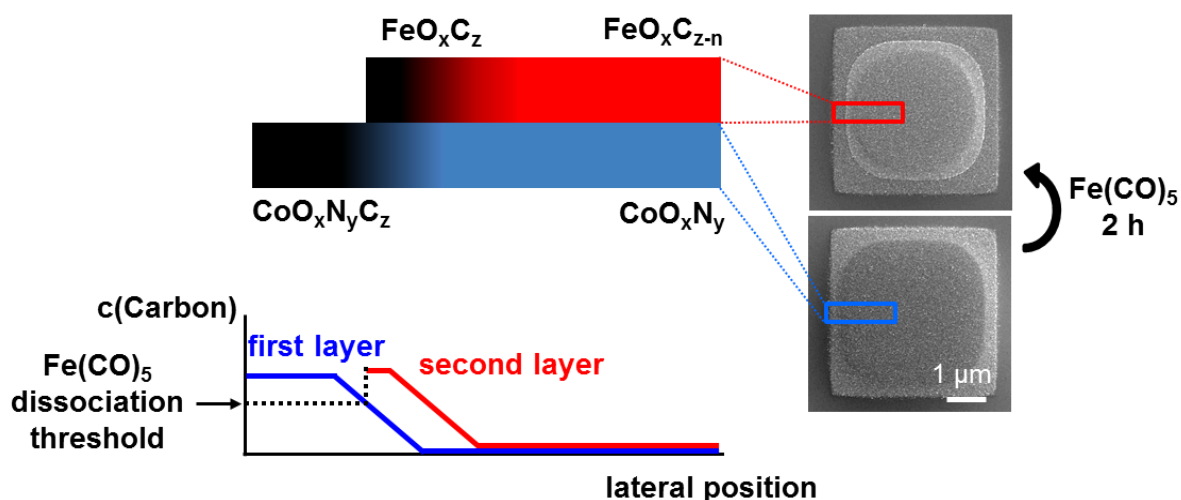
Figure 4-17: *Suggested model for the formation of the pyramidal, layered deposit on 2HTPP/TiO$_2$(110). A carbon concentration gradient exists at the boundary between inner and outer part of the first layer. Below a certain concentration threshold, Fe(CO)$_5$ can dissociate, and the newly formed layer then also exhibits a carbon concentration gradient, leading again to the same process in the third layer when Co(CO)$_3$NO is supplied.*

solely relies on catalytic effects.

In Figure 4-17, a possible model for the formation of the inner and outer part in the second and higher layers is suggested. The basic assumption is that at the interface

between inner and outer part in the first layer, the carbon concentration does not abruptly drop to zero, which is considered unlikely. Instead, it gradually decreases, as schematically indicated by the transition from black ($CoO_xN_yC_z$) to blue (CoO_xN_y) for the first layer (lower SE micrograph). Next, $Fe(CO)_5$ is supplied, and dissociates on the carbon-free area. However, it possibly also dissociates on sites that contain carbon, i.e. on the carbon concentration gradient, until a certain concentration threshold value is reached above which the catalytic activity of the first layer is inhibited, as depicted in the lower left diagram. The second layer then also exhibits a carbon concentration gradient, e.g. due to incomplete decarbonylation, indicated by the transition from black (FeO_xC_z) to red (FeO_xC_{z-n}), and consequently, the same effect occurs when an additional layer is grown on top. This might explain the fact that in higher lying layers, carbon is present in the inner part, as the carbon concentration gradient does not diminish to zero.

In summary, an experiment was conducted with the aim of fabricating layered, bi-compositional deposits on 2HTPP/TiO_2(110), by means of (auto-)catalytic decomposition of alternating precursors on an EBID deposit fabricated from $Co(CO)_3NO$. It was found that $Fe(CO)_5$ decomposes and grows autocatalytically only in the inner part of the base layer, which is attributed to the carbon present in the outer part. Like the base layer, the iron layer consists of an outer part with a significant carbon content and of an inner part with a strongly reduced carbon content. Upon exposure of this structure to $Co(CO)_3NO$, decomposition is also confined to the inner part of the layer before. This phenomenon results in a stepped pyramid shaped deposit with alternating layers of CoO_xN_y (C_z) and FeO_x (C_z). A model is suggested to explain the formation mechanism of the binary composition in the second layer and above. It is based on the assumption that a carbon concentration gradient exists between the inner and outer part of the base layer, and decomposition in the second layer only takes place once the carbon concentration falls below a certain threshold, and a concentration gradient is then formed in the next layer as well. However, this explanation is speculative and more work has to be done to gain deeper understanding of the underlying mechanisms.

4.2 Evaluation of surface activation and electron scattering parameters via EBISA combined with MC simulations

4.2.1 Introduction

The recently introduced EBISA technique allows investigating basic scattering properties of substrates. This is due to the separation of electron irradiation and precursor dosage, meaning that no material deposition and therefore no forward scattering occurs during electron irradiation. Thus, in EBISA only BSEs and SEs contribute to deposit formation (BSE proximity effect), and the maximum extent of proximity effects is limited by the BSE escape radius. Therefore it is possible to study the influence of BSE proximity effects independently. This is in contrast to EBID, where scattering might also take place in already deposited material (FSE proximity effect).
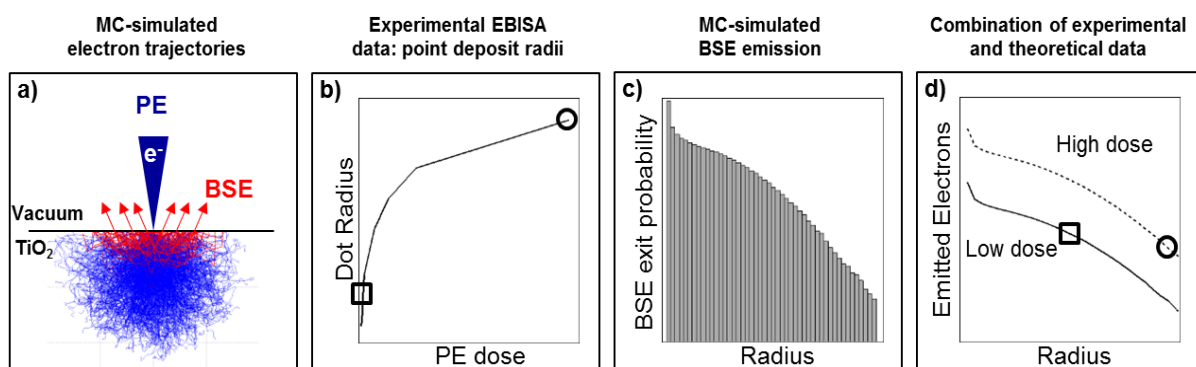
Figure 4-18: *Scheme of the study design; a) electron scattering in TiO$_2$; blue trajectories terminate (at E < 50 eV) within the substrate, red trajectories represent emitted BSEs; b) dependence of the experimentally observed dot radius on the total PE dose; square and circle markers indicate low and high PE dose, respectively; c) MC simulation result of the BSE exit probability vs. radius for a given PE energy and material (note: ordinate in log scale); d) absolute emitted electrons vs. radius for low (solid) and high (dotted line) PE dose; markers indicate the respective simulated electron dose at the experimentally observed dot radius.*

In order to to evaluate the scattering and basic surface activation parameters, a combination of experimental EBISA and theoretical Monte-Carlo data was applied. A scheme of the study design is depicted in Figure 4-18. A series of point irradiations (single pixel) with increasing dwell time (i.e. total PE dose) were carried out on various surfaces and subsequently developed using $Fe(CO)_5$ as precursor. The autocatalytic growth of iron nanostructures during this development step yields polycrystalline, high-purity Fe nanostructures, which can easily be observed in SEM. Due to the electron scattering the point irradiation leads to the formation of circular structures on the surface, the size of which increases with increasing electron doses (Figure 4-18a, b).

The corresponding MC simulation gives the radial BSE emission probability, which allows calculating absolute numbers of BSEs per area for a given PE dose and radial position (Figure 4-18c, d). These curves can then be compared with the observed point deposit radii, yielding the critical backscattered electron dose d_{crit}. This critical electron dose is the minimum amount of BSEs per area necessary to activate the surface such that it becomes catalytically active towards precursor dissociation, resulting in deposit formation. This evaluation procedure allows quantifying and comparing d_{crit} for different substrates and allows for a deeper understanding of the activation mechanisms in EBISA.

4.2.2 Results and discussion

Prolonged irradiation of an isolated point (i.e. single pixel) in EBISA results in the activation of areas with radial symmetry around the impact point due to BSE proximity effects. After the activated areas were developed by autocatalytic growth of $Fe(CO)_5$, the size of the resulting Fe structures was investigated to assess the dependency on the incident electron dose. Figure 4-19a depicts a series of such Fe deposits prepared on a ~ 1 nm thin multilayer (~ 2-3 layer) of 2HTPP on Ag(111) and highlights the importance of the incident electron dose for the final lateral size of the deposit. In the following, 2HTPP/X will denote a similar multilayer of 2HTPP molecules on substrate X (X is either Si(111), Ag(111) or rutile TiO_2(110)). Figure 4-19b juxtaposes Fe deposits of the same incident dose (720 nC) on various surfaces, namely SiO_2/Si, TiO_2, 2HTPP/Si, 2HTPP/TiO_2 and 2HTPP/Ag.
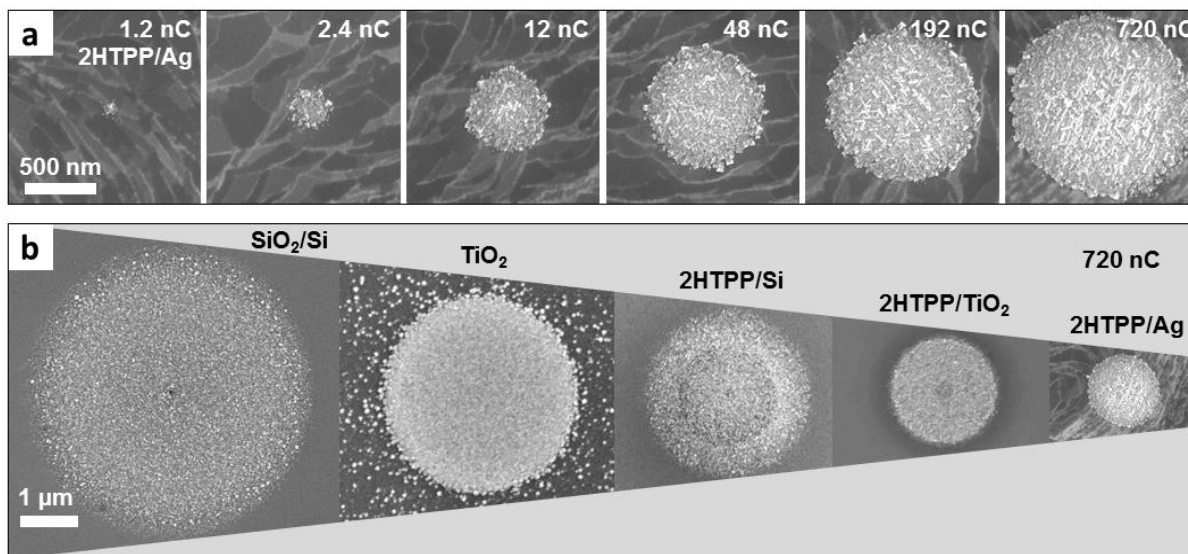
Figure 4-19: *a) EBISA-fabricated Fe deposits on ~ 2-3 layer of 2HTPP on Ag(111). The structures were fabricated using the indicated doses of 15 keV primary electrons and developed by autocatalytic growth of $Fe(CO)_5$. The size of the structures grows larger as the cumulated number of BSE at a certain range increases for higher total PE doses. (b) Fe deposits on different substrates fabricated using similar parameters: EBISA, 15 keV beam energy, 720 nC incident dose, total precursor exposure of ~ 10^5 L $Fe(CO)_5$. The difference in deposit size is due to the different electron scattering properties and activation mechanisms.*

Two trends can be extracted from the data: (a) the size of the deposit on 2HTPP layers decreases for denser support materials, i.e., Si (ρ = 2.34 g/cm³, Z = 14) > TiO_2 (Rutile; ρ = 4.23 g/cm³, Z_m = 12.67) > Ag (ρ = 10.49 g/cm³, Z = 47); (b) the deposit size on the pristine oxide surfaces (SiO_2, TiO_2) is larger compared to the same substrates covered with 2HTPP.

In order to better understand both trends, MC simulations of the electron backscattering corresponding to the experiments were conducted with the general-purpose radiation-transport Monte-Carlo-simulation code system PENELOPE [99]. Electron trajectories were terminated either when the electron left the substrate or when their energy dropped below 50 eV, as the employed transport model is not valid for lower energies. It should therefore be considered that the present simulation results do not account for low energy electrons, the focus is on the backscattered electrons and on emitted Auger electrons. In addition, the crystalline nature of substrates cannot be taken into account using this formalism; yet the lack of experimental evidence for an influence of the crystal structure, e.g., deposit asymmetry, suggest that this is not a critical factor in the evaluation. Finally, the surface

layer of SiO_2 for the Si substrate and the 2HTPP layers for all substrates were not included in the MC simulation itself. This is justified, as their limited thickness (1 – 2 nm) compared to the bulk scattering depth of 15 keV incident electrons (few µm) do not significantly alter the scattering behavior and no fundamental difference in the escape depth of BSEs is expected compared to the pristine surface.

In Figure 4-20, the resulting normalized BSE densities of the substrates Ag (black),
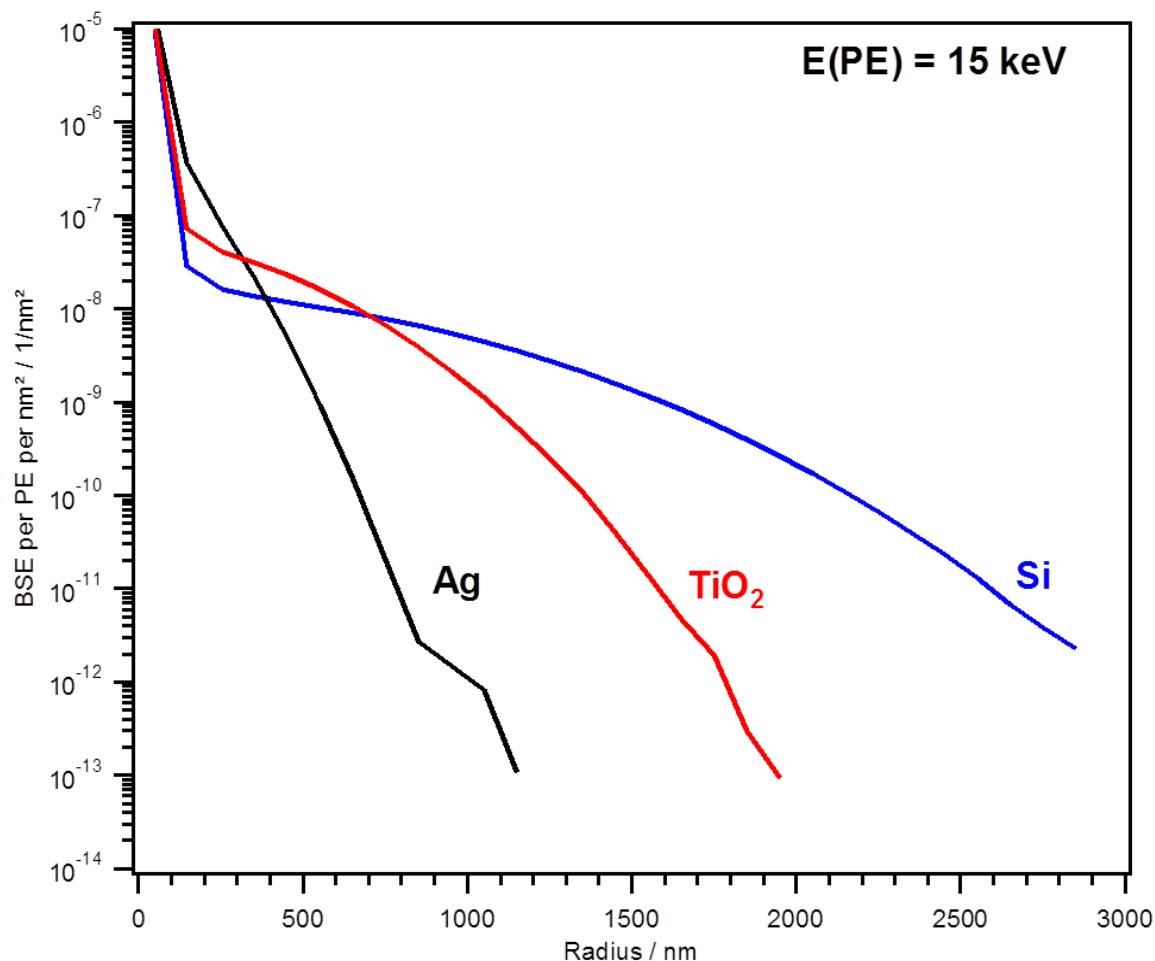
Figure 4-20: *BSE densities per incident primary electron vs. exit radius for Ag, TiO₂ and Si, and a beam energy of 15 keV.*

TiO₂ (red) and Si (blue) are plotted against the exit radius for a 15 keV primary electron beam, as used in the corresponding experiments. They reproduce the observed decrease of the BSE exit radius for Si > TiO₂ > Ag (Figure 4-19). Note that these curves are expressed as the relative density of BSEs per incident primary electron. Scaling these curves by the

number of incident electrons gives the absolute radial BSE density distribution. An example of such distributions for the silicon substrate, again for 15 keV incident electrons, is depicted in Figure 4-21 for four different electron doses. These curves can then be cross-referenced with the experimentally observed radii to evaluate the critical electron dose d_{CRIT} at respective deposit radius on the corresponding BSE density curve. Figure 4-22 depicts these d_{CRIT} vs. radius curves for all of the discussed systems. The incident electron dose increases from left to right for all curves, concluding with the highest dose of 720 nC at the rightmost end of each curve (indicated by the square marker). The substrate types are color-coded (black – Ag, red – TiO_2, blue – Si) while the surface type is coded by line style

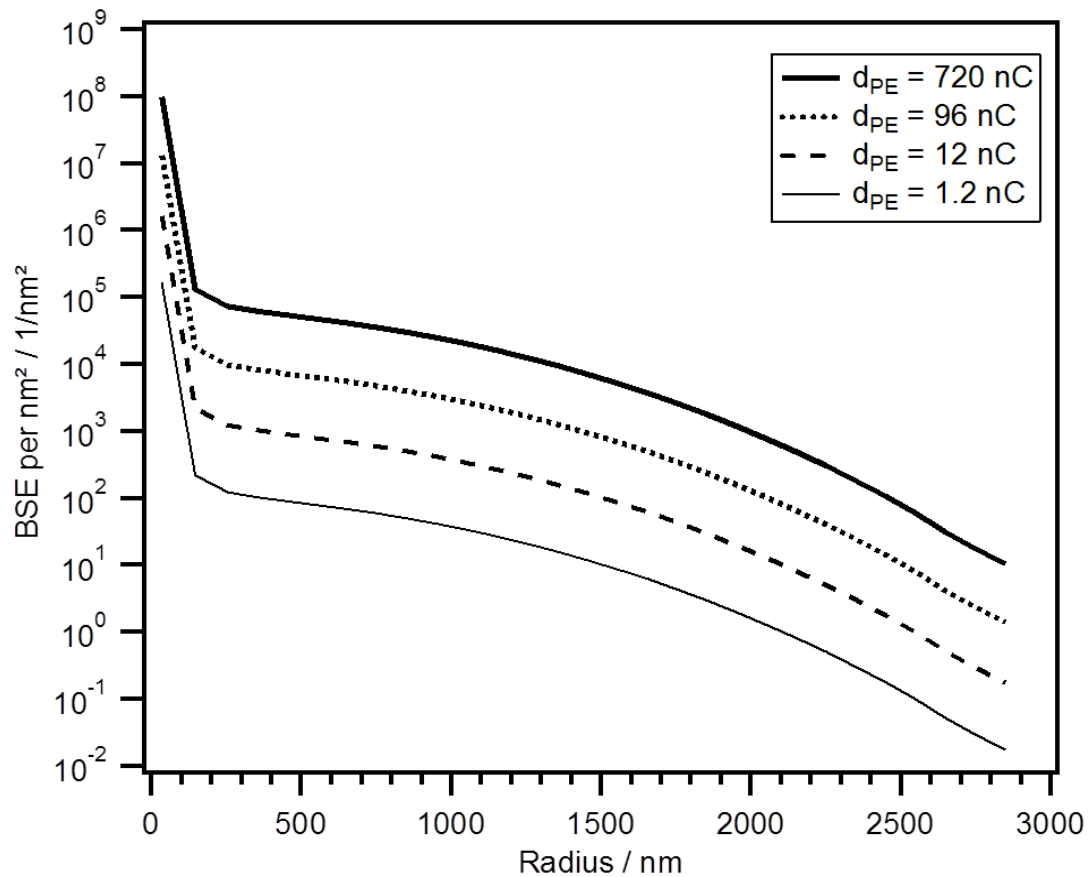**Figure 4-21:** *Calculated, absolute number of emitted BSEs for a spot irradiation at r = 0 nm for a Si sample and an incident electron energy of 15 keV. Different line styles indicate the respective primary electron dose d_{PE}. This data can be cross-referenced with experimentally determined deposit radii to determine a critical BSE dose for activation so that only areas with $d_{BSE}(r) > d_{CRIT}$ will be activated.*
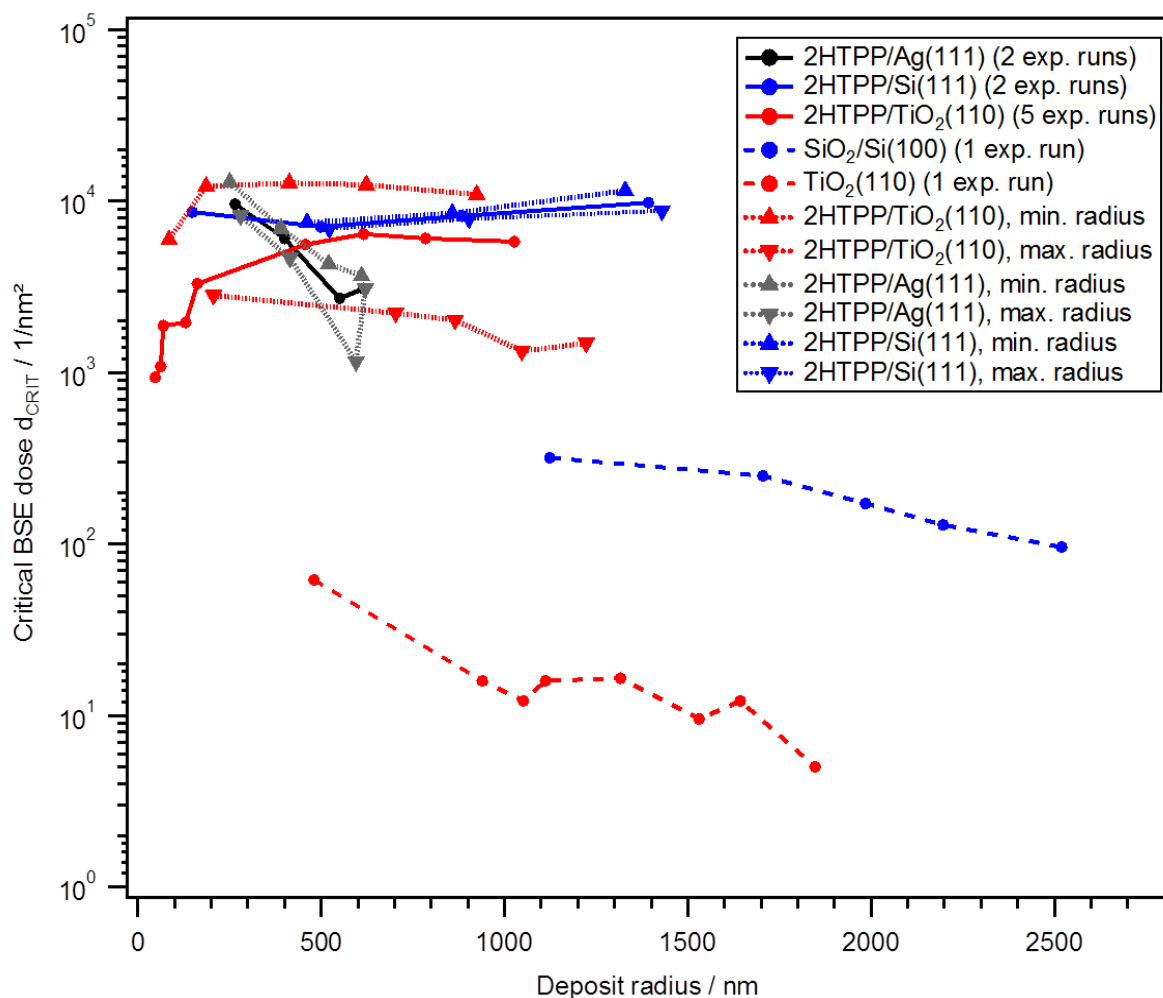
Figure 4-22: *Critical BSE dose d_{CRIT} plotted vs. experimentally determined deposit radii. Dashed lines indicate oxide substrates, on which one experimental run was conducted. The solid lines correspond to substrates covered with thin 2HTPP layers, on which multiple experimental runs were conducted. The dotted lines indicate the corresponding curves when using the highest or lowest measured radii. Number of measurements for each substrate: TiO_2: 1, SiO_2: 1, 2HTPP/Ag(111): 2, 2HTPP/Si(111): 2, 2HTPP/TiO_2(110): 5. The required BSE dose for activation of 2HTPP-terminated substrates is similar, and the activation dose for SiO_2 (blue, dashed) and TiO_2 (red, dashed) are lower by about one and two orders of magnitude, respectively.*

(2HTPP – solid, oxide – dashed) for easier comparison.

The absolute values of d_{CRIT} range from 10^1 BSE / nm² for the most susceptible surface, TiO_2(110), to 10^4 BSE / nm² for the 2HTPP-covered substrates, while the SiO_2 surface exhibits an intermediate d_{CRIT} of about 10^2 BSE / nm². TiO_2 and SiO_2 surfaces differ by more

than one order of magnitude, while all 2HTPP-covered substrates exhibit a similar d_{CRIT}, about 1-2 magnitudes higher than for SiO_2. On TiO_2 and SiO_2, d_{CRIT} decreases with increasing radius. On the 2HTPP covered substrates, the trend is not that clear: on 2HTPP/Ag(111) d_{CRIT} also decreases with increasing radius, and on 2HTPP/Si(111) and 2HTPP/TiO_2, d_{CRIT} is almost constant. The deposit radii deviated considerably in multiple experiments, especially on 2HTPP/TiO_2(110) (see figure caption for the number of experiments conducted in each system). The dotted lines depict the corresponding curves when using the highest or lowest measured deposit radii from the different experimental runs. The resulting BSE densities deviate by nearly one magnitude on 2HTPP/TiO_2(110), thus, other parameters (e.g. precursor quality) appear to considerably influence the deposition. Therefore no further assessments concerning the trends of the BSE densities on the 2HTPP-covered substrates will be made at this point.

As d_{CRIT} has the same magnitude on the 2HTPP covered substrates, the activation of 2HTPP layers appears to be virtually unaffected by the physical and chemical properties of the underlying surface. This is in line with the proposed activation mechanism for multilayers of 2HTPP on Ag(111) [10], which states that porphyrin molecules in higher layers are electronically decoupled from the substrate and thus susceptible to electron-induced chemical reactions, e.g. dissociation, without quenching of the active species by the substrate.

The different magnitudes of d_{CRIT} can be explained by different cross sections of the corresponding reactions upon electron impact. One can therefore conclude that the average cross section for the activation of a 2HTPP layer is several magnitudes lower than for TiO_2(110) and SiO_2/Si(100). In the case of TiO_2(110) and SiO_2/Si(100), these reactions would be the ionization of the Ti 3p and Si 2p levels, assuming the observed oxygen loss follows the Knotek-Feibelman mechanism [57]. To the best of the authors knowledge, no electron impact ionization cross sections of the Ti 3p level have been reported so far in literature [100]. In the case of the 2HTPP layer, it is possible that the active species are formed by a variety of different reactions, such as ionization of different shells (possibly also X-ray induced), electron attachment etc., and these reactions exhibit different cross sections. All corresponding cross sections are depending on the energy of the incoming electron, and the different dissociative electron-molecule interactions have cross section maxima at electron energies down to few eV [53]. Thus, it is necessary to consider the energy distributions of the emitted electrons, especially with low energy electrons included.
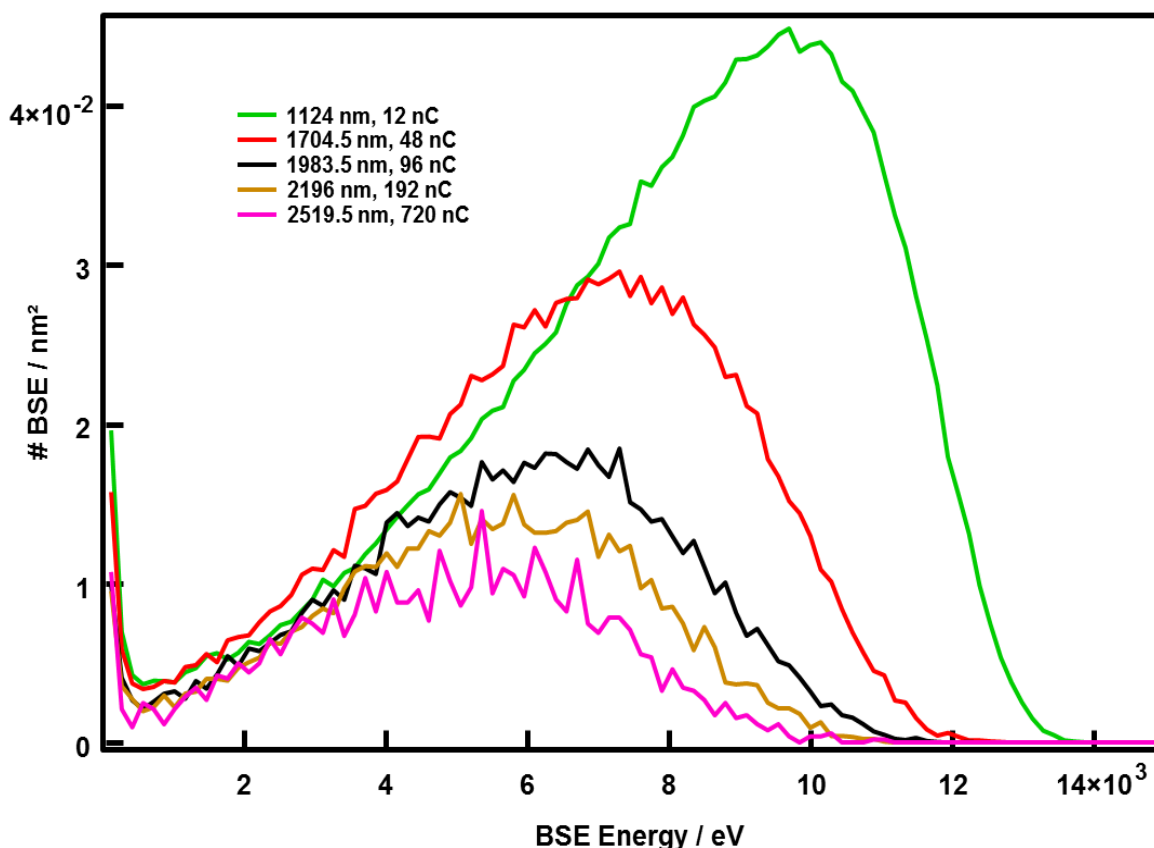
Figure 4-23: *BSE energy distributions for different distances to the 15 keV electron beam impact point on Si. The distances correspond to the deposit radii obtained with the indicated primary electron doses, and integrating over the curves would give the respective d_{CRIT}.*

Furthermore, spectroscopic studies are needed to obtain information concerning the electron induced reactions that occur during electron irradiation of the 2HTPP layer.

The decrease of d_{CRIT} on the oxide surfaces with increasing distance to the electron beam impact point might also be explained with an increase in the cross sections of the corresponding Ti 3p and Si 2p ionization reactions. Electron impact ionization cross sections usually increase with increasing electron energy to a maximum at an overvoltage (ratio of the energy of the impact electron to the binding energy) of ~ 4, and then decrease again [100]. Thus, it is necessary to consider the energy distribution of the electrons that escape the surface at the corresponding distance from the electron beam impact point, i.e. at the position of d_{CRIT}. Figure 4-23 depicts the energy distributions at the different d_{CRIT} for $SiO_2/Si(100)$. Note that in these simulations the low energy cutoff was 125 eV. The curves are scaled to the employed primary electron dose, giving an absolute amount of BSE / nm²

as a function of the BSE energy. With increasing distance, the intensity maxima shift to lower BSE energy, from ~ 9 keV at 1124 nm to ~ 5 - 6 keV at 2519.5 nm. This would explain the decrease in d_{CRIT}, as the ionization cross section increases with decreasing electron energy. To further simplify, one might first consider only the maximum cross sections at an overvoltage of ~ 4, which would be around ~ 140 eV for Ti 3p (4 × 35 eV) and ~ 400 eV for Si 2p (4 × 100 eV). However, at electron energies of the Si 2p ionization cross section maximum (~ 400 eV), the BSE intensity is slightly higher at 1124 nm than at 2519.5 nm. In this simplified picture, the decrease in d_{CRIT} is therefore not explained by these energy distributions as one would expect a higher amount of BSE at ~ 400 eV for 2519.5 nm, as d_{CRIT} is lower at this distance. It is therefore concluded that simulations which include low electron energies (< 125 eV) would be necessary along with cross section data over the whole energy spectrum, to weight the electrons according to their cross section and thus make a valid statement concerning their impact on d_{CRIT}. It is also possible that different reaction pathways that do not follow the Knotek-Feibelman mechanism lead to the observed oxygen loss, and thus reactions with different cross sections would have to be considered.

To conclude, this chapter presented a procedure to assess the critical BSE densities d_{CRIT} required to activate $TiO_2(110)$, SiO_2 and various 2HTPP-covered substrates (2HTPP/X) for the catalytic decomposition of $Fe(CO)_5$, by comparing experimental EBISA data with MC simulations. First, EBISA point deposit radii were experimentally obtained on the respective surfaces. MC simulations using the PENELOPE code were used to obtain the absolute BSE densities as a function of the distance to the electron beam impact point. The critical (i.e. minimum required) BSE density d_{CRIT} was then obtained at the corresponding radius on the BSE density curve. Three general trends were observed: 1) d_{CRIT} is approximately the same for all 2HTPP/X, 2) it increases over several magnitudes from $TiO_2(110)$ to SiO_2 to 2HTPP/X, 3) it decreases by up to one magnitude for increasing radii on $TiO_2(110)$ and SiO_2. Thus, the average cross section for activating the 2HTPP layer is lower. The fact that d_{CRIT} is approximately the same for all 2HTPP/X is interesting, as it means that the 2HTPP activation is independent of the chemical and physical properties of the underlying surface. The observed differences in d_{CRIT} on the different substrates, as well as the decrease with increasing radius on the oxide substrates, appear to be challenging to explain. It is considered likely that different average cross sections of the corresponding electron induced reactions are the decisive factor. To assess these average cross sections, simulations that

include low energy electrons and cross section data over the respective energy spectrum would be required.

4.3 FEBIP on surface-anchored metal-organic frameworks

4.3.1 Introduction

In this work, the field of FEBIP is expanded to a novel class of substrates, namely Surface-Anchored Metal-Organic Frameworks (SURMOFs). A brief introduction to SURMOFs is presented in chapter 3.3.4, including the two SURMOFs used in this work. From the FEBIP perspective, the porosity of SURMOFs is highly interesting, as the precursor molecules can potentially diffuse into the substrate, provided the framework has a sufficiently large pore size and is chemically inert towards precursor decomposition. This diffusion might lead to additional precursor transport channels, which severely impacts the FEBIP process, as on standard bulk substrates material deposition can be limited by surface diffusion of precursor molecules to the point of impact of the electron beam. Another interesting aspect would be the ability to deposit material inside the SURMOF by exploiting the interaction volume of the scattered electrons. By varying the electron beam energy and therefore changing the interaction volume, one might even be able to control the depth of the deposit, potentially enabling controlled deposition in three dimensions. Due to the low density of SURMOFs compared to the bulk materials commonly used in FEBIP, one also anticipates reduced electron backscattering and thus reduced proximity effects. Conversely, FEBIP presumably also benefits the fabrication and application of SURMOFs. A straightforward way would be the flexible deposition of nanoscaled interconnects for conductivity measurements. Similar to what has been done with micro contact printing and electron beam lithography [101], but on a smaller scale, FEBIP could also be used to fabricate templates for the localized growth of SURMOFs, e.g. by fabrication of a gold deposit and subsequent selective anchoring of the SAM on it. This might also be done on an already deposited SURMOF, opening up strategies to fabricate complex structures also in the vertical direction by successively applying the method on the locally grown SURMOF.

The first part of this chapter presents EBID and EBISA experiments with the precursors $Fe(CO)_5$ and $Co(CO)_3NO$, typically followed by autocatalytic growth, conducted on two different SURMOFs: HKUST-1 and Zn-DPDCPP. HKUST-1 was chosen as it is very well investigated and is regarded as a "standard" SURMOF, while Zn-DPDCPP was chosen as it is chemically similar to 2HTPP, which, in form of multilayers on Ag(111), TiO_2(110) and

Si(111), has been demonstrated to be a suitable substrate for EBID and EBISA (chapter 4.1.2 and reference [10]). With this in mind, one objective is to find out potential similarities and differences in the FEBIP process between Zn-DPDCPP and 2HTPP, e.g. the possibility to be activated for EBISA, which might allow drawing general conclusions concerning porphyrin-based substrates in FEBIP.

The second chapter presents a series of EBID experiments with $Fe(CO)_5$ on HKUST-1 that were performed with the aim of obtaining line structures with the smallest possible line width and spacing. The motivation is whether one can exploit the aforementioned properties of SURMOFs for the fabrication of structures with minimal feature size. The low density compared to bulk substrates results in a lower backscattering coefficient, along with this a lower secondary electron coefficient, and consequently reduced proximity effects at the same primary electron dose. If this is the case, one might expect the minimum deposit feature sizes to approximately have the beam spot size, which is one of the objectives of this experiment. The high porosity might lead to additional precursor transport channels through the bulk, and consequently a higher precursor concentration at the electron beam impact point compared to standard bulk samples, where surface diffusion and adsorption from the gas phase are the only transport channels. This might lead to a more homogeneous deposit, as the precursor surface density strongly influences the shape of EBID deposits [5]. First, a detailed description of the process will be given, which was performed in an iterative manner to optimize the lithographic parameters. These will be described in detail, along with exemplary SE micrographs to demonstrate their influence on the deposit shape. The best results in terms of minimum FWHM and pitch, as well as best possible homogeneity are presented along with an AES analysis.

The precursor background pressure was set to 3.0×10^{-7} mbar during all experiments and autocatalytic growth processes presented in this chapter, corresponding to a surface pressure of ~ 9.0×10^{-6} mbar (chapter 3.1.1). The autocatalytic growth time for all EBISA structures was 270 min, and is given in the respective figure caption for EBID structures.

4.3.2 FEBIP on HKUST-1 and Zn-DPDCPP

First, the results of EBID and EBISA experiments and subsequent autocatalytic growth with both precursors on a Zn-DPDCPP SURMOF will be discussed. As discussed before this substrate was the first choice, since one might anticipate susceptibility to EBISA regarding the similarities to the free-base porphyrin layers explored previously (Chapter
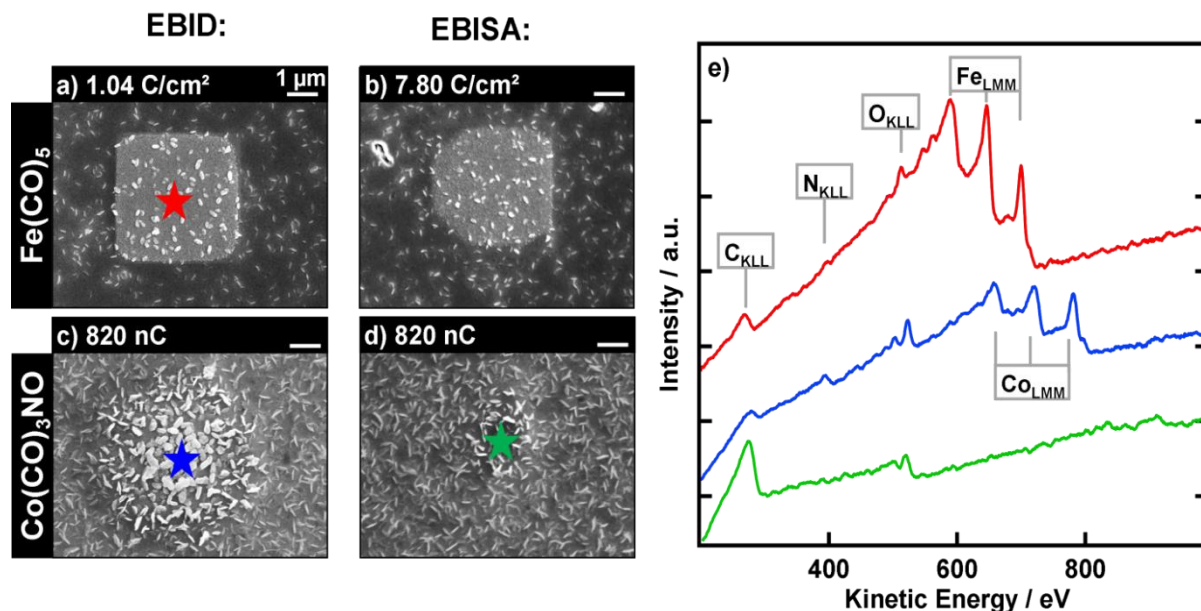
Figure 4-24: *Results of FEBIP experiments followed by autocatalytic growth on the SURMOF Zinc 5,15-diphenyl-10,20-di(4-carboxyphenyl)porphyrin (Zn-DPDCPP); a) SE micrograph of a 4×4 μm² square deposit fabricated by EBID with Fe(CO)$_5$; t_{AG} = 245 min; b) 4×4 μm² square deposit fabricated by EBISA with Fe(CO)$_5$. c) point deposit fabricated by EBID with Co(CO)$_3$NO; t_{AG} = 241 min; d) point deposit fabricated by EBISA with Co(CO)$_3$NO; e) Local AE spectra recorded at the positions indicated with respectively coloured stars. The EBISA structure b) deposited with Fe(CO)$_5$ is assumed to have approximately the same elemental composition, i.e. nearly pure iron, as structure a) due to the autocatalytic growth process. The green spectrum only exhibits substrate signals and thus confirms that no deposition occurred when using EBISA with Co(CO)$_3$NO.*

4.1.2). Figure 4-24a depicts a SE micrograph of a 4×4 μm² square deposit fabricated from Fe(CO)$_5$ by EBID and autocatalytic growth, and the corresponding local AE spectrum is depicted in red in Figure 4-24e. The deposition is confined to the irradiated area, and the autocatalytic growth process results in the formation of pure, crystalline iron. The observed carbon signal might either originate from the SURMOF below, or from the elongated protrusions which are observed on the whole substrate and appear to stick out of the deposit. Figure 4-24c depicts the SE micrograph of an EBID point deposit fabricated from Co(CO)$_3$NO and AG, i.e. the beam dwelled stationary at one position during deposition until a total electron dose of 820 nC was accumulated. Local AES (Figure 4-24e, blue spectrum) shows that the deposit consists of cobalt, oxygen, nitrogen and possibly carbon. As

expected, the deposit is roughly of circular shape with a radius that vastly extends that of the electron beam due to proximity effects, however, the material is deposited inhomogeneous due to the rough surface. These experiments prove that the porphyrin based Zn-DPDCPP SURMOF is suitable for EBID, even though the rough surface is a drawback regarding the fabrication of spatially well-defined structures. Further experiments were then conducted to evaluate whether EBISA is possible on this substrate. Figure 4-24b depicts an SE micrograph of an EBISA deposit fabricated from $Fe(CO)_5$ with subsequent autocatalytic growth. Growth of crystalline iron on the square-shaped pre-irradiated area is observed, albeit not in the expected square shape, for which no conclusive explanation has been found yet. Therefore it can be concluded that EBISA works for $Fe(CO)_5$ on the porphyrin SURMOF and consequently a corresponding activation mechanism must exist. Interestingly, EBISA did not work for the precursor $Co(CO)_3NO$ on the same substrate. Figure 4-24d depicts an SE micrograph of a surface site after a point-irradiation with 820 nC, and subsequent autocatalytic growth. A slight brightness difference of the irradiated spot is observed in SEM, and the corresponding local AE spectrum (Figure 4-24e, green spectrum) exhibits only signals from Zn-DPDCPP. This shows that no material was deposited, meaning that EBISA did not work for $Co(CO)_3NO$ but for $Fe(CO)_5$ on Zn-DPDCPP. This chemical selectivity is especially remarkable since EBISA worked for both precursors on thin 2HTPP layers on different substrates (chapter 4.1.2).

Overall the FEBIP experiments on Zn-DPDCPP revealed that EBID and EBISA are possible, and exhibited an unexpected precursor selectivity in EBISA. A major drawback of the porphyrin SURMOF was the rough surface topography, which severely complicates the fabrication of well-defined nanoscale structures. Therefore the next step was to explore FEBIP on a smoother surface, namely HKUST-1. Figure 4-25a-f depicts a series of SE micrographs of 4×4 µm² square deposits, and Figure 4-25m depicts a more complex structure (a simplified SURMOF scheme) fabricated with $Fe(CO)_5$ on HKUST-1. The series of square deposits were fabricated with two different beam energies, 5 and 15 keV, each with a variation in primary electron area dose. In Figure 4-25a ($Fe(CO)_5$, 5 keV, 0.088 C/cm²), a minor brightness difference between irradiated and non-irradiated areas is observed, and only scattered growth of crystallites in the central part. At higher electron doses (Figure 4-25b, c; 0.234 C/cm² and 1.171 C/cm²), deposition is observed on almost the whole irradiated area, except at its periphery. No unselective deposition, which might take place due to proximity effects or thermal decomposition, was observed on non-irradiated areas. In addition, local AES was conducted on the three mentioned deposits (Figure 4-25n,
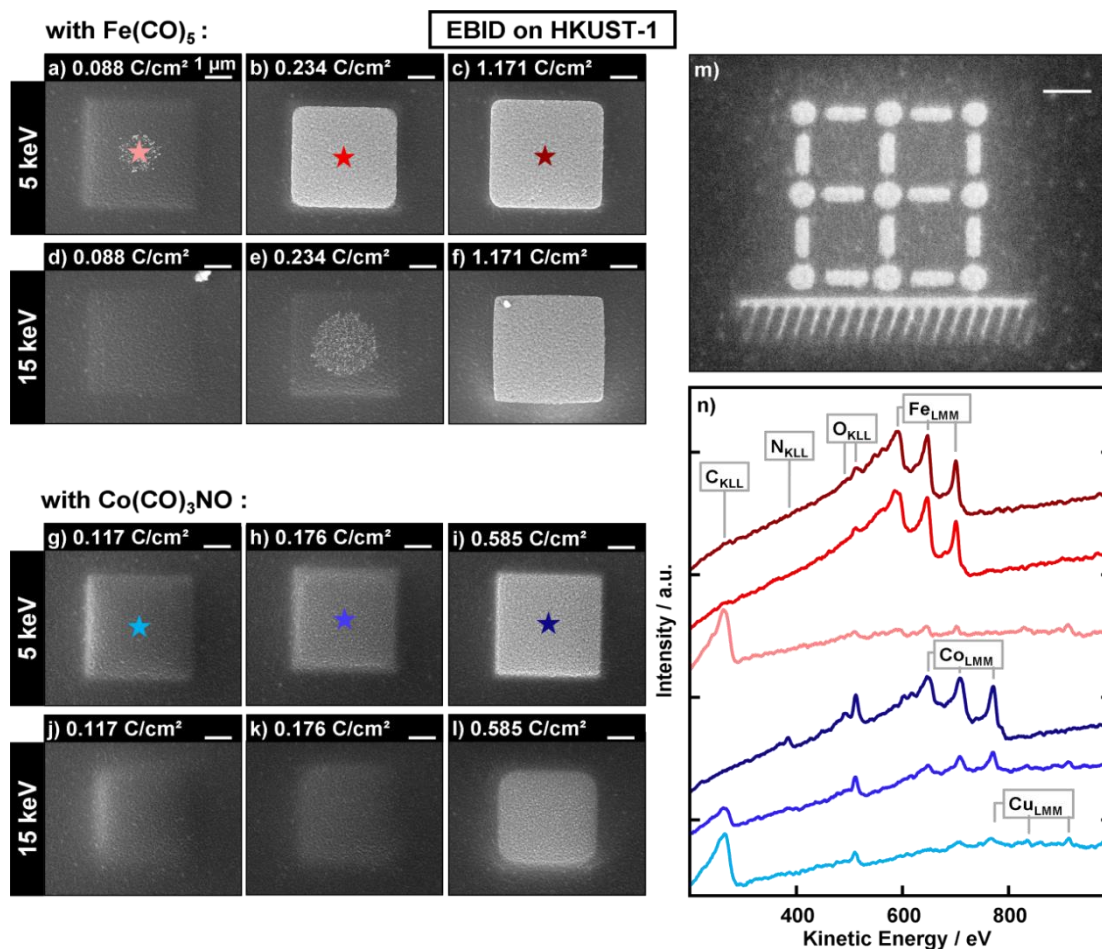
Figure 4-25: EBID on HKUST-1; all deposits written with the indicated beam energy and I_{Beam} = 400 pA; a)-f) SE micrographs of 4×4 µm² square deposits fabricated from Fe(CO)$_5$ with the indicated electron doses and autocatalytic growth times t_{AG} of: a) 257 min, b) 247 min, c) 238 min, d) 217 min, e) 202 min, f) 191 min. g)-l) 4×4 µm² square deposits fabricated from Co(CO)$_3$NO with the indicated electron doses and autocatalytic growth times t_{AG} of: g) 258 min, h) 252 min, i) 241 min, j) 212 min, k) 207 min, l) 198 min; m) Simplified scheme of a SURMOF fabricated with Fe(CO)$_5$; E_{Beam} = 15 keV, t_{AG} = 82 min; n) local Auger Electron spectra recorded at the sites indicated with stars of the same colour.

positions indicated in the SE micrographs by the respectively colored stars). The two deposits fabricated with higher electron doses consist of basically pure iron, with only minor amounts of oxygen, whereas the deposit fabricated with the lowest electron dose exhibits only minor amounts of iron, as expected from its appearance in SEM, while the spectrum is dominated by substrate signals. The series of deposits written with a 15 keV beam shows the same trend, i.e. more deposition of nearly pure, crystalline iron at higher primary electron

doses. However, compared to deposits written with the same primary electron dose but lower beam energy, compare e.g. Figure 4-25b and e, significantly less deposited material is observed.

The same variation of lithographic parameters was conducted during deposition of 4×4 μm² squares from $Co(CO)_3NO$ (Figure 4-25g-l), and the same trends as in the series of iron deposits are observed: increased material deposition at higher primary electron doses and lower beam energies (noticeable at the peripheries of structures i and l), and spatial selectivity of deposition to irradiated areas. Local AES shows that during the autocatalytic growth process, aside from cobalt, a significant amount of oxygen as well as nitrogen are incorporated into the deposit. In contrast, the deposits contain no carbon, which is evident from the spectrum of the deposit written with 0.585 C/cm², while the deposits written with lower doses are presumably not thick enough to completely attenuate the carbon signal from the HKUST-1 below. The following can be concluded from these findings. Using the EBID protocol and subsequent autocatalytic growth with $Fe(CO)_5$ and $Co(CO)_3NO$ on a HKUST-1 and Zn-DPDCPP SURMOF, spatially well-defined nanostructures (Figure 4-25m) can be obtained. With the experimental parameters used, deposition takes place once a critical effective electron dose is exceeded, where effective electron dose means the total number of PEs, SEs and BSEs crossing the substrate-vacuum interface. Due to their lower energy than the PEs, SEs and BSEs have higher cross sections to induce the various possible precursor dissociation reactions, and are therefore generally perceived to be the main contributors to deposit formation in EBID [6]. As the non-primary electrons exhibit a spatial distribution with radial symmetry around the impact point of the primary beam, the effective electron dose is, in the case of the square-shaped deposits shown, higher in the central part than in the periphery, leading to the onset of deposit formation in the center upon increasing primary electron dose (Figure 4-25a, e). Similarly, the higher deposition rate using 5 keV compared to 15 keV beam energy is then attributed to an overall increase in SE and BSE emission. The experiments performed on the Porphyrin-based SURMOF Zn-DPDCPP show very similar results regarding spatial selectivity and elemental composition of the deposits, suggesting that SURMOFs are in general suitable substrates for EBID. The measured elemental compositions of the deposits shown are assumed to be the outcome of the autocatalytic growth process, and the results reproduce the findings concerning deposits fabricated with the same precursors, but on different substrates [8-10, 69]. Therefore it can be concluded that in these cases the composition of the autocatalytically grown material is independent of the underlying substrate, which demonstrates the high potential of
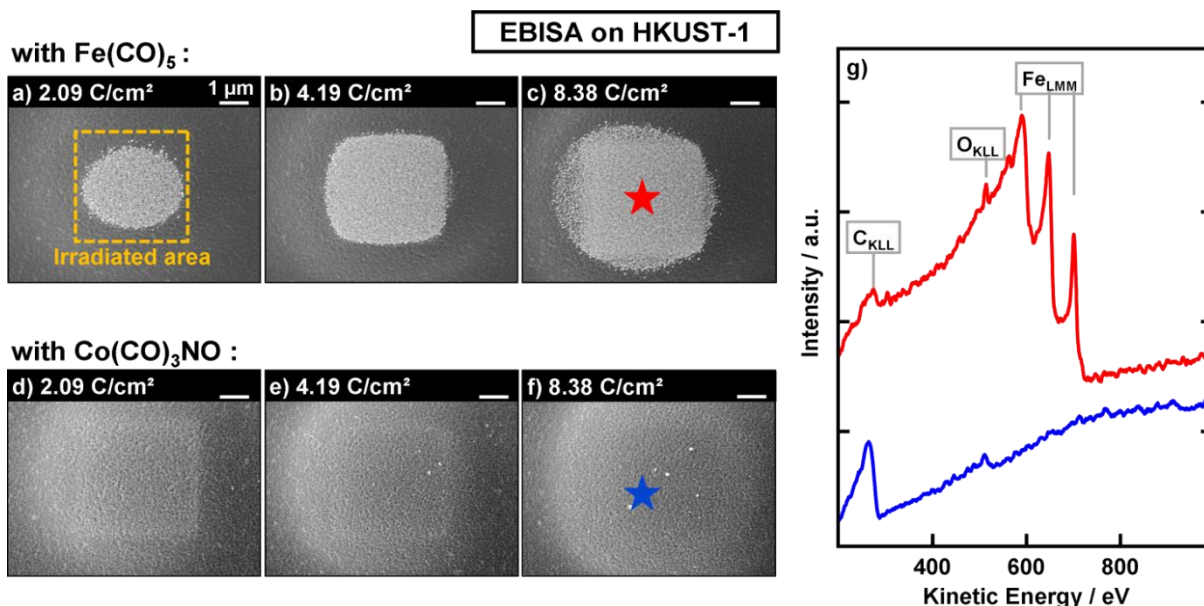
Figure 4-26: *EBISA on HKUST-1. All structures written with E_{Beam} = 20 keV, I_{Beam} = 3 nA, t_{AG} = 270 min. SE micrographs of 4×4 μm² square deposits fabricated from a)-c) Fe(CO)$_5$ and d)-f) Co(CO)$_3$NO with the indicated electron doses; g) local Auger Electron spectra recorded at the sites indicated with the respectively coloured stars. They confirm that EBISA with Fe(CO)$_5$ was successful, resulting in deposits consisting of nearly pure iron, and that no deposition took place when using Co(CO)$_3$NO.*

autocatalysis in FEBIP regarding the reproducibility of the elemental composition of the deposits.

Another set of experiments was then performed in order to find out if deposits can also be fabricated using the EBISA routine and autocatalytic growth with both precursors on HKUST-1. In Figure 4-26, SE micrographs of two series of 4×4 μm² square deposits, fabricated by EBISA and autocatalytic growth with Fe(CO)$_5$ (a-c) and Co(CO)$_3$NO (d-f) on HKUST-1, are depicted. In the case of Fe(CO)$_5$, deposited material can be clearly distinguished in SEM, and the presence of clean Fe is confirmed with local AES (Figure 4-26g), proving that EBISA was successful. Similar to EBID, we observe deposition in the center of the irradiated area at relatively low primary electron doses (2.09 C/cm², Figure 4-26a), whereas at increasing doses, Fe is deposited on the complete irradiated area and eventually outside of it due to proximity effects. Again, autocatalytic growth leads to the formation of cubic Fe-crystals, while only minor carbon and oxygen impurities are detected

in local AES. On the contrary, irradiated areas that have been exposed to $Co(CO)_3NO$ do not exhibit a pronounced contrast in SEM, aside from what is likely beam damage. Local AES performed in the area that has been irradiated with the highest electron dose (8.38 C/cm²) only shows signals from HKUST-1, confirming that no deposition from $Co(CO)_3NO$ occurred. Interestingly, HKUST-1 exhibits the same chemical selectivity towards the two precursors as Zn-DPDCPP. Thus, just as on Zn-DPDCPP, no deposition from $Co(CO)_3NO$ occurred in EBISA.

To gain more insight into the activation mechanism that leads to the dissociation of $Fe(CO)_5$, the influence of electron beam irradiation on HKUST-1 was studied. In order to do this, AE spectra were recorded while scanning the surface at different magnifications and therefore applying different electron area doses, which allows following potential intensity changes of the substrate AE signals as a function of the electron area dose. No significant changes in the C_{KLL} and Cu_{LMM} signal intensities were observed, but for O_{KLL}, shown in Figure 4-27a. Here, a series of AE spectra (O_{KLL} region) recorded with different scan areas is depicted, corresponding to applied electron area doses of 3.6×10^{-3} C/cm² (red, bottom) to 1.3×10^6 C/cm² (black, top, recorded with the beam stationary) until the O_{KLL} peak maximum is recorded at ~ 512 eV. One can clearly observe a decrease in peak area towards higher electron doses, which is also apparent from Figure 4-27b, where all normalized peak areas are plotted against the applied electron area dose. Thus, the topmost layers of the HKUST-1 become depleted of oxygen, and only carbon and copper remain (not shown), which strongly suggests decomposition upon electron irradiation.
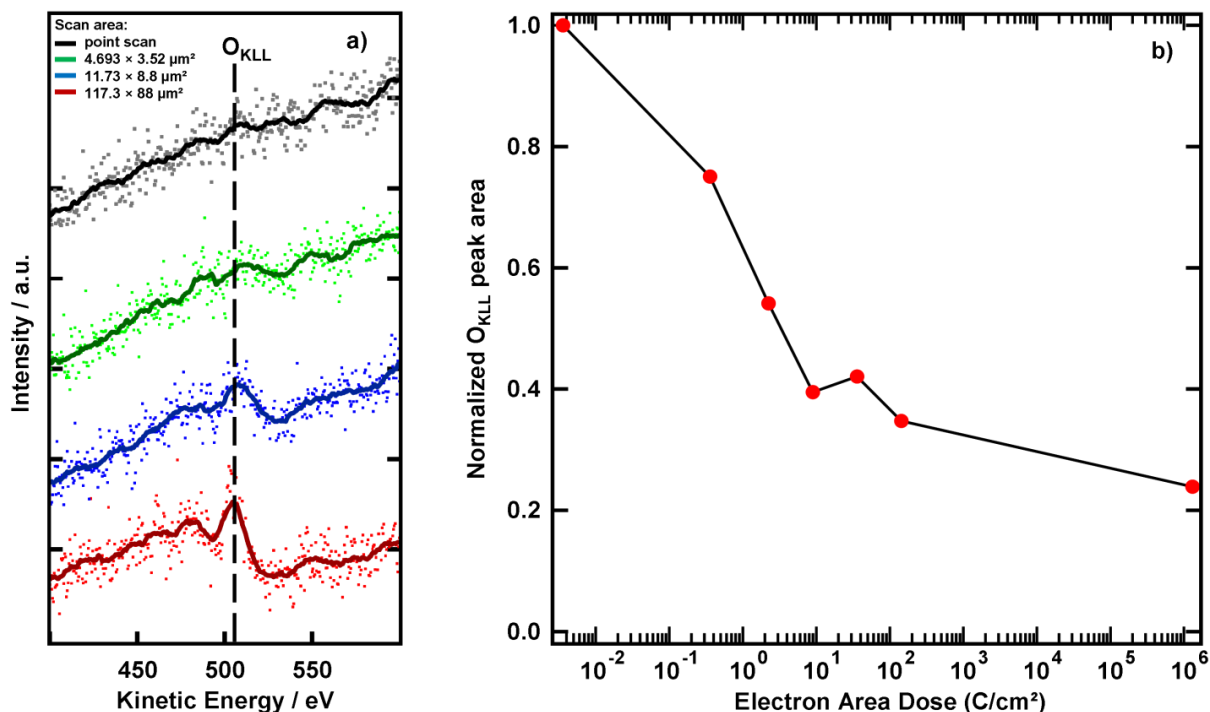
Figure 4-27: *a) Series of AE spectra in the O_{KLL} region recorded on HKUST-1 while scanning the surface with different SEM magnifications with E_{Beam} = 15 keV and I_{Beam} = 3 nA; the respective scan areas are displayed in the upper left. The black spectrum was recorded with a stationary electron beam having a diameter of ~ 3 nm; b) plot of the normalized O_{KLL} peak area (after a linear background subtraction) against the electron area dose, illustrating the decrease of oxygen content following electron beam irradiation.*

These findings demonstrate that HKUST-1 and Zn-DPDCPP are suitable substrates to fabricate clean iron nanostructures from $Fe(CO)_5$ using EBISA and autocatalytic growth, and in contrast, there are no indications that $Co(CO)_3NO$ decomposes at pre-irradiated surface sites. This further expands the range of substrates suitable for EBISA to SURMOFs which are novel to FEBIP in general. The catalytic activity resulting from the electron beam irradiation is completely selective towards decomposition of only one of the investigated precursors ($Fe(CO)_5$), which generally is an interesting property, e.g. when working with precursor mixtures, as it might allow for selective deposition of only one material. Although chemically closely related, EBISA with $Co(CO)_3NO$ is not possible on Zn-DPDCPP, but possible on thin 2HTPP layers (chapter 4.1.2). One possibility could be that electron irradiation of these substrates leads to different reaction products which exhibit different catalytic activity towards decomposition of $Co(CO)_3NO$. The results also provide some

insight into the effect of high energy electron irradiation on HKUST-1, but the exact chemical nature of the dissociation products remains speculative. One mechanism leading to oxygen removal might be an electron induced C-C bond scission between aromatic and carboxylic carbon atoms, followed by release of CO_2. Similar to what has been observed for electron irradiation of different organic compounds on surfaces [59, 93-95], other reactions might involve C-C and C-H bond scissions, leading to e.g. cross-linking of aromatic fragments and formation of reactive radical and ionic species which then initiate precursor dissociation and nucleation.

In summary, first FEBIP experiments on SURMOFs were conducted, a substrate class that is novel to the field. EBID and EBISA experiments with the precursors $Fe(CO)_5$ and $Co(CO)_3NO$ were conducted on the SURMOFs HKUST-1 and Zn-DPDCPP. EBID experiments with all precursor/substrate combinations were successful, yielding almost pure iron deposits with $Fe(CO)_5$, and cobalt deposits with oxygen and nitrogen impurities from $Co(CO)_3NO$, all after prolonged autocatalytic growth. EBISA experiments were successful with $Fe(CO)_5$ on both investigated SURMOFs, also yielding pure iron deposits after autocatalytic growth, but no deposition was observed when using EBISA with $Co(CO)_3NO$. It was demonstrated that electron irradiation of HKUST-1 leads to a reduced oxygen concentration in the probed topmost layers, which implicates dissociation of the SURMOF, and it is proposed that reactive dissociation products are the active species leading to dissociation of $Fe(CO)_5$.

4.3.3 Downscaling of deposits on HKUST-1

A series of EBID experiments was performed with $Fe(CO)_5$ on HKUST-1 with the aim of obtaining smallest possible feature sizes. Using the 'bitmap exposure.vi' (chapter 3.4.2), the input bitmap file used were nested-L structures, with the initial one depicted in Figure 4-28. The nested-L shape is commonly used in different lithographic methods as a benchmark pattern for the fabrication of structures with minimal feature sizes [102-105]. It consists of seven L-shaped lines that lie closely together in a nested manner, with the central one being longer than the rest. As highlighted by van Oven et al. [102], this enables the direct comparison of an isolated line with an array of densely packed lines, e.g. to investigate

possible proximity or replenishment effects. Furthermore, due to the lines oriented perpendicular to each other, effects of electron beam astigmatism might be revealed.

The aim of the experiment was to deposit this structure with a minimal line FWHM and pitch, both depicted in Figure 4-28. The FWHM was evaluated from integrated line profiles (see chapter 3.5), while the pitch d_p (distance between the centres of two adjacent lines) is defined by the preset step size and number of pixels between the lines in the input file (see chapter 3.4.2). At the same time, the deposit has to be well-defined, i.e. the lines should ideally exhibit the same SEM contrast and brightness at each position, as well as minimal cross-linking, and material should be deposited at all irradiated sites. In the following, the most important deposition parameters that were changed during the experiment and their influence on the deposit shape are described, and the best results are presented at the end of the chapter. Note that in this experimental series, the beam energy was 20 keV and the nominal beam current 200 pA during the FEBIP process and imaging.
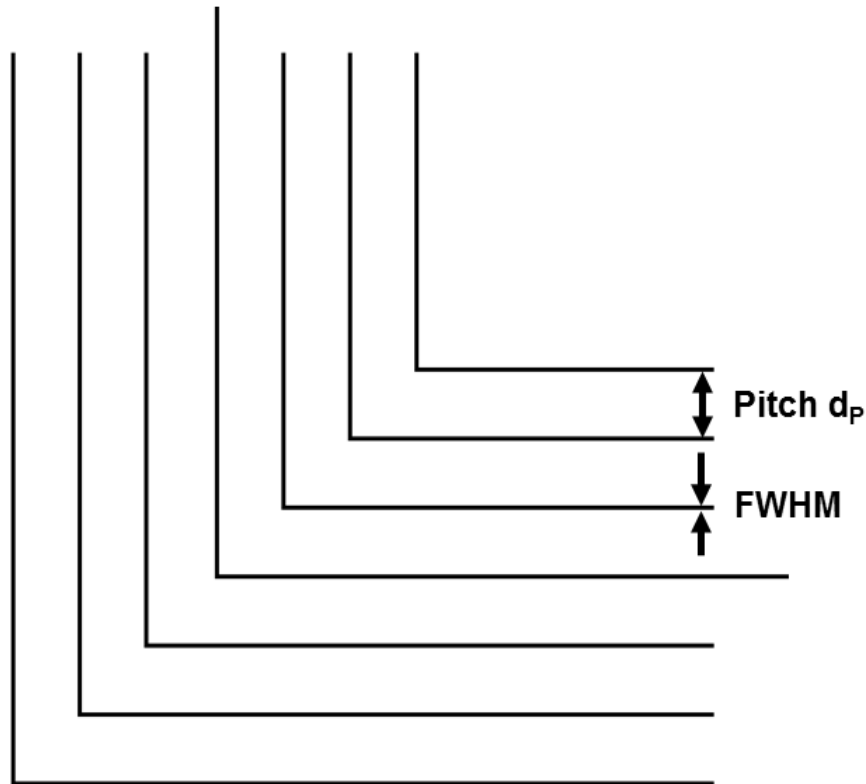

Figure 4-28: Exemplary nested-L blueprint as used in the presented experiments, which were performed with the aim of minimizing the line FWHM at a smallest possible pitch d_p.

Electron dose. To ensure a well-defined deposit, the dwell times at individual pixels have to be adjusted to compensate for proximity effects. As described in detail in chapter
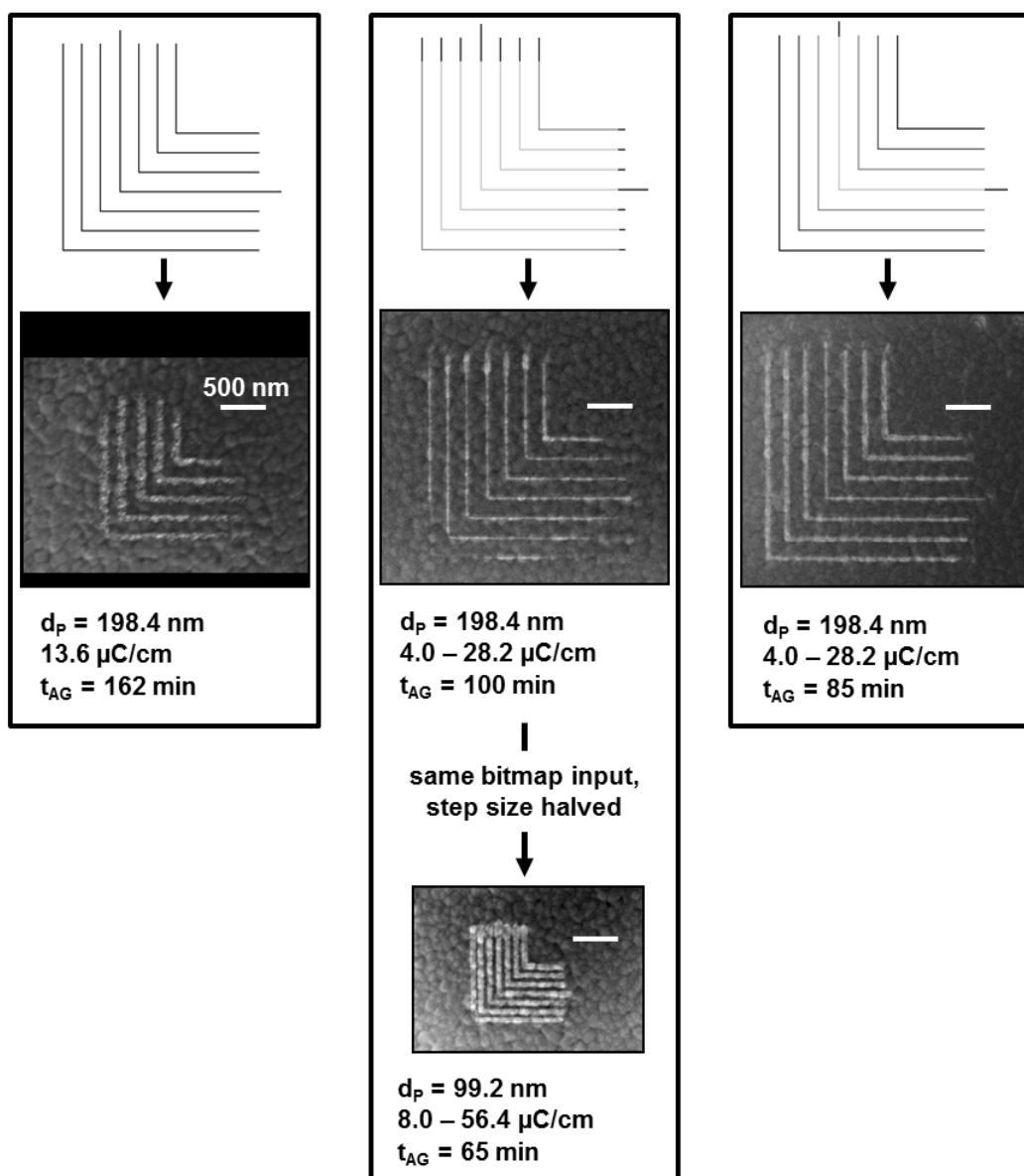
Figure 4-29: *Examples of how proximity effects can be compensated by appropriate adjustment of the RGB grey values in the input file. Left: Using the same electron dose per pixel results in an inhomogeneous deposit which lacks material deposition in the periphery. Centre and right: Stepwise adjustment of the grey values results in a more homogeneous deposit. Centre, bottom: Example of how an increase in the electron line dose by decreasing the step size affects the deposit.*

3.4.2, this can be done by changing the RGB grey values of the corresponding pixels, i.e. a brighter pixel means lower dwell time and thus electron dose. An example for such compensation is depicted in Figure 4-29. On the left side, a non-compensated input file was used (depicted top), i.e. all pixels were exposed to the same electron dose (resulting in 13.6 µC/cm line dose), and the resulting structure is depicted in the SE micrograph below. Only the central five of the nominally seven lines are visible, with an inhomogeneous material distribution, i.e. broader lines in the central part. Thus, the electron dose at the periphery of the structure is too low and too high in the center. To overcome this, a modified input file was used, depicted in the center top in Figure 4-29. The dwell time corresponding to a black pixel was increased to obtain a maximum electron line dose of 28.2 µC/cm, the two outer lines were irradiated with 14.1 µC/cm, whereas the inner lines were irradiated with reduced dwell times (minimum electron line dose 4.00 µC/cm). All seven lines are now deposited, although not continuously, and are mostly thinner than before. The input file was then further improved (Figure 4-29, right side) based on the discussed results, i.e. the outer lines were irradiated with 28.2 µC/cm and the line doses now gradually decrease towards the central line. This results in a deposit where all lines are continuously deposited, except at the edges of the outer lines, with nearly constant thickness except for the thinner central line.

In order to reduce the pitch, the same input file and dwell time was used and the step size reduced. An example for this step is depicted in the lower central part in Figure 4-29, where the step size was halved. In the resulting deposit all lines are discernible, but thicker compared to before. This is because the same total electron dose is now applied to a smaller area, effectively doubling the electron line dose. Therefore, after each downscaling step to reduce the pitch further adjustments of the input file and dwell times are necessary.

Autocatalytic growth time. As the deposits fabricated from $Fe(CO)_5$ can grow autocatalytically at RT in UHV, the autocatalytic growth time t_{AG} has to be adjusted accordingly to minimize lateral broadening of the lines. Figure 4-30 depicts three SE micrographs of nested-L structures that were deposited with the same parameters except different t_{AG}. At the longest growth time (Figure 4-30a, t_{AG} = 50 min), individual lines cannot be distinguished, i.e. the complete irradiated area is overgrown with Fe. With t_{AG} = 29 min (Figure 4-30b), the horizontal lines can be clearly distinguished, whereas the vertical lines are still overlapping. The reason for this is presumably not a different horizontal autocatalytic growth rate, but a small compression of the structure due to inaccurate beam positioning (cf. paragraph *number of sweeps* for details). With t_{AG} = 4 min (Figure 4-30c), the irradiated lines
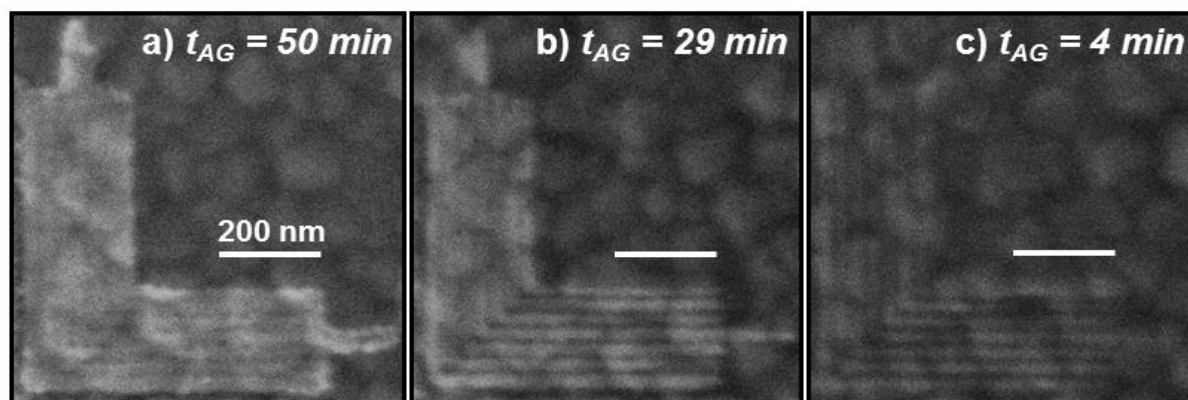
91

Figure 4-30: *Effect of the autocatalytic growth time t_{AG} one the deposit line width. All structures were written with 2.6-36.6 µC/cm, but with the different depicted t_{AG}. With $t_{AG} = 50$ min, the irradiated area is nearly completely overgrown with iron; with $t_{AG} = 29$ min, the horizontal lines are clearly separated, whereas with $t_{AG} = 4$ min, the lines are hardly discernible.*

are for the most part undistinguishable from the substrate, as not enough material is deposited.

Based on these results, a t_{AG} between 18-22 min was chosen for the fabrication of structures with minimal line width, in order to prevent cross linking of the lines and to ensure sufficient material is deposited such that all lines can be observed. Considering that with these t_{AG} the smallest achieved line FWHM were ~ 8-14 nm, the lateral growth rates of deposits from $Fe(CO)_5$ on HKUST-1 appear to be very similar to lateral growth rates that were measured in the same instrument, with the same growth parameters (pressure, temperature) on different substrates [106], i.e. 0.71 nm/min on native SiO_x/Si_3N_4 (200 nm) and 0.42 nm/min on SiO_x(300 nm)/Si(100).

Number of sweeps. As described in detail in chapter 4.1.3, varying the number of sweeps, while keeping the electron dose constant, can influence the deposition rate and therefore the lateral extent of a deposit feature. This is due to the so-called replenishment effect, meaning that adsorbed precursor molecules deplete during irradiation of a spot, leading to a decreasing deposition rate with increasing dwell time, which can be overcome by reducing the dwell time and letting the precursor concentration replenish while irradiating

the remaining structure. An example for this is depicted in the SE micrographs in Figure 4-31a and b. The structure shown in Figure 4-31a was deposited in one sweep (4.00-28.2 µC/cm) and material deposition is only sparsely observed in the central part, while the low
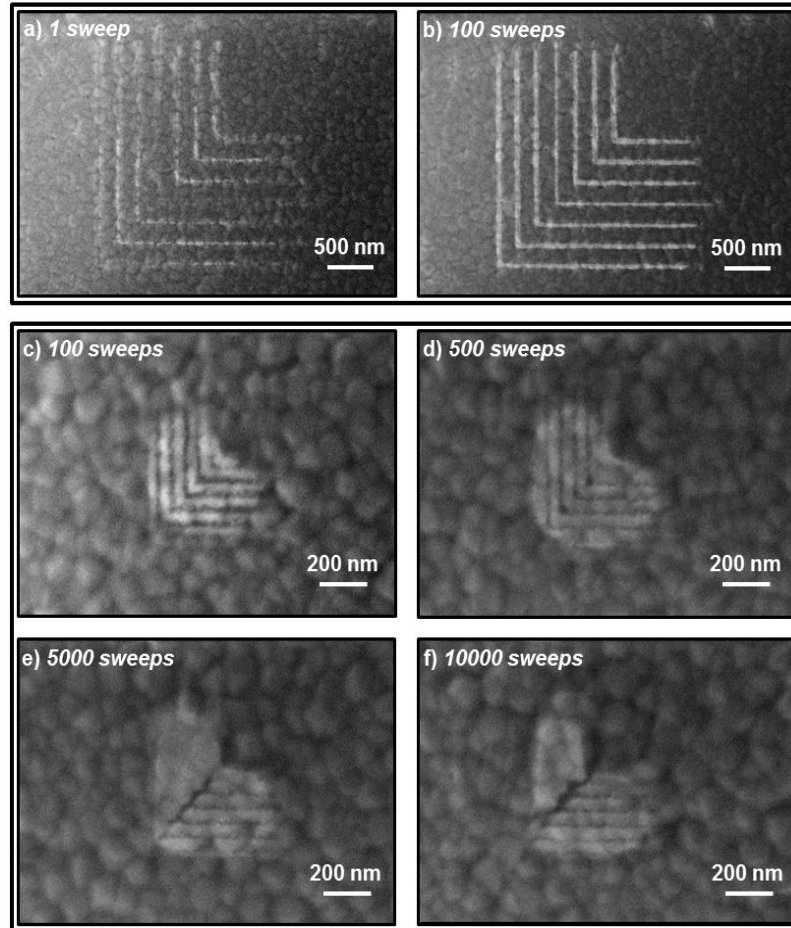
Figure 4-31: *Effect of the number of sweeps on the deposit; a), b) deposits fabricated with the same electron line dose (4.0-28.2 µC/cm, d_p = 198.4 nm), but with the different depicted amounts of sweeps. An increasing amount of sweeps leads to more material deposited, in a more homogeneous manner, due to the replenishment effect (cf. chapter 4.1.3); c)-f) deposits fabricated with the same electron line dose (4.0-28.2 µC/cm, d_p = 55.0 nm), but with the different depicted amounts of sweeps. Due to the decreasing dwell time per pixel with increasing number of sweeps, the vertical lines become distorted due to insufficient beam stabilization.*

brightness of the rest of the lines is ascribed to beam damage. In contrast, all lines were deposited homogeneously, except at the edges of the outer lines in the structure fabricated with the same electron dose but in 100 sweeps (Figure 4-31b). Therefore it is in principle beneficial to increase the number of sweeps to the instrumental limit. Figure 4-31c-f depicts a series of deposits which were fabricated with 100, 500, 5000 and 10000 sweeps respectively, with the same electron line dose as in Figure 4-21a,b but with d_p = 55.0 nm instead of 198.4 nm. The deposit fabricated with 100 sweeps exhibits only six lines, which are not continuous, but clearly separated from each other. With 500 sweeps, more material was deposited, i.e. the lines are broader, with less space inbetween. Using 5000 sweeps, the horizontal lines exhibit the same appearance as with 500 sweeps, however all vertical lines are now compressed towards each other and are completely overgrown with Fe. This trend continues when using 10000 sweeps, i.e. the vertical lines are indistinguishable and even more compressed towards each other, while the horizontal lines remain unchanged.

These examples demonstrate that an increase in the number of sweeps first leads to an increased amount of deposited material, generally resulting in more defined structures due to the reasons discussed above and in chapter 4.1.3. However, a further increase in sweeps eventually leads to a horizontal distortion of the deposit. This phenomenon is immanent to the electromagnetic beam deflection unit and was already described by Vollnhals [72]. The increase of sweeps goes along with a decrease in dwell time per pixel to keep the electron dose constant. With decreasing dwell times the beam movement speed over the surface becomes higher, and the position of the beam becomes increasingly difficult to stabilize by the electromagnetic deflection system before moving to the next pixel. As the nested-L exposure is performed in a raster scan fashion, (line by line from the top left to the bottom right), this instability becomes first apparent when the beam has to perform the jumps between the vertical lines, where it is moving at a faster speed compared to the horizontal lines, where the pixels are adjacent to each other. In the work of Vollnhals, the maximum beam movement speed until which stable beam positioning is possible was calculated to be ~ 0.01 ms^{-1}. Using the same formula, the horizontal beam movement speed when writing only vertical lines in the nested-L exposure with 5000 sweeps is calculated as

$$v_{h,1} = \frac{d_p}{t_d} = \frac{55.04 \text{ nm}}{1.2 \text{ µs}} = 0.046 \text{ ms}^{-1},$$

with the pitch (= jump distance) d_p and the dwell time t_d. This movement speed is above the threshold, therefore the vertical lines becomes distorted due to the inaccurate beam positioning. Similarly, the movement speed when writing only horizontal lines is calculated as

$$v_{h,2} = \frac{\Delta x}{t_d} = \frac{3.44 \text{ nm}}{1.2 \text{ μs}} = 0.0029 \text{ ms}^{-1},$$

with the step size Δx between the adjacent pixels. The value is below the threshold, therefore the horizontal lines are irradiated correctly. Consequently, the number of sweeps and thus dwell times in further experiments were chosen such that the beam movement speed always remains below the threshold value throughout the exposure, but close to the aforementioned instrumental limit.

Frame exposure and waiting time. In the course of downscaling the deposits, a particular challenge was that the outer L remained relatively undefined and broad, compared to well-defined inner lines, as exemplary depicted in Figure 4-32a. Several adjustments of the local electron line dose by varying the input file and dwell times did not result in a significant improvement. Therefore a square-shaped frame was added around the nested-L pattern. The idea behind this was that, for example, proximity effects from irradiating the
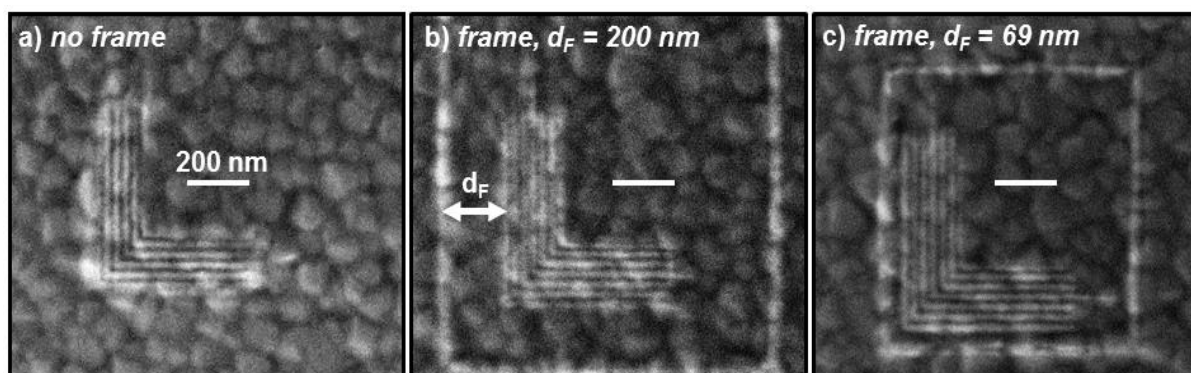

Figure 4-32: *Effect of writing a frame around the nested-L structure. All structures were written with the same electron line dose (11.56-173.4 μC/cm), but a) without frame, b) with a frame in a distance $d_F = 200$ nm, c) with a frame with $d_F = 69$ nm. The addition of a frame leads to an improvement in homogeneity, depending on the distance d_F.*

frame might be beneficial in terms of obtaining a more homogeneous distribution of BSE and SE on the nested-L deposit itself. Additionally, writing the two horizontal lines of the frame adds an effective waiting time between individual exposures of the nested-L structure, where the beam is not dwelling on any point of the nested-L structure. This might lead to an increased precursor concentration due to the replenishment effect, just as by increasing the number of sweeps, and therefore a more defined deposit.

Figure 4-32b depicts a deposit that was fabricated with the same electron dose as in Figure 4-32a, but now including a frame (38.6 µC/cm) with a distance d_F = 200 nm away from the outer L. All lines are now more defined than before, and the outer L is nearly continuous and is as broad as the other lines. When decreasing d_F to 69 nm (Figure 4-32c),
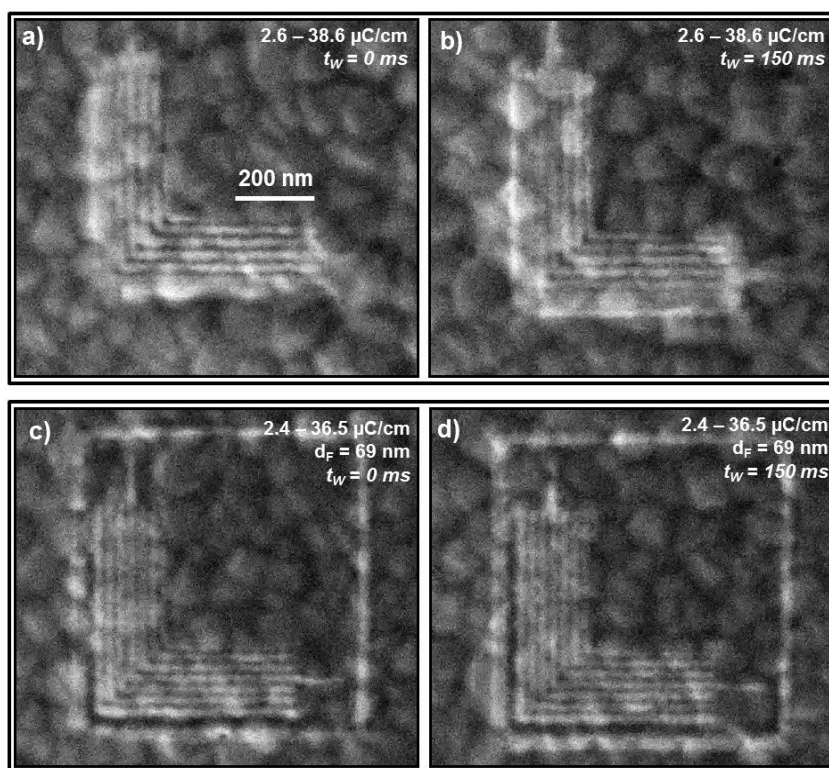
Figure 4-33: *Effect of introducing a waiting time t_W between individual sweeps. a) nested-L without waiting time; b) same electron line dose as in a), but now with t_W = 150 ms between sweeps; more material is deposited due to the replenishment effect. c) nested-L without waiting time, but with frame; d) same as c), but with t_W = 150 ms. No clear difference between both structures can be seen, presumably because writing a frame already introduces a waiting time of ~ 200 ms when the horizontal lines are written.*

the deposit is even more defined. To investigate whether it is the introduced waiting time between sweeps that leads to the improved deposits when writing a frame, additional experiments were performed. Figure 4-33 depicts nested-L structures (same dimensions as in Figure 4-32) that were deposited (a) without frame and waiting time, (b) without frame and with a waiting time t_w = 150 ms, (c) with a frame and without waiting time and (d) with frame and a waiting time t_w = 150 ms. As discussed before, the deposit without frame and waiting time is undefined, especially the outer lines. Introducing a waiting time leads to overall more defined boundaries, but the outer lines are still not separated. When comparing the deposits with frame and with or without waiting time, no discernible difference can be observed, presumably because writing the frame already introduces a waiting time of t_w ~ 200 ms when writing the horizontal lines of the frame, and the effect is not improved by the additional t_w = 150 ms.

Interestingly, when writing a frame, the outer line becomes thinner, despite being irradiated with the same electron dose and having the additional proximity effect contribution from the frame. It is speculated that the deposition of the nearby frame leads to depletion of the precursor concentration and therefore reduced deposition rate, which might be beneficial to obtain a defined line. The introduction of a waiting time, which is inherent when writing a frame as discussed before, also appears to have a minor positive effect, as more material is deposited in the periphery.

Best results. Figure 4-34a-d depicts the best results that were obtained after successive improvement of the deposition parameters, along with blowup micrographs from the horizontal lines. On the deposit in Figure 4-34a, a minimum FWHM of 12 nm was measured from an integrated line profile as depicted in Figure 4-34e, with a nominal pitch of 27.27 nm. The deposit is well-defined, that is the lines are continuous and complete, and exhibit only minimal cross-linking. Further downscaling and optimization resulted in the structure depicted in Figure 4-34b, on which a minimum FWHM of 8 nm was measured, with a nominal pitch of 23.58 nm. All lines are still discernible, however, they are more discontinuous and now exhibit more cross-linking. These interconnects appear to be mainly caused by the relatively rough substrate which forms after prolonged electron beam irradiation. As it can be seen at the isolated line from the elongated L in Figure 4-34c, the bright substrate irregularity causes a slight bending in the line. Another factor that limits further downscaling are known in-house vibrations with frequencies of ~ 50 Hz and amplitudes of ~ 20 nm, which are apparent in the blowup images. As the deposits were

97

written with 250 sweeps, these vibrations presumably cause a broadening of the structure during the writing process, as well as a jagged appearance during imaging.
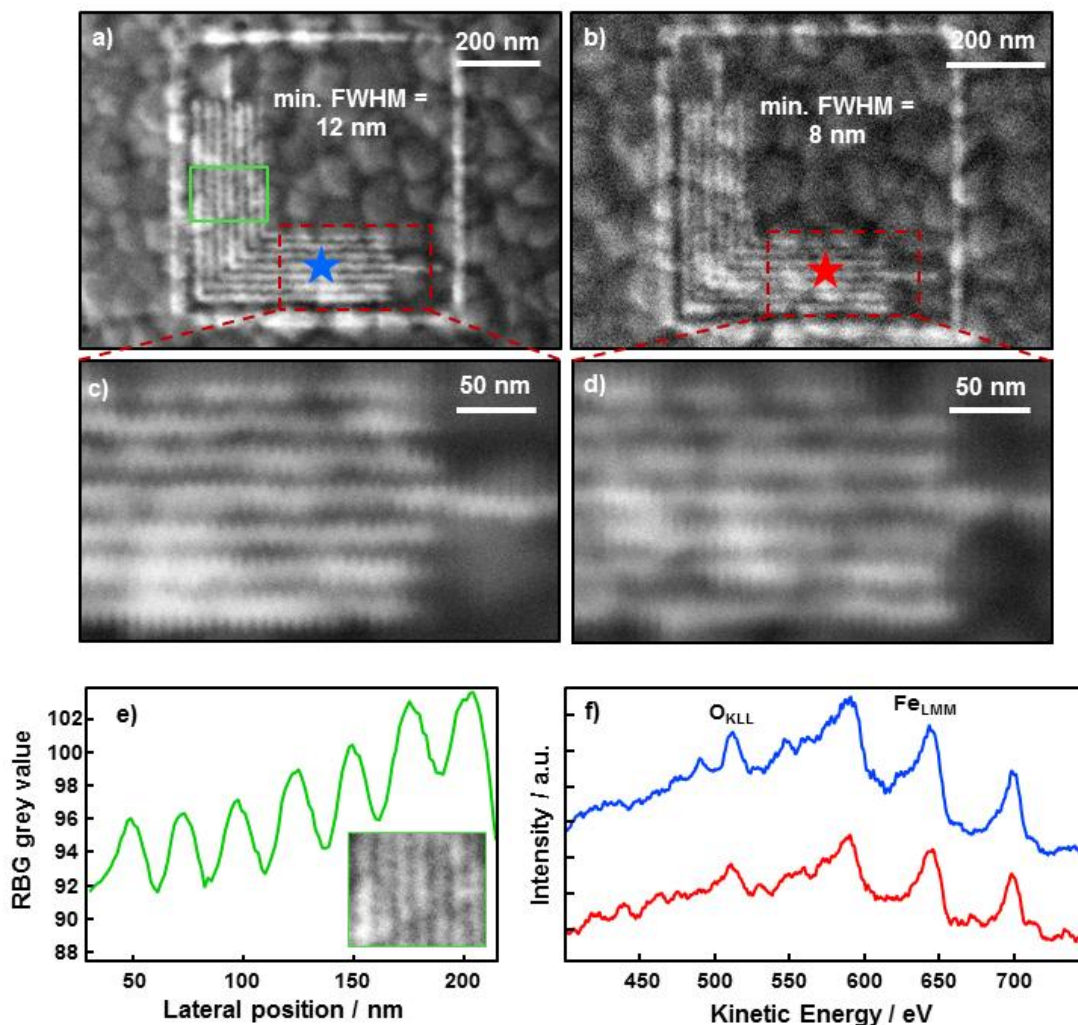
Figure 4-34: *Best results obtained in the presented experimental series. a) Fabricated with 2.4-36.5 µC/cm, 250 sweeps, t_{AG} = 21 min. A minimum FWHM of 12 nm was measured on an integrated line profile as exemplary depicted in e), with a pitch of 27.27 nm. b) Fabricated with 2.3-33.8 µC/cm, 250 sweeps, t_{AG} = 17 min. A minimum FWHM of 8 nm was measured, with a pitch of 23.58 nm. c), d) Blowup micrographs of the two structures, highlighting the increasing amount of interconnects between lines when decreasing the pitch, as well as the influence of in-house vibrations. f) Local AE spectra recorded at the positions indicated with the respectively coloured stars, proving that iron was deposited.*

Additionally, local AES (Figure 4-34f) at the positions indicated with stars was conducted. Signals of iron, oxygen and carbon (not shown) are observed, evidencing significant metal deposition. It has to be emphasized that the autocatalytic growth times of the depicted structures were only 18 and 21 min in order to minimize lateral broadening of the lines, and previous experiments have shown that at room temperature and the background pressure used, growth of crystalline iron does not take place at such relatively low autocatalytic growth times. Deposits directly fabricated by EBID have been demonstrated to consist of iron, carbon and oxygen [107] and can be regarded as seeds for the autocatalytic growth of pure iron crystallites. However, a quantitative statement concerning the elemental composition of the depicted line structures cannot be made, as potential carbon and oxygen signals from the deposit are indistinguishable from the signals originating from the SURMOF below. At this point it has to be emphasized that at the time when the experiments were conducted, the SEM emitter filament was degraded, and the maximum resolution of the employed 20 keV / 200 pA beam was at determined to ~ 6.5 nm (80 / 20 criterion on Au / C). Thus, the lowest obtained FWHM of 8 nm was only ~ 23 % larger than the measured resolution (which can be approximated as the beam spot size), indicating that proximity effects did only contribute to a very minor extent to the deposit width. This is regarded as a proof that one can indeed reduce proximity effects in FEBIP by using the low density HKUST-1 as a substrate.

To conclude, this chapter presented the results of a series of experiments that were performed with the aim of obtaining nested-L structures with minimal line pitch and FWHM. The influence of local and total electron dose, autocatalytic growth time, number of sweeps, co-deposition of a frame and waiting time between sweeps was presented and discussed, along with a justification for the use of certain parameters. Surprisingly, the deposition of a frame around the nested-L structure was a major step towards a well-defined deposit, as without frame, it was not possible to deposit the peripheral areas in a defined manner. The best results were presented, exhibiting a minimum FWHM of 12 nm at a nominal pitch of 27.27 nm, which are the smallest values achieved so far at the instrument. Local AES proved that iron was deposited. Further downscaling resulted in an increasing amount of interconnects between the lines due to the rough substrate that forms during electron irradiation. It was also shown that in-house vibrations cause significant broadening of the lines during imaging and likely also during deposition. As demonstrated by van Oven et al. [102], an effective countermeasure would be a phase synchronization of each sweep by

introducing according waiting times between individual sweeps. If these challenges can be overcome, SURMOFs in general appear to be very promising substrates to fabricate nanostructures by FEBIP. The minimum line FWHM of 8 nm only deviates by ~ 23 % from the measured minimum resolution (6.5 nm), which suggests that the main limiting factor for further downscaling is the beam spot size.

4.4 Local modification of Cu₂O/Cu(111) by FEBIP

4.4.1 Introduction

The fabrication of well-defined nanostructures can be realized either by top-down methods such as FEBIP, EBL and photolithography, or by a bottom-up approach, e.g. by the self-assembly of organic molecules into defined, supramolecular structures on surfaces. A major obstacle to implementing the bottom-up approach into the fabrication of e.g. microelectronic devices is the lack of positional control of the supramolecular assembly. Given the enormous complexity of these devices and the strict requirements in respect to the number of defects, a solution would be to control the position of individual atoms or molecules by top-down methods. This has already been demonstrated with an STM tip [108-110], but this method lacks the required throughput. This chapter presents the concept of a different approach: the use of FEBIP as a top-down method to fabricate templated, functionalized surfaces for the directed adsorption or anchoring of organic molecules, along with first results of an experimental implementation.

A general principle of surface functionalization is schematically depicted in Figure 4-35: A certain surface, e.g. a metal or semiconductor is pre-covered with a different material, e.g. a corresponding oxide. Organic molecules with certain functional groups, e.g. amine and imine groups of porphyrins, are evaporated on this surface and, depending on the interaction of the functional groups with the different substrates, adsorb preferentially on one of the materials. The adsorption behavior of porphyrin derivatives on a variety of defined surfaces has been extensively studied in the recent years [96, 111-113]. These molecules are regarded as ideal prototype building blocks for functional molecular architectures, as they combine a rigid framework, the porphin macrocycle, with a variety of possible moieties. This enables the modification of molecule-substrate and intermolecular interactions in a defined manner, e.g. by varying of the central metal ion or introducing linker groups in the periphery of the molecule.

Ditze et al. recently demonstrated that a Cu(111) surface pre-covered with sub-monolayer copper oxide acts as a model template for localized functionalization: 2HTPP preferentially adsorbs on bare Cu(111) due to the stronger molecule-substrate interaction, and cobalt tetraphenylporphyin (CoTPP) anchors at the edges of copper oxide islands [114].

The study is therefore a proof of principle that the adsorption site of 2HTPP can be controlled by exploiting the different adsorption behaviour of the molecule on different materials. However, the copper oxide islands in this case were prepared without spatial
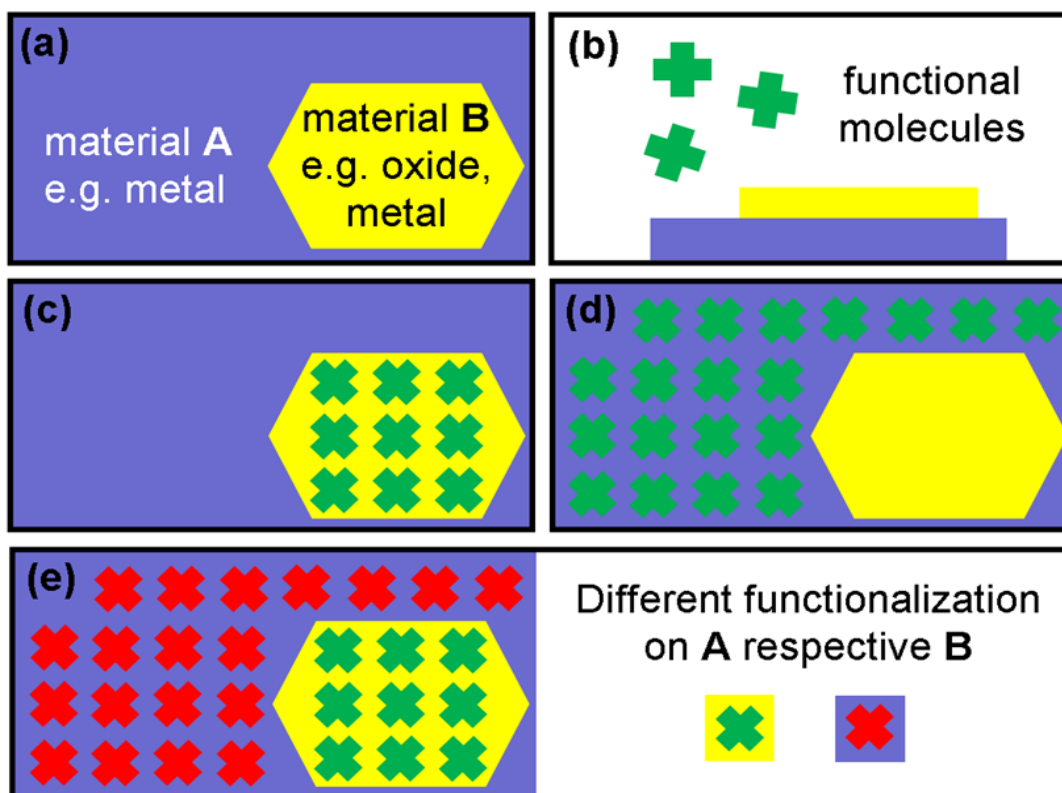

Figure 4-35: *Scheme of functionalizing a surface to direct the adsorption of molecules. a) A surface is pre-covered with a different material; b) functional molecules are evaporated and will preferentially be located on one of the materials (c-e). Adapted from ref. [114].*

control and are therefore randomly distributed on the copper substrate.

To gain precise control over the spatial arrangement of bare Cu(111) and copper oxide, the following concept was drafted, depicted in Figure 4-36. (1) A Cu(111) substrate is oxidized such that a copper oxide surface layer that covers the complete surface is formed. (2) The copper oxide layer is locally irradiated with a focused electron beam, with the aim of selectively removing it at irradiated sites. This step is based on the assumption that electron irradiation of copper oxide results in ESD of oxygen, which was observed for $SiO_x/Si(001)$ [8], $TiO_2(110)$ [9] and MgO/Ag(100) (not published), presumably based on the Knotek-Feibelman mechanism [57]. In an ideal scenario, removing the copper oxide layer would
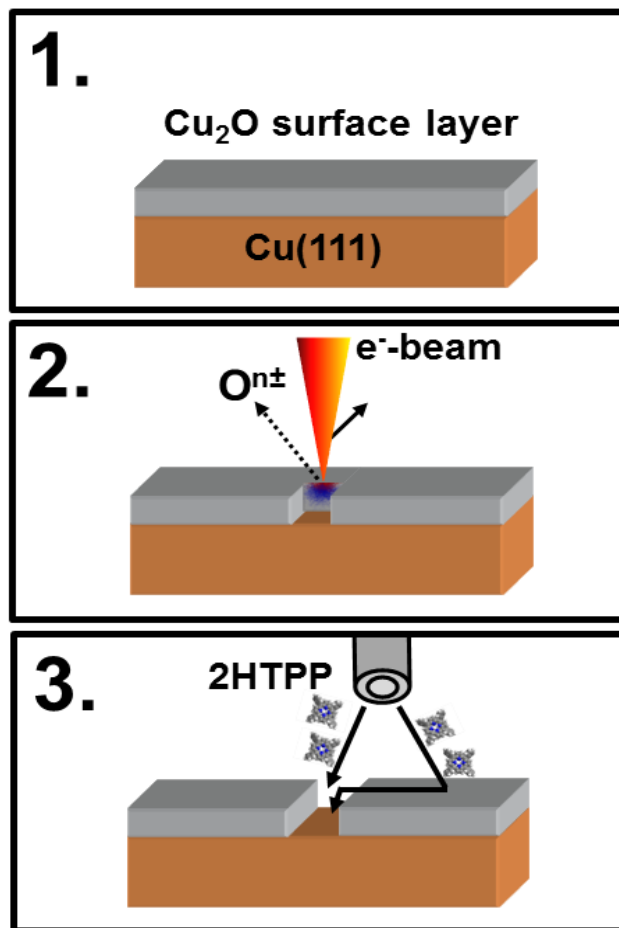
Figure 4-36: *Concept for the controlled fabrication of 2HTPP adsorption sites on Cu$_2$O/Cu(111) by FEBIP. The surface oxide layer is irradiated by the focused electron beam, thereby locally removing the oxide by ESD of oxygen, ideally exposing the Cu(111) surface. Subsequently supplied 2HTPP is then expected to be preferentially located on Cu(111) due to stronger molecule-substrate interactions.*

then expose the bare Cu(111) surface at irradiated sites. (3) When evaporating 2HTPP on this modified surface, the molecules would then preferentially be located on the exposed Cu(111). Ditze et al. have concluded that 2HTPP can sufficiently diffuse over the copper oxide layer, as the impingement of the molecules is assumed to be evenly distributed over the surface and is thus mainly taking place on the non-irradiated copper oxide layer [114].

The following chapter first describes the preparation of a copper oxide layer and its characterization by STM and LEED. The effect of electron beam irradiation of the copper oxide layer is investigated in detail by SEM, STM and AES.

4.4.2 Preparation of Cu₂O/Cu(111) and proof of principle

Starting off with a clean Cu(111) surface after repeated sputtering-annealing cycles (chapter 3.3.3), a copper oxide layer can be formed by exposing the surface to O_2. The crystal temperature during the exposure determines the type of oxide formed: at RT, a mostly disordered layer is formed after a sufficient O_2 dose, with only short-range, hexagonal order [115-119]. This layer was used in the study of Ditze et al. At higher temperatures during O_2 exposure, or upon annealing the disordered film, different long-range ordered copper oxide films can be obtained [118, 119].

Figure 4-37a depicts an ST micrograph, recorded after exposing a Cu(111) surface held at 423 K to 400 L O_2, with the corresponding LEED pattern depicted in Figure 4-37b, recorded with the sample at RT. Long-range ordered domains can be observed, with three different orientations (two orientations shown in the ST micrograph), corresponding to the threefold symmetry of the copper substrate below. Areas that are not covered by ordered domains appear noisy, which is attributed to mobile adsorbates on the pristine Cu(111) areas, i.e. these adsorbates are diffusing too fast to be imaged at RT. The rhomboid unit cell vectors of the copper oxide are 1.86 ± 0.07 nm and 0.97 ± 0.04 nm, enclosing an angle of 96°. This results in a unit cell area ~ 32 times larger than the Cu(111) 1×1 unit cell [120]. In literature, two types of possible reconstructions have been identified, depending on the
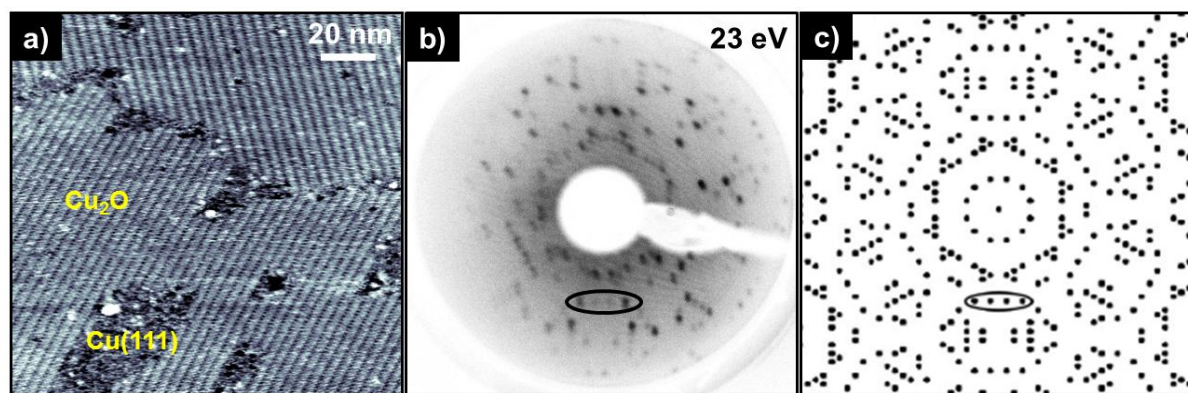
Figure 4-37: a) ST micrograph of a Cu₂O('29')/Cu(111) surface, noisy areas are assumed to be Cu(111) (U_{Bias} = 1.0 V, I = 30 pA); b) the corresponding LEED pattern; c) reciprocal lattice plot for the '29' superstructure, adapted from Matsumoto et al. [118]; the circle marks some reflexes in common with b).

crystal temperature during oxidation: the '29' and '44' superstructures, labeled by the size of their unit cells, which are 29 and 44 times larger than the Cu(111) 1×1 unit cell [118, 119, 121]. Both have a formal composition Cu_2O. Based on the measured unit cell size, the depicted copper oxide is therefore assumed to be the '29' superstructure. This is confirmed by the LEED pattern: Figure 4-37c depicts the reciprocal lattice plot for the '29' superstructure, adopted from Matsumoto et al. [118], which coincides with the measured LEED pattern depicted in Figure 4-37b, with only few spots missing or not discernable. This Cu_2O film is different from the disordered copper oxide film reported by Ditze et al.

Figure 4-38 depicts an ST micrograph and a corresponding blowup of this Cu_2O/Cu(111) surface after evaporation of 2HTPP. The porphyrin molecules appear as square/rectangular shaped protrusions, and can exclusively be observed in areas that are not covered by Cu_2O. It is therefore assumed that these areas are pristine Cu(111), and due to the strong molecule-substrate interaction between 2HTPP and Cu(111), diffusion away from these areas is inhibited. This strong interaction is based on the 'saddle-shape' conformation of 2HTPP, in which the porphyrin macrocycle is distorted such that the two
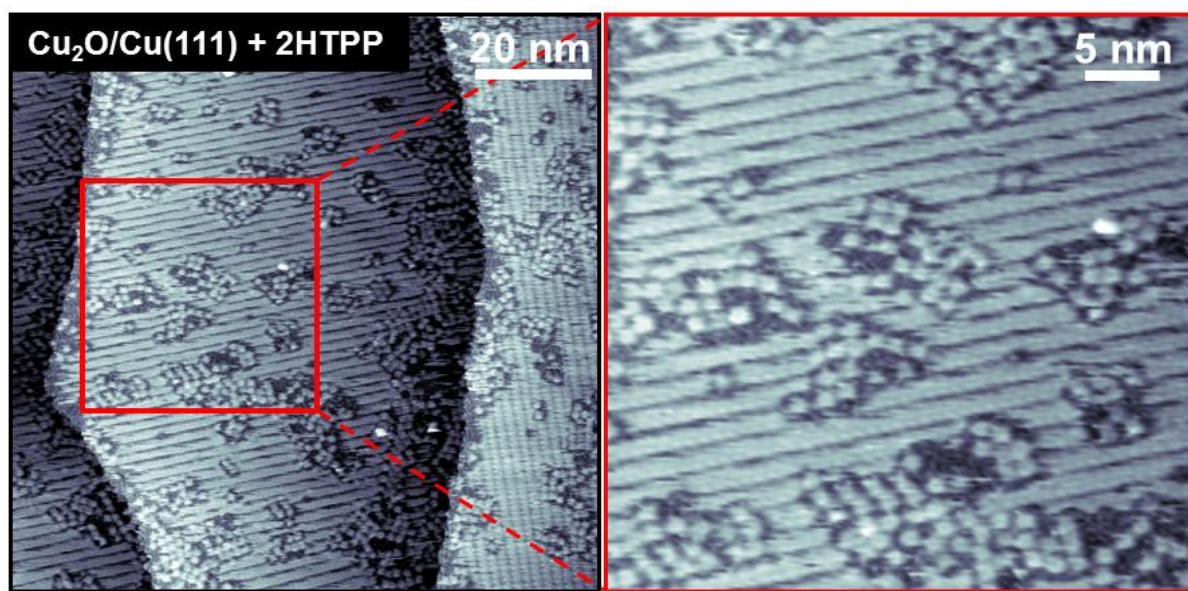

Figure 4-38: ST micrograph and a blowup of a Cu_2O('29')/Cu(111) surface after evaporation of 2HTPP. Individual molecules appear as square/rectangular protrusions only on what is assumed to be free lying Cu(111), due to the stronger molecule-substrate interactions compared to the oxide layer.

opposing iminic nitrogen atoms of the pyrroline rings point towards the surface, whereas the aminic nitrogen atoms of the pyrrol rings point away [111]. In the case of Cu(111), this conformation leads to a relatively strong bond between substrate and iminic nitrogen atoms and therefore low mobility at RT [122, 123]. It is assumed that at RT, the molecule-substrate interactions are stronger on Cu(111) than on Cu_2O. Therefore, 2HTPP molecules rapidly diffuse over the Cu_2O surface and become trapped on the pristine Cu(111). These findings are therefore in perfect agreement with the reports of Ditze et al. with disordered copper oxide on Cu(111).

4.4.3 Electron beam irradiation of Cu_2O('29')/Cu(111)

Next, the effects of irradiating the Cu_2O('29')/Cu(111) surface with a focused electron beam were investigated regarding microscopic changes (SEM, STM) and changes in elemental composition (AES), with the ultimate aim of locally removing the Cu_2O layer by electron beam irradiation.

Figure 4-39a depicts an SE micrograph of a Cu_2O('29')/Cu(111) surface after irradiating it with a dot matrix pattern with a focused 15 keV electron beam (beam diameter ~ 3 nm) and 80 pC per point (t_d = 0.2 s, I_{Beam} = 400 pA). The individual dots have diameters of several 10 nm and appear darker than the non-irradiated surface. Irregular, stripy features from top left to bottom right are attributed to substrate step edges. This pattern was then investigated with STM by navigating the tip over the irradiated matrix with SEM. An ST micrograph of the pattern is depicted in Figure 4-39b, with the same scale as in Figure 4-39a for direct comparison. Individual irradiated dots appear as bright protrusions. Note that step edges now run from bottom left to top right, as the scan direction in STM is rotated by 90° relative to the SEM scan direction. Figure 4-38c and d depict blowups with ~ 4 × 5 dots and a single dot, respectively. It is apparent that the individual dots consist of amorphous clusters with varying size, scattered around the electron beam impact point. It is assumed that in this case the topography dominates the appearance in STM, and that the clusters lie on top of the Cu_2O surface, which is still intact around the irradiated spot (stripy features on the surface in Figure 4-39d).

Local AES was then employed to obtain information concerning the elemental changes during electron beam irradiation. To do so, series of AE spectra were recorded while scanning the surface with decreasing scan areas, which allows following the AE peak areas as a function of the electron area dose. Figure 4-40 depicts a plot of the normalized O_{KLL}
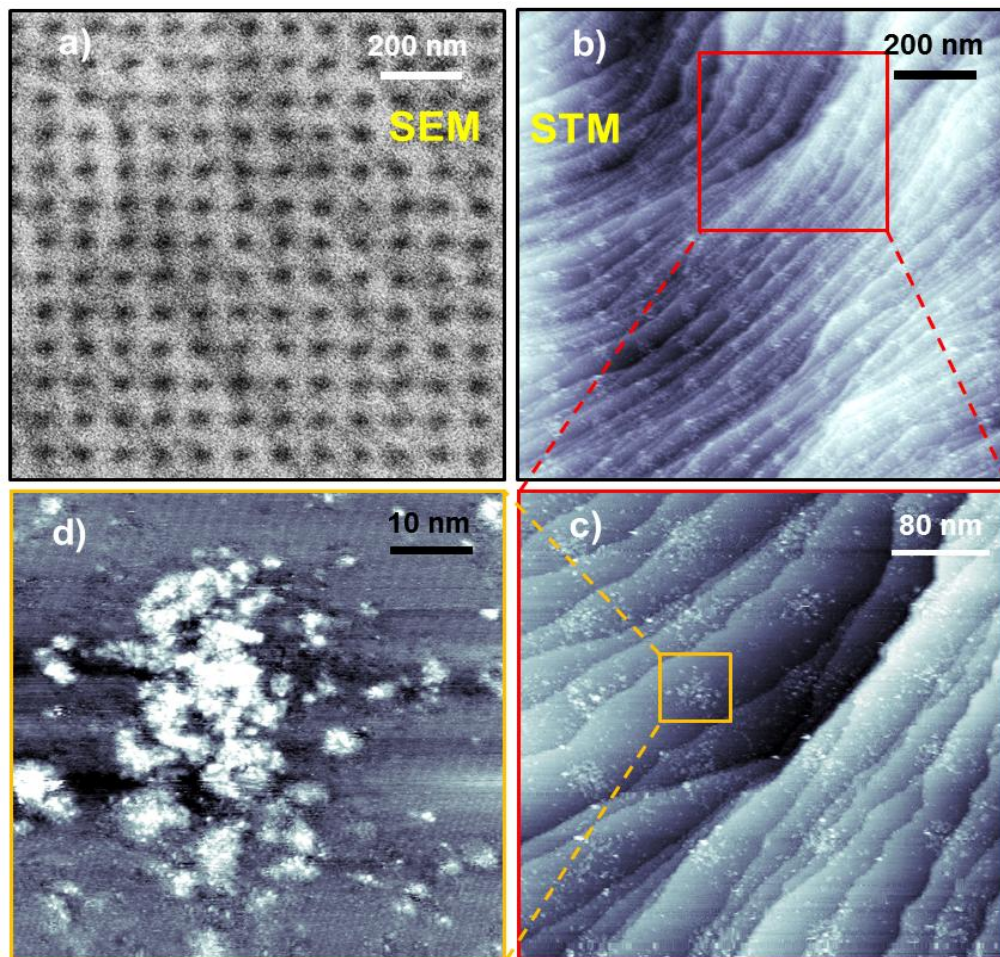
Figure 4-39: *a) SE micrograph of a Cu₂O('29')/Cu(111) surface after irradiating it with a matrix of single pixel points (15 keV, 80 pC/point); b) ST micrograph of the same pattern, with the same scale as in a); c,d) STM blowups of the pattern, showing that deposition of amorphous material occurred at irradiated spots.*

and C_{KLL} derivative peak heights (difference between highest and lowest slope in the first derivative spectrum) against the applied electron area dose along with a linear fit. It can be seen that the O_{KLL} intensity decreases, while the C_{KLL} intensity increases with increasing electron area dose.

These findings demonstrate that during the irradiation of the Cu_2O('29')/Cu(111) surface with a 15 keV focused electron beam, deposition of carbonaceous, amorphous material occurred. This deposition is probably due to the electron beam induced decomposition of surface-adsorbed hydrocarbon species. The decreasing oxygen signal intensity is therefore ascribed to an increased damping by the carbonaceous overlayer. This deposition process
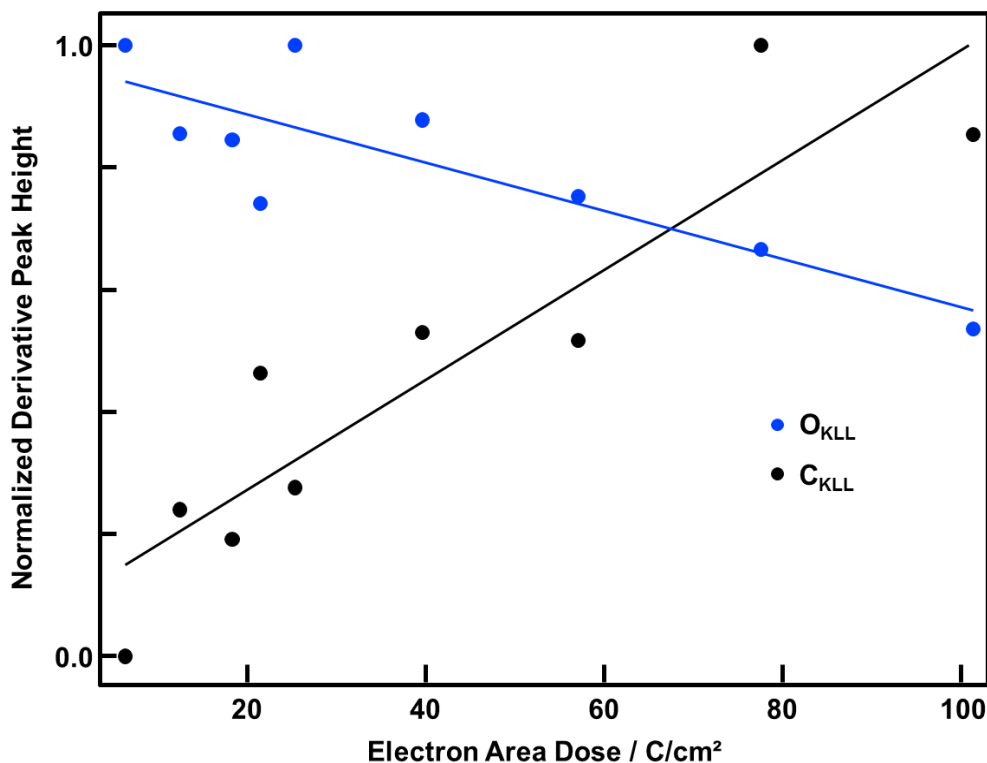
Figure 4-40: *Plot of the normalized derivative O_{KLL} and C_{KLL} peak heights, with a linear fit, against the applied electron area dose. The amount of deposited carbon increases with increasing electron area dose; the oxygen signal intensity is damped by the overlayer and therefore decreases with increasing electron dose.*

of amorphous material is obviously highly detrimental for the initial aim of removing the Cu_2O layer in a controlled way to fabricate adsorption sites for 2HTPP. On $TiO_2(110)$ and ultra-thin $SiO_x/Si(001)$, carbon deposition during electron beam irradiation was not observed, even for electron area doses of several magnitudes higher [8, 9]. Considering that these experiments were conducted in a UHV environment as well and presumably at a similar partial pressure of hydrocarbon species, it is speculated that the deposition of carbon on $Cu_2O('29')/Cu(111)$ occurs due to higher sticking coefficient, and therefore higher surface concentration of the hydrocarbon species compared to $TiO_2(110)$ and SiO_x.

To conclude, in this chapter a concept was presented to fabricate templated surfaces by FEBIP for the directed adsorption of organic molecules. It is based on the principle of locally removing or modifying a thin oxide layer with a focused electron beam, by ESD of oxygen, to create adsorption or anchoring sites. In first experiments, a '29' Cu_2O

superstructure on Cu(111) was fabricated, and this surface was irradiated with a dot matrix pattern. Investigating this pattern with STM revealed that amorphous material was deposited, and an AES study demonstrated that upon irradiation with higher electron area doses, carbon is deposited. As this makes the fabrication of defined adsorption/anchoring sites impossible, the system is considered unsuitable with the experimental conditions used during the irradiation. One possible way of preventing the carbon deposition could be to conduct the irradiation at different temperatures. A lower temperature might inhibit the diffusion of the hydrocarbon species, leading to a reduced deposition rate, and a higher temperature might lead to a higher desorption rate, therefore a lower hydrocarbon concentration and deposition rate.

5 Summary

The objective of this thesis was to further explore the research field of EBID and EBISA. In EBID, a focused electron beam is employed to dissociate surface-adsorbed precursor molecules, leaving a deposit at the beam impact point. In EBISA, a suitable surface is irradiated in the absence of a precursor, thereby the chemical composition of the surface is altered such that it becomes catalytically active towards decomposition of subsequently supplied precursor molecules, leading to deposit formation at pre-irradiated sites. In this work, the key challenges of these techniques, i.e. controlling the deposit composition and proximity effects, were addressed, and the EBID and EBISA techniques were expanded to new substrates and precursors. The focus of research was mostly on substrates consisting of organic materials, i.e. 2HTPP and SURMOFs. To mitigate the contribution of residual gas fragments to the deposit composition, FEBIP experiments and the corresponding characterization were carried out in a UHV environment. All deposits were fabricated and characterized using a UHV-compatible SEM with a beam diameter and therefore resolution < 3 nm, and local AES was performed to obtain spectromicroscopic information.

In this work, it was found that subtle differences in the surface structure (here 1×1 and 1×2 reconstructed $TiO_2(110)$) can lead to a severe difference in catalytic activity towards decomposition of a precursor. The catalytic activity can be completely inhibited by pre-covering the surface with 2-3 layer 2HTPP. EBISA is possible on the 2HTPP layer with $Co(CO)_3NO$ and $Fe(CO)_5$, considerably expanding the EBISA technique, as it is possible to use it on substrates which are otherwise not suitable, by pre-covering them with a thin layer of 2HTPP. It was further demonstrated that EBISA in combination with Monte-Carlo simulations is a powerful technique to assess basic scattering and surface activation parameters. It was demonstrated that EBID and EBISA is possible on SURMOFs, where unexpected precursor selectivities were discovered. Line FWHM down to 8 nm were achieved on HKUST-1, the lowest value achieved so far at the instrument.

FEBIP experiments revealed that rutile $TiO_2(110)$ 1×1 catalytically decomposes $Co(CO)_3NO$ at RT in UHV, leading to the formation of a closed overlayer following autocatalytic growth. Previous experiments have demonstrated that no spatially unselective decomposition occurs at RT when using $Fe(CO)_5$ as precursor on the same substrate. Interestingly, on the 1×2 reconstructed surface the situation is reversed: spatially selective

fabrication of nanostructures is possible with $Co(CO)_3NO$, whereas $Fe(CO)_5$ catalytically decomposes at 1×2 strands at RT. It was then demonstrated that by pre-covering $TiO_2(110)$ 1×1 with 2-3 layers of 2HTPP, the catalytic decomposition of $Co(CO)_3NO$ is inhibited. Using this substrate, spatially well-defined nanostructures were fabricated using either the EBID or EBISA protocol, with both $Co(CO)_3NO$ or $Fe(CO)_5$. Further experiments were conducted to expand this concept of surface passivation by demonstrating that 2-3 layers of 2HTPP also inhibit the catalytic decomposition of $Co(CO)_3NO$ on Si(111). Thus it was demonstrated for the first time that EBISA is possible with $Co(CO)_3NO$, as it has previously only been demonstrated with $Fe(CO)_5$ on SiO_x, $TiO_2(110)$ and 2HTPP layers, and with $Co_2(CO)_8$ on SiO_x. Besides inhibiting the catalytic activity, using thin 2HTPP layers, and presumably closed organic layers in general, also offers the interesting possibility of expanding EBISA to surfaces on which electron beam activation is not possible in the pristine state, such as Si(111).

A detailed analysis of the deposit composition of FEBIP structures fabricated on 2HTPP-covered substrates demonstrated that all structures contain significant amounts of carbon in the periphery, whereas the inner part is carbon-free. This difference in composition goes along with a distinct contrast of the corresponding areas in SEM. An extensive analysis of the influence of various lithographic parameters was conducted. To obtain a more conclusive picture of the corresponding processes that lead to the formation of these bi-compositional deposits, further studies are necessary.

Experiments were presented in which layered, bi-compositional deposits were fabricated on 2HTPP/$TiO_2(110)$, by alternate dosing of $Fe(CO)_5$ and $Co(CO)_3NO$ on an EBID deposit fabricated with $Co(CO)_3NO$. It was shown that $Fe(CO)_5$ decomposes only on the inner, carbon-free area of the initial deposit, and interestingly, in this second layer the periphery is carbon-rich as well, and the inner part carbon-free. The same phenomena are observed when exposing this deposit to $Co(CO)_3NO$, leading to the formation of a 'stepped pyramid' shaped deposit. A model was presented to explain the formation mechanism of the binary composition in the second layer and above.

A combined experimental and theoretical procedure was conducted to obtain quantitative information concerning the critical BSE densities required in EBISA to activate various surfaces for the decomposition of $Fe(CO)_5$. Experimentally obtained EBISA point deposit radii were evaluated on 2HTPP-covered $TiO_2(110)$, Si(111), Ag(111), as well as on pristine $TiO_2(110)$ and SiO_x/Si. MC simulations provided the absolute BSE densities at these radii, giving the minimum, critical BSE densities d_{CRIT} required to sufficiently activate these

surfaces for the decomposition of $Fe(CO)_5$. It was found that d_{CRIT} has the same magnitude for all 2HTPP covered substrates, it increases several magnitudes from $TiO_2(110)$ to SiO_x/Si to 2HTPP-covered substrates, and it decreases for increasing radii on $TiO_2(110)$ and SiO_x/Si. Attempts to explain these trends were presented, and it was concluded that in order to obtain more information concerning the activation processes, further data about the respective electron induced reaction cross sections, as well as the energy distribution of low energy electrons, is required.

A novel class of substrates, namely SURMOFs, was introduced to the field of FEBIP. SURMOFs are MOFs epitaxially grown on a surface in a highly controlled manner, and they exhibit interesting properties for the FEBIP process, e.g. high porosity, potentially enabling precursor diffusion through the bulk, and low density compared to standard bulk materials, possibly leading to a lower backscattering coefficient and consequently reduced proximity effects. The SURMOF substrates were were fabricated and provided by the group of Dr. H. Gliemann and Prof. C. Wöll (KIT). First FEBIP experiments on HKUST-1 and the porphyrin-based Zn-DPDCPP revealed that EBID is possible with $Fe(CO)_5$ and $Co(CO)_3NO$, whereas EBISA is only possible with $Fe(CO)_5$, but not with $Co(CO)_3NO$ on both SURMOFs. This finding further expands the EBISA technique to a new organic substrate, thus organic layers in general appear to be suitable for the corresponding activation. Another series of experiments was performed with the aim of fabricating line structures (nested-L) with a lowest possible line width and spacing, using EBID with $Fe(CO)_5$ on HKUST-1. The best results exhibit FWHM down to 8 nm, which is the smallest value reached so far with the instrument.

Lastly, a new concept was presented along with a first experimental implementation: the use of FEBIP as a top-down method to fabricate template surfaces for the spatially controlled adsorption or anchoring of organic molecules, such as porphyrin derivatives. The concept relies on the principle of locally removing or modifying a thin oxide layer, by ESD of oxygen, which was observed on different oxide surfaces. It was found that irradiation of a single-layer '29' Cu_2O superstructure on Cu(111) leads to deposition of carbonaceous material. It was concluded that, at least under the experimental conditions used, this substrate is not suitable for the approach. Further experiments might include varying the temperature during electron beam irradiation to inhibit diffusion of hydrocarbon species (low T) or increase their desorption rate (high T).

6 Zusammenfassung

Das Ziel dieser Arbeit war der Beitrag zu den Forschungsgebieten der elektronenstrahlinduzierten Abscheidung (Electron Beam Induced Deposition, EBID) und elektronenstrahlinduzierten Oberflächenaktivierung (Electron Beam Induced Surface Activation, EBISA). Beide und weitere Techniken werden auch unter dem Akronym FEBIP (Focused Electron Beam Induced Processing) zusammengefasst. In EBID wird ein hochfokussierter Elektronenstrahl eines Elektronenmikroskops verwendet um oberflächenadsorbierte Precursormoleküle zu zersetzen, was zur Bildung einer Abscheidung an der bestrahlten Stelle führt. In EBISA wird eine geeignete Oberfläche in Abwesenheit eines Precursors bestrahlt. Dabei wird die chemische Zusammensetzung so geändert, dass die bestrahlten Stellen katalytisch aktiv in Bezug auf die Zersetzung eines danach auf die Oberfläche dosierten Precursors werden. Diese Arbeit befasst sich zum einen mit den größten Herausforderungen der beiden Techniken: die Kontrolle über die chemische Zusammensetzung der Abscheidungen, sowie die sogenanten 'Proximity Effects', d.h. die Strukturweitung durch den Einfluss von Rückstreu- und Sekundärelektronen. Desweiteren werden beide Techniken auf neue Substrate und Precursorsubstanzen erweitert. Im Fokus lagen hier insbesondere die organischen Substrate: ultradünne Schichten (2-3 Lagen) 2HTPP (2H-Tetraphenylporphyrin) sowie SURMOFs (Surface-Anchored Metal-Organic Frameworks). Um den Einfluss von oberflächenadsorbierten Restgasmolekülen auf die chemische Zusammensetzung der Abscheidungen (z.B. unerwünschter Kohlenstoff durch die Zersetzung von Kohlenwasserstoffen) zu minimieren, wurden alle Experimente und Charakterisierungen in Ultrahochvakuum (UHV) durchgeführt. Alle Abscheidungen wurden mit einem UHV-kompatiblen Rasterelektronenmikroskop (REM) mit einem Strahldurchmesser, und dadurch einer Auflösung, von < 3 nm erstellt und charakterisiert. Lokale Augerelektronenspektroskopie wurde durchgeführt um spektro-mikroskopische Informationen zu erhalten.

Es wurde gezeigt, dass geringe Unterschiede in der Oberflächenstruktur (hier 1×1 und 1×2-rekonstruiertes $TiO_2(110)$) zu erheblichen Unterschieden in der katalytischen Aktivität bezüglich der Zersetzung eines Precursors führen. Die katalytische Aktivität wird durch 2-3 Lagen 2HTPP gehemmt. EBISA ist auf dieser 2HTPP-Schicht mit $Co(CO)_3NO$ und $Fe(CO)_5$ möglich, was die Technik erheblich erweitert, da es möglich ist EBISA auf Substraten

durchzuführen auf denen es in ihrer reinen Form nicht möglich ist, indem man sie mit 2HTPP beschichtet. Weiterhin wurde gezeigt dass mit EBISA, in Kombination mit Monte-Carlo Simulationen, grundlegende Streu- und Oberflächenaktivierungsparamter ermittelt werden können. Es wurde gezeigt dass EBID und EBISA auf SURMOFs möglich ist, wobei unerwartete Precursorselektivitäten beobachtet wurden. Linienstrukturen mit FWHM bis zu 8 nm wurden erreicht, was der niedrigste bisherige Wert an dem benutzten Instrument ist.

Es wurde gezeigt dass rutiles $TiO_2(110)$ 1×1, bei Raumtemperatur in UHV, $Co(CO)_3NO$ katalytisch zersetzt, was nach autokatalytischem Wachstum die Bildung einer geschlossenen Schicht auf der kompletten Oberfläche zur Folge hat. Frühere Experimente haben gezeigt dass auf dem selben Substrat keine solch unselektive Zersetzung mit $Fe(CO)_5$ stattfindet. Interessanterweise ist die Situation auf der 1×2-rekonstruierten Oberfläche umgekehrt: räumlich definierte Nanostrukturen können mit $Co(CO)_3NO$ erstellt werden, während sich $Fe(CO)_5$ an den 1×2-rekonstruierten Stellen zersetzt. Es konnte gezeigt werden dass eine dünne Schicht (2-3 Lagen) 2HTPP die katalytische Zersetzung von $Co(CO)_3NO$ auf $TiO_2(110)$ 1×1 verhindert. Auf dieser modifizierten Oberfläche können wiederum räumlich definierte Nanostrukturen erstellt werden, mit EBID und EBISA und sowohl $Co(CO)_3NO$ als auch $Fe(CO)_5$. Weitere Experimente wurden durchgeführt um dieses Konzept der Oberflächenpassivierung zu erweitern, und es wurde gezeigt dass 2-3 Lagen 2HTPP auch die katalytische Zersetzung von $Co(CO)_3NO$ auf Si(111) verhindern. Diese Experimente zeigten somit zum ersten Mal dass EBISA mit $Co(CO)_3NO$ möglich ist, da es bisher nur mit $Fe(CO)_5$ auf SiO_x, $TiO_2(110)$ und 2HTPP-Lagen, und mit $Co_2(CO)_8$ auf SiO_x gezeigt wurde. Neben dem Verhindern der katalytischen Zersetzung ermöglicht das Verwenden von 2HTPP-Lagen, und womöglich dünnen organischen Schichten generell, EBISA auf Oberflächen durchzuführen, auf denen es in ihrem reinen Zustand nicht möglich ist, z.B. Si(111).

Eine detaillierte Analyse der Zusammensetzung der Abscheidungen auf 2HTPP-Lagen zeigte dass alle Abscheidungen einen erheblichen Kohlenstoffanteil in der Peripherie der Struktur aufweisen, während der innere Teil durchweg frei von Kohlenstoff ist. Dieser Unterschied geht einher mit einem ausgeprägten REM-Kontrast zwischen den beiden Bereichen. Eine Analyse des Einflusses der verschiedenen lithographischen Parameter auf diesen Unterschied wurde durchgeführt. Um ein schlüssiges Bild der jeweiligen Prozesse die zur Entstehung dieser binären Zusammensetzung zu bekommen sind allerdings weitere Untersuchungen nötig.

Ein Experiment wurde präsentiert in dem geschichtete Abscheidungen auf 2HTPP/TiO$_2$(110) erstellt wurden durch abwechselndes Dosieren von Fe(CO)$_5$ und Co(CO)$_3$NO auf eine EBID-Abscheidung die wiederum mit Co(CO)$_3$NO angefertigt wurde. Es konnte gezeigt werden dass sich Fe(CO)$_5$ nur auf dem inneren, kohlenstofffreien Bereich katalytisch zersetzt (und autokatalytisch wächst), und interessanterweise weist die dadurch gebildete zweite Lage ebenfalls einen hohen Kohlenstoffanteil in der Peripherie auf, während der innere Bereich kohlenstofffrei ist. Das gleiche Phänomen wird beobachtet, wenn auf diese zweite Lage wiederum Co(CO)$_3$NO dosiert wird, was zur Bildung einer Abscheidung in Form einer Stufenpyramide führt. Es wurde ein Modell präsentiert, welches einen Erklärungsansatz für die Ausbildung der binären Zusammensetzung ab der zweiten Lage liefert.

Eine kombinierte theoretische und experimentelle Methode wurde gezeigt, um quantitative Informationen über die kritische Rückstreuelektronendichten (d$_{CRIT}$) zu erhalten, die in EBISA benötigt werden um verschiedene Oberflächen für die katalytische Zersetzung von Fe(CO)$_5$ zu aktivieren. Hierzu wurden zunächst Radien von EBISA-Punktabscheidungen auf 2HTPP-beschichtetem TiO$_2$(110), Si(111), Ag(111), sowie auf reinem TiO$_2$(110) und SiO$_x$/Si ermittelt. Monte-Carlo (MC) Simulationen, lieferten die absoluten Rückstreuelektronendichten an den jeweiligen Radien. Diese Rückstreuelektronendichten sind die minimalen, kritischen Dichten d$_{CRIT}$, welche benötigt werden um die Oberfläche für die Zersetzung von Fe(CO)$_5$ zu aktivieren. Es wurde herausgefunden dass d$_{CRIT}$ für alle 2HTPP-beschichteten Substrate relativ gleich ist, dass sie um mehrere Größenordnungen von TiO$_2$(110) über SiO$_x$/Si zu 2HTPP-beschichteten Substraten steigt, und dass sie auf TiO$_2$(110) und SiO$_x$/Si für steigende Radien abnimmt. Es wurden Erklärungsansätze für diese Trends vorgelegt, und es wurde gefolgert dass für weitere Rückschlüsse weitere Daten über die Wirkungsquerschnitte der entsprechenden elektroneninduzierten Reaktionen sowie die Energieverteilung der niederenergetischen Elektronen nötig sind.

In Kapitel 4.3 wurde eine neuartige Klasse von Substraten in das FEBIP Forschungsgebiet eingeführt: SURMOFs. SURMOFs sind MOFs (Metal-Organic Frameworks), welche durch kontrolliertes, epitaktisches Wachstum auf eine Oberfläche aufgebracht werden. Sie weisen für FEBIP-Prozesse interessante Eigenschaften auf: ausgeprägte Porosität, was potentiell die Diffusion von Precursormolekülen durch das Substrat ermöglicht, und eine niedrige Dichte verglichen mit Standartsubstraten, was potentiell zu niedrigeren Rückstreukoeffizienten und damit verringerten Proximity-Effekten

führt. Die Proben wurden von der Gruppe von Dr. H. Gliemann und Prof. C. Wöll (KIT) geliefert. Erste FEBIP-Experimente auf HKUST-1 und dem porphyrin-basierten Zn-DPDCPP zeigten, dass EBID mit $Fe(CO)_5$ und $Co(CO)_3NO$ auf beiden SURMOFs möglich ist, wohingegen EBISA mit $Fe(CO)_5$, aber nicht mit $Co(CO)_3NO$ auf beiden Substraten möglich ist. Dieser Befund erweitert die EBISA-Technik auf ein weiteres organisches Substrat, was darauf hinweist dass organische Schichten wohl generell empfänglich für die entsprechende Oberflächenaktivierung sind. Weitere EBID-Experimente wurden mit $Fe(CO)_5$ auf HKUST-1 durchgeführt, mit dem Ziel, Linienstrukturen mit einer geringstmöglichen Linienbreite und – dichte zu erstellen. In den besten Ergebnissen wurde ein FWHM (Full width at half maximum) der Linien bis zu 8 nm erreicht, was der geringste Wert ist, der bis dahin mit dem Instrument erreicht wurde.

Desweiteren wurde ein neues Konzept sowie erste dazugehörige Experimente präsentiert. Eine geeignete Oberfläche wird mit einem fokussierten Elektronenstrahl bestrahlt, um gezielt Adsorptionsstellen für organische Moleküle, z.B. Porphyrine, zu erstellen. Das Konzept basiert auf dem Prinzip lokal eine dünne Oxidschicht zu modifizieren oder zu entfernen, ermöglicht durch elektroneninduzierte Desorption von Sauerstoff, welche bereits auf verschiedenen Oxiden gezeigt wurde. Es wurde gezeigt dass die Bestrahlung einer dünnen '29' Cu_2O-Superstruktur auf Cu(111) zur Abscheidung von Kohlenstoff führt. Es wurde gefolgert dass, zumindest unter den verwendeten experimentellen Bedingungen, dieses Substrat nicht geeignet ist. Weitere Experimente könnten eine Variation der Temperatur während der Bestrahlung beinhalten, z.B. um die Diffusion von Kohlenwasserstoffen zu hemmen (niedrige Temperatur) oder ihre Desorptionsrate zu erhöhen (hohe Temperatur).

7 References

1. M. Harris, "Inside Pascal: NVIDIA's Newest Computing Platform", Tesla P100 GPU specifications, *https://devblogs.nvidia.com/parallelforall/inside-pascal/*, retrieved 06.04.2017.

2. C. Vieu, F. Carcenac, A. Pépin, Y. Chen, M. Mejias, A. Lebib, L. Manin-Ferlazzo, L. Couraud and H. Launois, Applied Surface Science, 2000, **164**, 111.

3. Y. D. Chan, Proc. of SPIE, 2011, **8166**.

4. Y. Chen, Microelectronic Engineering, 2015, **135**, 57.

5. I. Utke, P. Hoffmann and J. Melngailis, Journal of Vacuum Science & Technology B, 2008, **26**, 1197.

6. W. F. van Dorp and C. W. Hagen, J. Appl. Phys., 2008, **104**, 081301.

7. M.-M. Walz, M. Schirmer, F. Vollnhals, T. Lukasczyk, H.-P. Steinrück and H. Marbach, Angew. Chem. Int. Ed., 2010, **49**, 4669.

8. M.-M. Walz, F. Vollnhals, M. Schirmer, H.-P. Steinrück and H. Marbach, Physical Chemistry Chemical Physics, 2011, **13**, 17333.

9. F. Vollnhals, T. Woolcot, M.-M. Walz, S. Seiler, H.-P. Steinrück, G. Thornton and H. Marbach, The Journal of Physical Chemistry C, 2013, **117**, 17674.

10. F. Vollnhals, P. Wintrich, M.-M. Walz, H.-P. Steinrück and H. Marbach, Langmuir, 2013, **29**, 12290.

11. F. Tu, M. Drost, F. Vollnhals, A. Späth, E. Carrasco, R. H. Fink and H. Marbach, Nanotechnology, 2016, **27**, 355302.

12. J. M. De Teresa and A. Fernández-Pacheco, Applied Physics A - Materials Science & Processing, 2014, **117**, 1645.

13. J. M. De Teresa, A. Fernández-Pacheco, R. Córdoba, L. Serrano-Ramón, S. Sangiao and M. R. Ibarra, Journal of Physics D: Applied Physics, 2016, **49**, 243003.

14. A. Fernández-Pacheco, J. M. De Teresa, R. Córdoba and M. R. Ibarra, Journal of Physics D: Applied Physics, 2009, **42**, 055005.

15. L. Reimer, Scannig Electron Microscopy, Springer-Verlag Berlin Heidelberg, 1985.

16. R. F. Egerton, Physical Principles of Electron Microscopy, Springer Science+Business Media, Inc., 2005.

17. Product information: ZEISS GeminiSEM Family, Carl Zeiss Microscopy GmbH, retrieved 04.10.2016.

18. Product information: Advances in SEM and Microanalysis - JEOL's Ultrahigh Resolution Analytical FE SEM and Soft X-ray WDS, JEOL USA, retrieved 05.10.2016.

19. J. F. Watts and J. Wolstenholme, An Introduction to Surface Analysis by XPS and AES, Wiley-VCH Verlag GmbH, 2003.

20. M. Barthés-Labrousse, Microscopy Microanalysis Microstructures, 1995, **6**, 253.

21. D. F. Stein and A. Joshi, Annual Review of Materials Research, 1981, **11**, 485.

22. J. C. Lascovich, R. Giorgi and S. Scaglione, Appplied Surface Science, 1991, **47**, 17.

23. W. Göpel, Surface Science, 1984, **139**, 333.

24. P. H. Dawson, Quadrupole Mass Spectrometry and its applications, Elsevier Scientific Publishing Company, 1976.

25. L. J. Clarke, Surface Crystallography: An Introduction to Low Energy Electron Diffraction, John Wiley & Sons Ltd., 1985.

26. P. Sutter, Science of Microscopy, Springer Science+Business Media, LLC, 2007.

27. C. J. Chen, Introduction to Scanning Tunneling Microscopy, Oxford University Press, New York, 1993.

28. M. P. Nikiforov and D. A. Bonnell, Science of Microscopy, Springer Science+Business Media, LLC, 2007.

29. R. L. Stewart, Physical Review, 1934, **45**, 488.

30. R. W. Christy, J. Appl. Phys., 1960, **31**, 1680.

31. A. G. Baker and W. C. Morris, Review of Scientific Instruments, 1961, **32**, 458.

32. S. J. Randolph, J. D. Fowlkes and P. D. Rack, Crit. Rev. Solid State Mater. Sci., 2006, **31**, 55.

33. N. Silvis-Cividjian, C. W. Hagen and P. Kruit, J. Appl. Phys., 2005, **98**, 084905.

34. M. Song and F. Kazuo, Science and Technology of Advanced Materials, 2008, **9**, 023002.

35. W. F. Van Dorp, C. W. Hagen, P. A. Crozier and P. Kruit, Nanotechnology, 2008, **19**, 1.

36. K. Murakami, F. Wakaya and M. Takai, Journal of Vacuum Science & Technology B, 2007, **25**, 1310.

37. Y. Tsukatani, N. Yamasaki, K. Murakami, F. Wakaya and M. Takai, Japanese Journal of Applied Physics, 2005, **44**, 5683.

38. I. Utke, P. Hoffmann, R. Berger and L. Scandella, Applied Physics Letters, 2002, **80**, 4792.

39. D. N. Madsen, K. Mølhave, R. Mateiu, A. M. Rasmussen, M. Brorson, C. J. H. Jacobsen and P. Bøgghild, Nanoletters, 2002, **3**, 47.

40. H. W. P. Koops, E. Munro, J. Rouse, J. Kretz, M. Rudolph, M. Weber and G. Dahm, Nuclear Instruments and Methods in Physics Research A, 1995, **363**, 1.

41. K. Edinger, H. Becht, J. Bihr, V. Boegli, M. Budach, T. Hofmann, H. W. P. Koops, P. Kuschnerus, J. Oster, P. Spies and B. Weyrauch, Journal of Vacuum Science and Technology B, 2004, **22**, 2902.

42. T. Bret, R. Jonckheere, D. Van den Heuvel, C. Baur, M. Waiblinger and G. Baralia, Proceedings of SPIE, 2012, **8322**, 83220C.

43. M. Weber, H. W. P. Koops, M. Rudolph, J. Kretz and G. Schmidt, Journal of Vacuum Science & Technology B, 1995, **13**, 1364.

44. I. Utke, T. Bret, D. Laub, P. Buffat, L. Scandella and P. Hoffmann, 2003, **73-74**, 553.

45. T. Lukasczyk, M. Schirmer, H.-P. Steinrück and H. Marbach, Small, 2008, **4**, 841.

46. A. Botman, J. J. L. Mulders and C. W. Hagen, Nanotechnology, 2009, **20**, 1.

47. D. Belić, M. M. Shawrav, M. Gavagnin, M. Stöger-Pollach, H. D. Wanzenboeck and E. Bertagnolli, ACS Applied Materials & Interfaces, 2014, **7**, 2467.

48. E. Begun, O. V. Dobrovolskiy, M. Kompaniiets, R. Sachser, C. Gspan, H. Plank and M. Huth, Nanotechnology, 2015, **26**, 075301.

49. B. B. Lewis, M. G. Stanford, J. D. Fowlkes, K. Lester, H. Plank and P. D. Rack, Beilstein Journal of Nanotechnology, 2015, **6**, 907.

50. A. Szkudlarek, A. R. Vaz, Y. Zhang, A. Rudkowski, C. Kapusta, R. Erni, S. Moshkalev and I. Utke, Beilstein Journal of Nanotechnology, 2015, **6**, 1508.

51. M. G. Stanford, B. B. Lewis, J. H. Noh, J. D. Fowlkes and P. D. Rack, ACS Applied Materials & Interfaces, 2015, **7**, 19579.

52. E. Villamor, F. Casanova, P. H. F. Trompenaars and J. J. L. Mulders, Nanotechnology, 2015, **26**, 095303.

53. E. Böhler, J. Warneke and P. Swiderek, Chemical Society Reviews, 2013, **42**, 9219.

54. C. R. Arumainayagam, H.-L. Lee, R. B. Nelson, D. R. Haines and R. P. Gunawardane, Surface Science Reports, 2010, **65**, 1.

55. J. D. Fowlkes, R. Winkler, B. B. Lewis, M. G. Stanford, H. Plank and P. D. Rack, ACS Nano, 2016, **10**, 6163.

56. H. Marbach, Applied Physics A 2014, **117**, 987.

57. M. L. Knotek and P. J. Feibelman, Physical Review Letters, 1978, **40**, 964.

58. K. Muthukumar, H. O. Jeschke, R. Valenti, E. Begun, J. Schwenk, F. Porrati and M. Huth, Beilstein Journal of Nanotechnology, 2012, **3**, 546.

59. E. Balaur, T. Djenizian, R. Boukherroub, J. N. Chazalviel, F. Ozanam and P. Schmuki, Electrochemistry Communications 2003, **6**, 153.

60. J. Huang, M. Lee and J. Kim, Journal of Vacuum Science & Technology A, 2012, **30**, 01A1281.

61. M.-M. Walz, F. Vollnhals, F. Rietzler, M. Schirmer, A. Kunzmann, H.-P. Steinrück and H. Marbach, Journal of Physics D: Applied Physics, 2012, **45**, 1.

62. M.-M. Walz, F. Vollnhals, F. Rietzler, M. Schirmer, H.-P. Steinrück and H. Marbach, Applied Physics Letters, 2012, **100**, 053118.

63. G. Wedler, Lehrbuch der Physikalischen Chemie, Wiley-VCH Verlag GmbH, 2004.

64. R. R. Kunz, T. E. Allen and T. M. Mayer, Journal of Vacuum Science & Technology B, 1987, **5**, 1427.

65. R. R. Kunz and T. M. Mayer, Applied Physics Letters, 1987, **50**, 962.

66. R. R. Kunz and T. M. Mayer, Journal of Vacuum Science & Technology B, 1988, **6**, 1557.

67. F. Zaera, Surface Science 1990, **255**, 280.

68. T. Lukasczyk, M. Schirmer, H.-P. Steinrück and H. Marbach, Langmuir, 2009, **25**, 11930.

69. F. Vollnhals, M. Drost, F. Tu, E. Carrasco, A. Späth, R. Fink, H.-P. Steinrück and H. Marbach, Beilstein Journal of Nanotechnology, 2014, **5**, 1175.

70. T. Lukasczyk, PhD Thesis, FAU Erlangen-Nürnberg, 2010.

71. M. Schirmer, PhD Thesis, FAU Erlangen-Nürnberg, 2012.

72. F. Vollnhals, PhD Thesis, FAU Erlangen-Nürnberg, 2014.

73. J. Ackermann, Handbuch SUPRA(VP) und ULTRA, 2004.

74. V. Friedli and I. Utke, Journal of Physics D: Applied Physics, 2009, **42**, 125305.

75. U. Diebold, Surface Science Reports, 2002, **48**, 53.

76. H. Gliemann and C. Wöll, Materials Today, 2012, **15**, 111.

77. S. Kitagawa, R. Kitaura and S. Noro, Angew. Chem. Int. Ed., 2004, **43**, 2334.

78. J. L. C. Rowsell and O. M. Yaghi, Microporous And Mesoporous Materials, 2004, **73**, 3.

79. X.-S. Wang, S. Ma, P. M. Forster, D. Yuan, J. Eckert, J. J. López, B. J. Murphy, J. B. Parise and H.-C. Zhou, Angew. Chem. Int. Ed., 2008, **47**, 7263.

80. U. Mueller, M. Schubert, F. Teich, H. Puetter, K. Schierle-Arndt and J. Pastré, Journal of Materials Chemistry, 2005, **16**, 626.

81. H. Furukawa, N. Ko, Y. B. Go, N. Aratani, S. B. Choi, E. Choi, A. Ö. Yazaydin, R. Q. Snurr, M. O'Keeffe, J. Kim and O. M. Yaghi, Science, 2010, **329**, 424.

82. A. U. Czaja, N. Trukhan and U. Müller, Chemical Society Reviews, 2009, **38**, 1284.

83. O. Shekhah, H. Wang, D. Zacher, R. A. Fischer and C. Wöll, Angew. Chem. Int. Ed., 2009, **48**, 5038.

84. S. Bundschuh, O. Kraft, H. Arslan, H. Gliemann, P. Weidler and C. Wöll, Applied Physics Letters, 2012, **101**, 1019101.

85. W. Zhou, PhD Thesis, Karlsruher Institut für Technologie, 2016.

86. S. S.-Y. Chui, S. M.-F. Lo, J. P. H. Charmant, A. Guy Orpen and I. D. Williams, Science, 1999, **283**, 1148.

87. R. A. Bennett, P. Stone, N. J. Price and M. Bowker, Physical Review Letters, 1999, **82**, 3831.

88. S. Takakusagi, K. Fukui, F. Nariyuki and Y. Iwasawa, Surface Science, 2003, **523**, L41.

89. G. C. Gazzadi, H. Mulders, P. Trompenaars, A. Ghirri, M. Affronte, V. Grillo and S. Frabboni, The Journal of Physical Chemistry C, 2011, **115**, 19606.

90. G. C. Gazzadi, J. J. L. Mulders, P. Trompenaars, A. Ghirri, A. Rota, M. Affronte and S. Frabboni, Microelectronic Engineering, 2011, **88**, 1955.

91. D. Madarász, G. Pótári, A. Sápi, B. László, C. Csudai, A. Oszkó, À. Kukovecz, A. Erdőhelyi, Z. Kónya and J. Kiss, Physical Chemistry Chemical Physics, 2013, **15**, 15917.

92. S. G. Rosenberg, M. Barclay and D. H. Fairbrother, The Journal of Physical Chemistry C, 2013, **117**, 16053.

93. A. Turchanin, D. Käfer, M. El-Desawy, C. Wöll, G. Witte and A. Gölzhäuser, Langmuir, 2009, **25**, 7342.

94. W. Geyer, V. Stadler, W. Eck, M. Zharnikov, A. Gölzhäuser and M. Grunze, Applied Physics Letters, 1999, **75**, 2401.

95. L. Sanche, Nuclear Instruments and Methods in Physics Research B, 2003, **208**, 4.

96. J. V. Barth, G. Costantini and K. Kern, Nature, 2005, **437**, 671.

97. D. Bonifazi, A. Kiebele, M. Stöhr, F. Cheng, T. Jung, F. Diederich and H. Spillmann, Advanced Functional Materials, 2007, **17**, 1051.

98. J. A. A. W. Elemans, S. Lei and S. De Feyter, Angew. Chem. Int. Ed., 2009, **48**, 7298.

99. F. Salvat, J. M. Fernández-Varea and J. Sempau, OECD/NEA Data Bank, Issy-les-Molineaux, France, 2011.

100. X. Llovet, C. J. Powell, F. Salvat and A. Jablonski, Journal of Physical and Chemical Reference Data, 2014, **43**, 013102.

101. J. Zhuan, J. Friedel and A. Terfort, Beilstein Journal of Nanotechnology, 2012, **2**, 570.

102. J. C. van Oven, F. Berwald, K. K. Berggren, P. Kruit and C. W. Hagen, Journal of Vacuum Science & Technology B, 2011, **29**, 06F305.

103. J. Yang and K. K. Berggren, J. Vac. Sci. Technol. B, 2007, **25**, 2025.

104. H. Duan, D. Winston, J. Yang, B. Cord, V. Manfrinato and K. K. Berggren, J. Vac. Sci. Technol. B, 2010, **28**, C6C58.

105. C. Xie, X. Zhu, H. Li, L. Shi, Y. Hua and M. Liu, Optics Letters, 2012, **37**, 749.

106. F. Rietzler, Diploma Thesis, FAU Erlangen-Nürnberg, 2011.

107. G. Hochleitner, H. D. Wanzenboeck and B. E., Journal of Vacuum Science & Technology B, 2008, **26**, 939.

108. D. M. Eigler and E. K. Schweizer, Nature, 1990, **344**, 524.

109. G. V. Nazin, X. H. Qiu and W. Ho, Science, 2003, **302**, 77.

110. M. Fuechsle, J. A. Miwa, S. Mahapatra, H. Ryu, S. Lee, O. Warschkow, L. C. L. Hollenberg, G. Klimeck and M. Y. Simmons, Nature Nanotechnology, 2012, **7**, 242.

111. H. Marbach and H.-P. Steinrück, Chem. Commun., 2014, **50**, 9034.

112. J. M. Gottfried, Surface Science Reports, 2015, **70**, 259.

113. F. Klappenberger, Progress in Surface Science, 2014, **89**, 1.

114. S. Ditze, M. Röckert, F. Buchner, E. Zillner, M. Stark, H.-P. Steinrück and H. Marbach, Nanotechnology, 2013, **24**, 115305.

115. L. McDonnell and D. Woodruff, Surface Science, 1974, **46**, 505.

116. G. Ertl, Surface Science, 1966, **6**, 208.

117. F. Habraken, E. Kieffer and G. Bootsma, Surface Science, 1978, **83**, 45.

118. T. Matsumoto, R. A. Bennett, P. Stone, T. Yamada, K. Domen and M. Bowker, Surface Science, 2000, **471**, 225.

119. F. Wiame, V. Maurice and P. Marcus, Surface Science, 2006, **601**, 1193.

120. M. Franke, Master Thesis, FAU Erlangen-Nürnberg, 2013.

121. F. Jensen, F. Besenbacher, E. Lægsgaard and I. Stensgaard, Surface Science Letters, 1991, **259**, L774.
122. F. Buchner, E. Zillner, M. Röckert, S. Gläßel, H.-P. Steinrück and H. Marbach, Chem. Eur. J., 2011, **17**, 10226.
123. F. Buchner, J. Xiao, E. Zillner, M. Chen, M. Röckert, S. Ditze, M. Stark, H.-P. Steinrück, J. M. Gottfried and H. Marbach, J. Phys. Chem. C, 2011, **115**, 24172.

8 Acknowledgements

At this point I want to acknowledge all people who contributed to this thesis.

I am grateful to Prof. Hans-Peter Steinrück for giving me the opportunity to work at the chair of PC II, and for all discussions regarding the topics of this thesis. I want to thank PD Hubertus Marbach for supervising my thesis and for all the constructive and helpful input regarding practical and theoretical aspects of this work.

I want to thank Prof. Jörg Libuda for the second assessment.

Special thanks goes to all current and former EBID team members: Fan Tu, Christian Preischl and Dr. Florian Vollnhals, for the very nice working atmosphere and for all the help with my experiments. I also acknowledge the contributions of Luisa Berger and Dr. Matthias Franke in the framework of their Master theses.

Furthermore, I want to thank all cooperation partners:

- Imre Szenti and Prof. János Kiss (MTA-SZTE Reaction Kinetics and Surface Chemistry Research Group, University of Szeged)
- Dr. Francesc Salvat-Pujol and Prof. Roser Valentí (Institut für Theoretische Physik, Goethe-Universität Frankfurt)
- Dr. Hartmut Gliemann and Prof. Christoph Wöll (Institut für funktionelle Grenzflächen, Karlsruhe Institute of Technology)

For the outstanding technical support, I want to thank Hans-Peter Bäumler and Bernd Kreß. Friedhold Wölfel and all members of the mechanical workshop are equally acknowledged for the reliable help regarding all kinds of small and big requests.

Finally, I want to thank my friends and family for all the support!